Fall 10-1-2021

The Rheology of Striated Muscles

Khoi Dac Nguyen
Yale University Graduate School of Arts and Sciences, khoi.nguyen@yale.edu

Abstract

The Rheology of Striated Muscles

Khoi Dac Nguyen

2021

Striated muscles are actuators of animal bodies. They are responsible for several biomechanical functions critical to survival and these include powering the cardiovascular system and modulating the mechanical interactions the body has with its surroundings. Nearly two centuries of active research on muscle phenomena has led to detailed insights into its microscopic composition, but accurate predictive models of muscle at larger scales remain elusive. This thesis reports on efforts to accurately capture the mechanical properties of striated muscles based on current knowledge of actomyosin dynamics. Specifically, this thesis derives the rheology of striated muscles from the dynamics. Muscle rheology is a characterization of the forces that it develops in resistance to externally imposed changes to its length, i.e. its mechanical behavior as a material. For example, the rheology of elastic solids is stiffness and that of viscous fluids is a damping coefficient. Detailed analyses of actomyosin dynamics suggest that the smallest functional units of striated muscles, half-sarcomeres, are viscoelastic and can function as either a solid-like struct or a fluid-like damper depending on time-durations of interest and neural inputs. Such adaptability may underlie the vastly different biomechanical functions that striated muscles provide to animal bodies. Furthermore, muscles are active structures because their properties require metabolic energy and depend on neural inputs. Striated muscles can therefore exhibit rheologies and functions that elastic springs and viscous fluids cannot. The analysis presented in this thesis may extend beyond muscles and biomedical applications. It may help to engineer muscle-like actuators based on principles of tunable properties and to understand the physics of other materials that can similarly transition between being solid-like and fluid-like.

The Rheology of Striated Muscles

A Dissertation

Presented to the Faculty of the Graduate School

Of

Yale University

in Candidacy for the Degree of

Doctor of Philosophy

by

Khoi Dac Nguyen

Dissertation Director: Madhusudhan Venkadesan

December, 2021

Contents

List of Figures

List of Tables

Acknowledgements

First and foremost, I want to thank my family. My parents immigrated from Vietnam to the USA with five kids, myself the youngest, and not much else. I can only imagine how difficult it was. My older siblings took on much of the responsibilities of an immigrant family and I had a relatively carefree childhood as a result of their efforts. For that and much more, I have always been grateful.

I was lucky to have been mentored by a number of individuals who saw to my personal development as a researcher. I apologize to them for the growing pains and am grateful for their mentorship. Tsute Chen, Caroline Owen, Martin Knolle, Robert Huie, Shreyas Mandre, Mahesh Bandi, and Madhusudhan Venkadesan are influential figures to me. I hope that my academic progress brings delight to them and encourages them to continue mentoring others.

I also want to acknowledge members of the Yale community with whom I was fortunate enough to cross paths. I shall always share a special bond with my fellow lab members, Neelima Sharma, Ali Yawar, Nihav Dhawale, and Carolyn Eng. I spent a fair bit of time interacting with the labs of Michael Murrell and Rebecca Kramer, and I am grateful for all the intellectual conversations I had with them. Aya Nawano and Zhe Mei are fellow Ph.D. students that I've gotten to know well. And lastly, I am grateful to Beth Benneth for showing me what it meant to be an amazing instructor.

Although they have been previously named, I want to specifically thank my committee members, Shreyas Mandre, Michael Murrell, and Madhusudhan Venkadesan, for their inputs and guidance over the years.

Chapter 1

Introduction

1.1 Overview

Muscles are biological actuators whose actions underlie many functions integral to animal bodies and can take on specialized forms depending on function [1–3]. Cardiac muscles form much of a heart's mass, which allows the heart to pump and circulate blood throughout the body. Skeletal muscles connect to and pull on bones to control body posture and movements. Smooth muscles line internal organs, airways, and vasculature to aid in the transport of air and blood. Applications of muscles in animal bodies are many, and the dysfunction of any single or a group of muscles relates to a wide spectrum of neuromuscular and cardiac diseases in humans[4–6]. Better understanding the internal components of muscles and how they give rise to different functions will impact the development of biomedical treatments and interventions against muscle-related diseases. There are many aspects to muscles, including but not limited to their development, specialization, neural control, and mechanics [1, 6, 7]. This thesis reports on the mechanics of cardiac and skeletal muscle cells, collectively referred to as striated muscle cells due to a distinctive striation pattern when viewed under a microscope.

The simplest idealization of striated muscles as a mechanical structure is a force-

generating motor that pulls on its environment with a constant force dictated by the nervous system. But this idealization forgoes all mechanical interactions between a muscle and its environment, which may act to stretch or contract it. These mechanical interactions are metaphorically the first line of defense to environmental inputs because they can respond faster than the nervous system that is limited by transmission delays [8–10]. They constitute the biomechanical properties often associated with muscles, namely the elastic stiffness needed to maintain body postures and viscous damping needed to dissipate kinetic energy [8, 11–13]. The study of a muscle's mechanical interactions with its environment is its material rheology and puts forth a more general and, as will be shown, more powerful idealization of striated muscles as both a material and a force-generating motor.

This thesis reports on efforts aimed at understanding and characterizing the material components of striated muscles that may help to generate better predictive muscle models to be used in biomedical applications. Unlike many materials, striated muscles are also active tissues with properties that vary considerably with neural inputs. As a result, they can exhibit rheologies not found in passive materials and can provide biomechanical functions that other tissues cannot. The thesis provides mathematical analyses that connect two classes of muscles models operating on vastly different size scales, macroscopic models based on phenomenological data [7] and microscopic models based on the mechanochemical dynamics of molecular motors that ultimately drive muscle forces [14, 15].

1.2 Motivations

1.2.1 Muscle function

The neural control of a muscle's rheology bridges together the multiple biomechanical functions that it provides [16]. At one extreme, a muscle may function as a solid-

like strut to stiffen a joint and to allow for efficient energy storage in the connecting tendons [8, 11]. At another extreme, it may function as a viscous fluid to safely dissipate excessive kinetic energy or to yield and minimally resist a motion antagonist to its line of action [12, 13, 17]. In general, when held at a constant neural input, muscles exhibit every viscoelastic intermediate between the extremes depending on the input [18–22]. But, under dynamic modulation of neural inputs, muscles can do more than passively resist perturbations and actively perform mechanical work on their surroundings to function, for example, as controlled brakes and motors [23–25]. Understanding the types of functions that may arise from the control of a muscle's rheology would have broad applications in multiple communities. In biomedical sciences, it can help design rehabilitation strategies against the loss of motor control in patients and thereby provide quality-of-life improvements in clinical settings [4]. And in animal biomechanics, it can provide models for neuromechanical interactions that are currently lacking in current models and motivate new theory-driven experiments that probe deeper into a muscle's contractile machinery [1, 26].

1.2.2 Design of actuators from tunable materials

Soft materials are often the mechanical interfaces between an actuator and its environment but the materials themselves, like muscles, can also actuate if their properties are dynamically tuned by an external stimulus [27–29]. This type of actuation is possible because changes in properties such as stiffness, damping, or a generalized impedance are often coupled with energy consumption that can translate to net mechanical work. Actuation by soft materials is the central idea of soft robots that locomote around without using heavy and structurally rigid mechanical components [28–30]. In principle, many soft materials can actuate, including shape memory alloys, dielectric elastomers, and magnetorheological fluids by timely control of their rheology [27, 31, 32], and some have already been implemented in soft robots [29].

The stimulus controlling the rheology depends on the soft material and may be pressure, current, magnetic fluid, or some other physical input. A framework that maps material rheology to a desired actuation efficiently implement control schemes for soft robots, however, remains to be developed. Current efforts consist of solving computationally difficult models or restricting the soft robot to quasi-static motion in a structured environment [30, 33], which preclude the ability to dynamically adapt and navigate uncertain environments. Muscle is a prime biological example of actuation by soft materials and studying its intricacies is likely to motivate and provide valuable insights towards developing a more general framework.

1.2.3 Physics of fluid-solid transitions

Materials that can transition between solid-like and fluid-like behaviors have tunable rheologies and are an active area of research in the field of soft matter [34]. Specifically, a universal jamming transition is hypothesized to underlie how these materials solidify and fluidize [35]. Muscles are active and biological structures that can solidify and fluidize [16], and so are passive and inanimate structures such as sand piles and cornstarch slurries often used in classroom demonstrations [36]. The constituents of these examples surely differ but the hypothesized jamming transition suggests that their governing dynamics are similar and driven by the same set of physical principles. Muscles provide a unique set of lenses with which to view these physical principles. The degree with which we can experimentally manipulate and image in real-time each constitutive unit of a muscle is likely unmatched by any biological material [37, 38]. Fluid-solid transitions are physical processes observed in a whole class of materials and not just of muscles [16, 34]. A muscle's tunable rheology ought to be understood in the context of all these materials and of the physical insights that each provides.

1.3 Outline and Scope

The thesis is structured as a series of stand-alone chapters that each introduce the requisite tools and concepts.

Chapter 2 - Rheology of actomyosin crossbridge ensembles

One class of muscle models idealizes striated muscle forces as resulting from the collective behavior of an ensemble of stochastically cycling crossbridges. This chapter examines multiple ensemble crossbridge models of varying complexity to derive the rheology that emerges from their dynamics. The chapter shall show that the ensemble rheology comprises of exponential modes of stress relaxation.

Chapter 3 - Rheological basis of skeletal muscle work loops

This chapter presents a general framework that adapts current oscillatory rheological characterizations to account for a time-varying external stimulus. It postulates that the rheology under a time-varying stimulus can be decomposed into basis rheologies measured under a constant stimulus. Accuracy and feasibility are tested for using comparisons between predictions of this framework and work loop data of fish (sculpin) abdominal muscles.

Chapter 4 - The role of filament compliance in sarcomeric viscoelasticity

A property of ensemble crossbridge models analyzed in Chapter 2 is that the timescales of the exponential modes are independent of ensemble size, which prevents any fluid-to-solid transitions in such models. Chapter 4 shows that introducing thick and thin filament compliances allows for crossbridge-crossbridge interactions that lead to ensemble size-dependent timescales. It examines the feasibility of such a mechanism using estimates of sarcomere parameters.

Chapter 5 - Conclusions and future directions

The final chapter summarizes the findings of this thesis. It also discusses the author's opinion on potential research directions that the thesis would be of value towards.

Chapter 2

Rheology of crossbridge ensembles

2.1 Abstract

How muscle's bulk material properties emerge from the ensemble dynamics of molecular motors is a longstanding question. Muscle's rheology, how it responds when externally perturbed, is crucial for animal motor control. Classical descriptions of the bulk rheology in terms of force-length or force-velocity relationships capture only part of muscle's perturbation response and we currently lack an understanding of the emergent properties arising from the microscopic actomyosin crossbridge dynamics. In particular, although much is known about the microscopic machinery, current mathematical models that describe the behavior of a population or an ensemble of crossbridges are plagued by an excess of parameters and computational complexity that limits their usage in large-scale musculoskeletal simulations. In this chapter, we examine models of crossbridge dynamics of varying complexities and show that the emergent rheological response of an ensemble of crossbridges can be simplified to few dominant time-constants associated with intrinsic dynamical processes. For the two-state crossbridge model, we derive exact analytical expressions for the bulk rheology and find that the ensemble behavior is characterized by a single time-constant. For up to five-state crossbridge models, we need at most three time-constants to capture

the ensemble behavior. Our results yield simplified models comprising of discrete exponential relaxations for muscle's bulk rheological response that can be readily used in large-scale simulations without sacrificing the model's interpretation in terms of the underlying crossbridge dynamics.

2.2 Introduction

Muscle exerts force when it is neurally stimulated and also when its length is externally perturbed [7, 26]. The dynamics of the perturbation response is crucial for motor control because it enables faster-than-reflex response to unexpected perturbations [1, 8, 9, 16, figure 2.1a]. Like most soft materials, muscle's perturbation-induced stress decays over time [15, 16], and the timescales involved in the decay affect the functional role of muscle. On shorter periods than the decay time, muscle behaves like an elastic solid body that resists stretching and could help elastic energy storage in series elements like tendons [8, 11]. Over longer periods than the decay time, muscle dissipates stress somewhat like a viscous liquid, and enables rapid postural changes and kinetic energy dissipation [12, 13]. Unlike passive materials, muscle's stress decay is affected by the neurally regulated active molecular interactions of myosin motors with actin filaments [39]. Thus, understanding muscle's emergent rheological response due to the underlying molecular machinery helps us understand how muscle contraction affect animal motor function [8, 16, figure 2.1a].

Muscle properties such as short-range stiffness, viscous damping, loss modulus, and storage modulus are examples of bulk rheological properties [13, 40, 41], and analogous to similar characterization of passive materials [42] and active materials [43, 44]. In muscle, the bulk rheology arises from contributions of its passive tissues, geometry, and internal molecular machinery [6, 45]. The mapping from the microscopic dynamics of the molecular machinery to its contributions to bulk properties

remains incomplete, however, and this gap is exemplified by the split between two classes of widely used muscle models. Namely, macroscopic phenomenological models and microscopic mechanochemical models that idealize muscles as one-dimensional structures.

Phenomenological models inspired by A.V. Hill's work are widely used to quantitatively describe muscle's force production capabilities [7, 46–48]. These models incorporate an active contractile element, a parallel material element that is often modeled as a passive elastic or viscoelastic material, and series elasticity that captures tendon and other passive tissue compliance [figure 2.1b]. The passive parallel element represents non-contractile tissues and the intramuscular fluid that have well-known effects on the contractile force capacity of muscle [45]. But muscle's perturbation response is dominated by the active contractile element except under extreme eccentric conditions where the passive parallel element is important [46, 49]. In Hill-type models, the perturbation response of the active element are represented by isometric force-length and isotonic force-velocity properties and its interactions with the series elasticity [7, 48]. Although force-length and force-velocity properties accurately capture the perturbation response under specific motor contexts [7], they fail under *in vivo* situations like locomotion where non-isometric and non-isotonic conditions are commonplace [50–54], leading to transient and non-steady perturbation responses [figure 2.1b]. Furthermore, parameters in phenomenological models do not lend themselves to interpretation in terms of known mechanochemical processes within muscle. Despite these shortcomings, phenomenological models remain the most viable means to perform large-scale biomechanical simulations and optimal control calculations because of their low computational burden and ease of implementation [55–57].

The flip side to phenomenological models are those that incorporate the current state of understanding of the microscopic mechanochemical cycles that drive muscle.

The hydrolysis of ATP by myosin motors during formation of actin-myosin crossbridges underlie active muscle contraction and influence its rheological perturbation response [14, 15, 58]. Each myosin undergoes the biochemical Lymn-Taylor cycle in which it attaches to and detaches from actin filaments based on ATP capture, hydrolysis, and release of byproducts [14]. There are different modeling approximations of this cycle that incorporate different numbers of intermediate states [figure 2.1b]. The biochemical Lymn-Taylor cycle is coupled to a mechanical cycle that converts chemical energy to mechanical work. When attached, each myosin motor pulls on the actin filament to generate piconewton forces and around 10 nm power strokes. The collective action of many motors is modeled as an ensemble of stochastically cycling crossbridges whose force contributions add up [15, 59]. Mechanical perturbation of the whole muscle ultimately perturbs the mechanochemical crossbridge cycle whose dynamics are load and strain-dependent [60, 61], which in turn alters the force produced by the ensemble and, in principle, manifests as bulk rheological properties of muscle. But crossbridge models employ numerous biochemical parameters that cannot be directly measured because of which we lack a mechanistic understanding of muscle's emergent rheology. This is the so called scale-connection problem.

Addressing the scale-connection problem would overcome many of the shortcomings of both microscopic and macroscopic models, and is a major objective of neuromuscular research [26]. The distribution-moment formalism was a crucial step in on-going efforts to address it and presented a general approach to simplifying microscopic models without relying on the exact choice of how a crossbridge cycle is modeled [62–64]. Specifically, the formalism assumed a Gaussian distribution for the fraction of bound crossbridges at every strain such that the governing ensemble dynamics is approximated by the dynamics of measurable macroscopic quantities: stiffness, forces, and elastic energy storage. Thus, it is an approximate yet tractable mapping from these macroscopic quantities to the ensemble dynamics. But in assum-

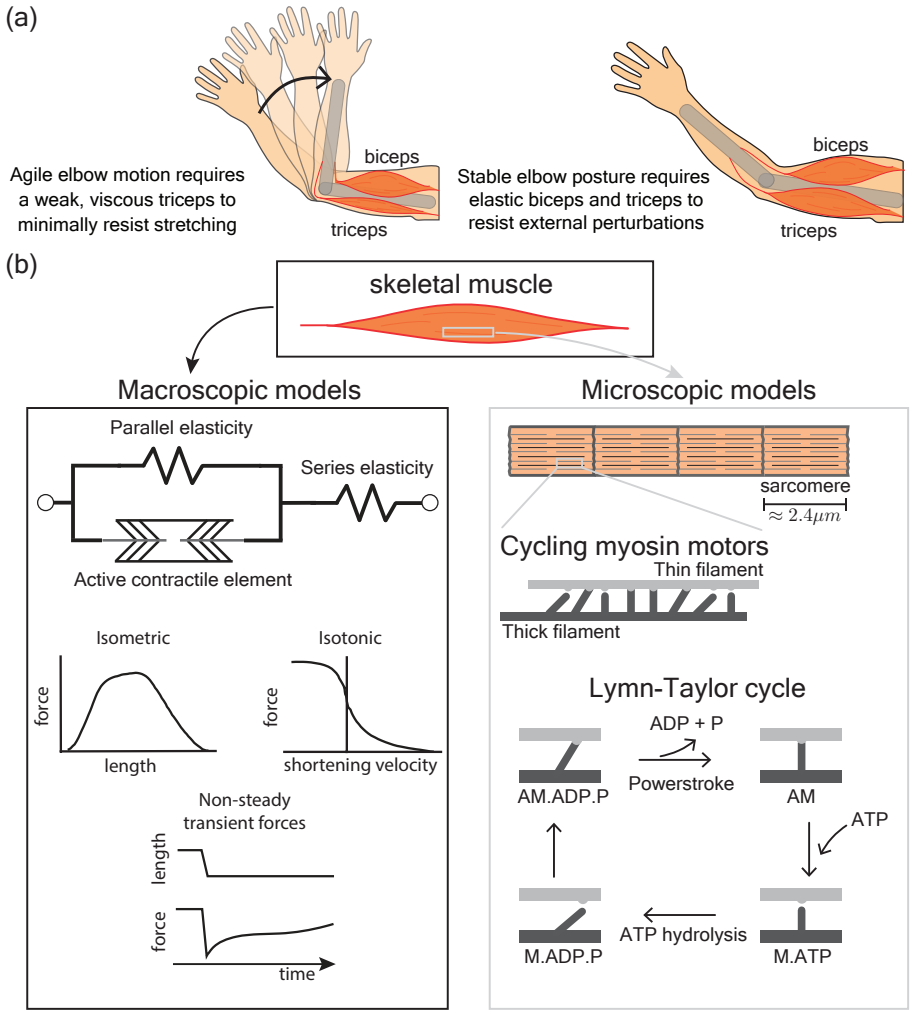

Figure 2.1: Current models of skeletal muscles. (a) An example of the motor functionalities provided by a muscle's rheological response to perturbations. (b) Widely used muscle models can be separated into microscopic biochemical models and macroscopic phenomenological models. The microscopic models track the dynamics of myosin motors whereas macroscopic models apply isometric and isometric characterizations and transient forces to capture the active contractile element. The isometric and isotonic characterizations are adapted from [figure 8 of 7] and the transient forces are adapted from [figure 3 of 15]. The current paper seeks to connect the crossbridge cycle dynamics to the emergent generalized transient force response beyond the isometric and isotonic characterizations of muscle.

ing a preset distribution and not one that emerges from the crossbridge dynamics, it stops short of connecting scales back to the crossbridge cycle. Shortcomings of this approximation are evident from multiple perturbation experiments which show that the distribution-moment model does not accurately capture muscle forces, but more

complex crossbridge models may be able to do so by sacrificing computational speed [65, 66]. So a gap remains in mapping crossbridge theory to the emergent rheology of its ensemble.

In this chapter, we connect the dynamics of a single crossbridge to the rheology of an ensemble that represents a whole sarcomere. In particular, we analyze the ensemble behavior of several different crossbridge models to identify a minimal parameter-set that affects their emergent rheology. The paper begins with a brief tutorial on rheological characterization of materials using complex modulus and dynamic stiffness. Then we use numerical simulations of large ensembles of crossbridges, ranging in complexity from two-state to five-state crossbridge models, to identify commonalities and differences in their rheological response. Next we analytically derive the rheology of a two-state crossbridge model and show how a single exponential relaxation process with one time-constant suffices to capture its rheology, how that relaxation is related to the crossbridge dynamics, and provide a mechanical interpretation in terms of elastic and viscous material properties. We then extend the characterization to more complex crossbridge models in terms of multiple exponential processes and discuss the implications of our work to the development of computationally efficient and parametrically parsimonious models that are still interpretable in terms of the microscopic mechanochemical dynamics of actomyosin crossbridges.

2.3 Mathematical Preliminaries

We focus here on the linear rheological characterization of muscle, which has proven useful in developing predictive models of muscle behavior [8, 16, 40] and in interpreting *in vivo* muscle function for both large and small perturbations [5, 67]. A central quantity in linear rheology is the material modulus defined as the ratio of the measured stress to the applied strain. The modulus for muscle depends on the rate at which the

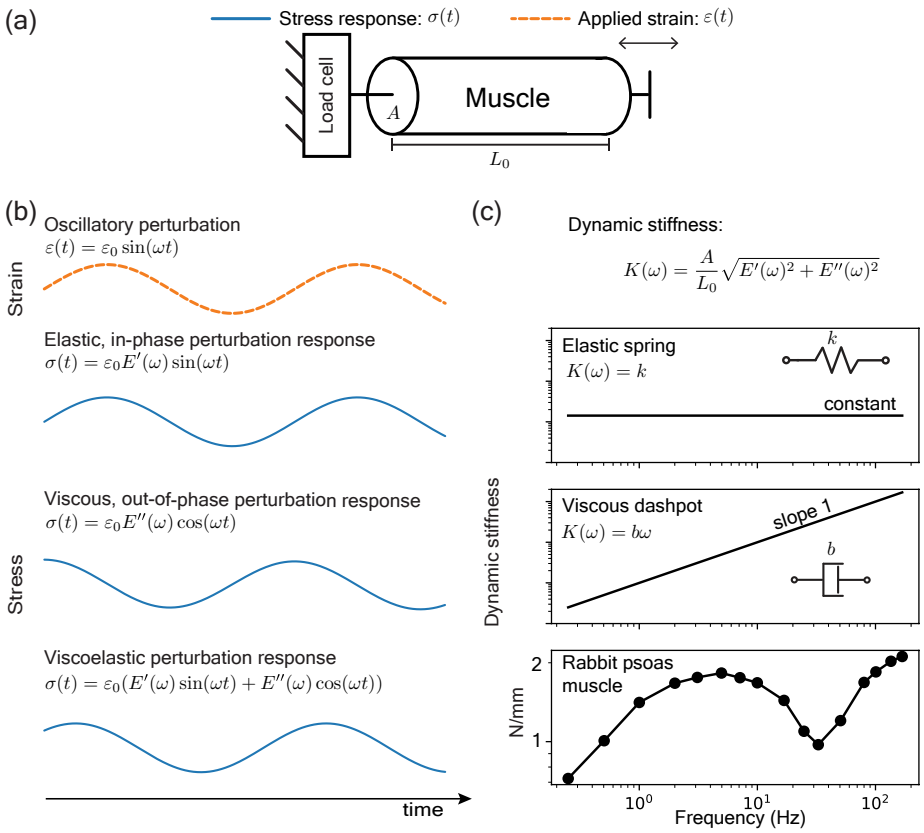

Figure 2.2: Linear rheological characterization of muscles. (a) Schematic of an experimental setup to measure a muscle's response to perturbations. (b) For an oscillatory length perturbation, the linear rheological response is characterized by an elastic modulus $E'(\omega)$ that measures the in-phase response and a loss modulus $E''(\omega)$ that measures the out-of-phase response. A general viscoelastic response has both in-phase and out-of-phase components. (c) The dynamic stiffness $K(\omega)$ is a third oscillatory rheological characterization. It is constant if the muscle is elastic and linearly proportional to frequency if the muscle is viscous. The dynamic stiffness of a rabbit psoas muscle is viscoelastic with features more complicated than elastic springs and viscous dashpots alone. The rabbit psoas plot is adapted from [figure 3 of 41].

strain is applied and varies over time. Using the Laplace or Fourier transform [68], the applied strain and the resulting stress response can each be decomposed into a sum of sinusoids of different temporal frequencies, and their ratio yields a frequency-dependent modulus. This characterization, a core tool in oscillatory rheology [42, 69], provides an interpretation of muscle material properties in terms of frequency-dependent loss, storage, and complex moduli [16, 41, 70]. If the applied strain is a small-amplitude sinusoidal wave, then the resulting stress is approximately sinusoidal

with both in-phase and out-of-phase components with respect to the applied strain [figure 2.2(a-b)]. The amplitude of the in-phase stress and out-of-phase stress divided by the applied strain amplitude define the storage modulus $E'(\omega)$ and loss modulus $E''(\omega)$, respectively. These moduli are a function of the oscillatory frequency ω. The complex modulus $E^*(\omega) = E'(\omega) + iE''(\omega)$ is a compact representation of the spring-like storage modulus and damper-like loss modulus. The dynamic stiffness $K(\omega)$ of sinusoidal analysis is related to the complex modulus as $K(\omega) = (A/L_0)|E^*(\omega)|$ for a muscle tissue of cross-sectional area A and length L_0. If muscle were elastic like a Hookean spring, then $K(\omega)$ is a constant independent of frequency. If muscle were viscous like a Newtonian fluid, then $K(\omega)$ is linearly proportional to frequency. In reality, muscle is neither extreme and exhibits intermediate viscoelastic behavior [figure 2.2c].

2.4 Results

2.4.1 Rheology of crossbridge ensembles

We shall use numerical simulations of different types of crossbridge models to compare and analyze their emergent rheological behaviors. Included in the models considered is Huxley's two-state formulation that helped set the foundations for the class of proposed crossbridge models developed since and its emergent rheology can thus serve as a point of reference [59]. In it, Huxley idealized crossbridges as independently cycling elastic springs that stochastically attach to and detach from a rigid thick and thin filament backbone. The total elastic resistance of a population or ensemble of these crossbridges is then taken to characterize the active and transient forces of muscles. When the ensemble is externally perturbed, as in a rheological experiment, the attached crossbridges elastically resist the perturbation and prevent the thick and thin filaments from sliding past each other. But because crossbridges eventually

detach, the elastic resistance will decay in time and lead to a viscous dissipation of mechanical energy. More recent crossbridge models refine Huxley's formulation by incorporating additional attached and detached states, and this introduces new dynamics to the emergent rheological behavior that we shall examine.

The crossbridge models considered include a three-state, four-state, and five-state model in addition to Huxley's two-state model [59, 71–73]. The models were selected firstly to sample the range of intermediate states found amongst proposed crossbridge models and secondly to sample the different types of muscle phenomena considered in the literature. The three-state model of Murase et al., 1986 showed that a second attached crossbridge state is necessary to capture the three dominant sinusoidal processes observed in insect flight muscles [71]. The four-state model of Smith, 1998 proposed a minimal kinetic scheme to capture the force transients resulting from the phosphate release and ATP capture of the Lymn-Taylor cycle [14, 72]. And lastly, the five-state model of Lombardi and Piazzesi, 1990 proposed a relatively complex kinetic scheme to capture the tension transients of a frog skeletal muscle fiber under steady lengthening that, notedly, incorporated a forced detached state accessible only when crossbridges are stretched beyond a critical distance. The number of parameters involved for each model are many with 4 for Huxley's two-state model, 16 for the three-state model, 17 for the four-state model, and 24 for the five-state model. These parameters define the neutral length and stiffness of each attached crossbridge state and the strain-dependent transition rates between internal states. A natural question that arises is how the emergent ensemble rheology depends on these parameters and, given such a vast parameter space, whether a parameter-reduction is possible that yields the same ensemble rheology. We shall address these questions with numerical simulations and detailed analysis of crossbridge dynamics.

We find that a simple rheology emerges at high and low frequencies regardless of the number of intermediate states in ensemble crossbridges models and that the

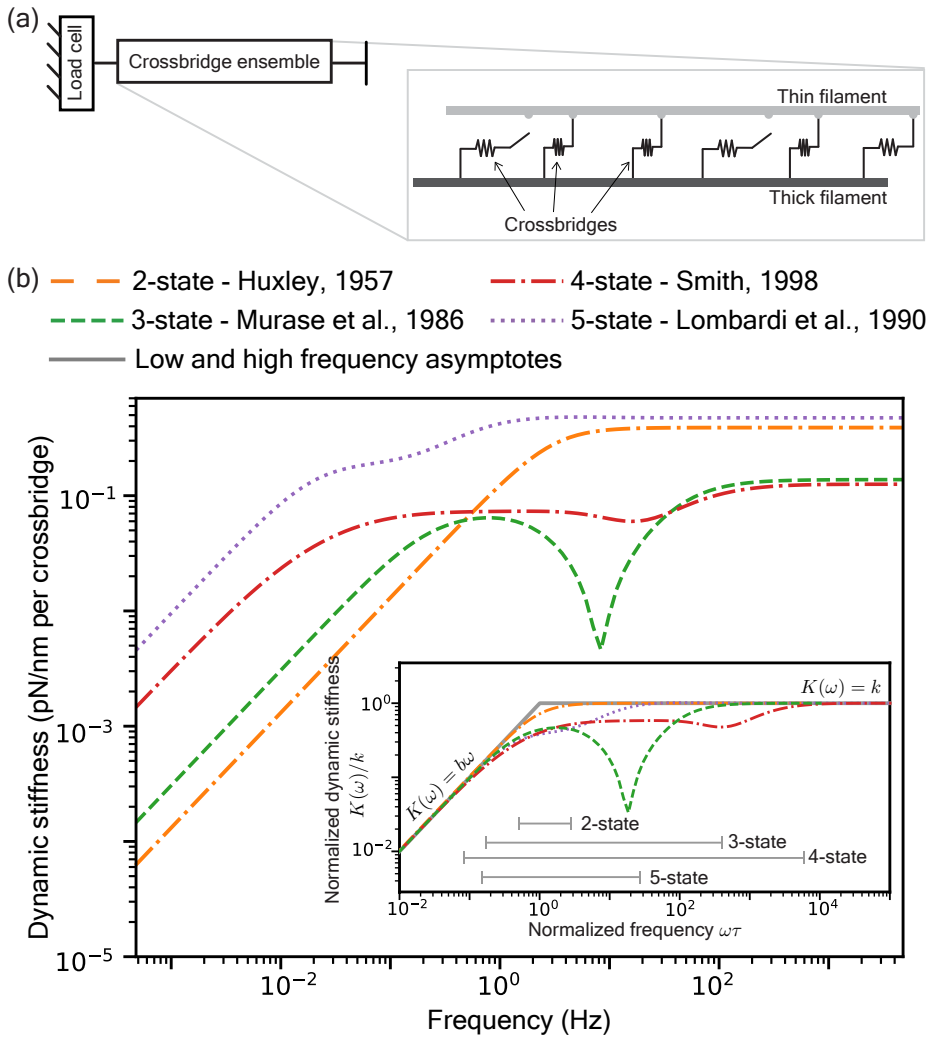

Figure 2.3: Rheology of the ensemble dynamics of different crossbridge models. (a) An ensemble of crossbridges operate collectively to model muscle forces. (b) The frequency-dependent dynamic stiffness of different crossbridge models resembles an elastic spring at high frequencies and a viscous dashpot at low frequencies. (inset) Collapse of different models onto equation 2.1 by normalizing the axes. For each model, the dynamic stiffness is normalized by the value k computed at the highest frequency. The frequency axis is normalized by a time-constant τ at which the two asymptotic behaviors match. The gray bars indicate the bandwidth over which the models deviate by more than 5% from their asymptotic behavior s.

difference between crossbridge models manifest only on intermediate frequencies [figure 2.3b]. For each model, we compute the collective force response of a crossbridge ensemble to a step length perturbation and extract the frequency-dependent dynamic stiffness [Methods 2.7.1]. The dynamic stiffness is constant at high frequencies and

linearly proportional to ω at low frequencies, i.e. the dynamic stiffness is approximately

$$K(\omega) \approx \begin{cases} k & \text{for high frequencies,} \\ b \cdot \omega & \text{for low frequencies.} \end{cases} \tag{2.1}$$

These asymptotic regimes present a mechanical interpretation as a high-frequency spring constant k and and low-frequency damping constant b. But the dynamic stiffness at intermediate frequencies is more complicated in their frequency dependence and differs between the model variants. We calculate a bandwidth in this intermediate frequency band where the dynamic stiffness differs by more than 5% from the asymptotic response [grey bars in inset of figure 2.3b]. The two-state Huxley model [59] has the smallest bandwidth, whereas the 4-state model [72] has the largest bandwidth of over five orders of magnitude [figure 2.3b, inset]. Greater the bandwidth, the more numerically 'stiff' the model is, and thus greater the computational burden for simulation. This is because the largest time-step that can used in numerical integration of the model's differential equations is governed by the high-frequency end of the bandwidth, whereas the duration of time needed for the transient responses to settle down is governed by the low-frequency end of the bandwidth.

2.4.2 Rheology of the generalized two-state crossbridge model

We analytically derive the rheology for the two-state crossbridge ensemble to examine the rheological features at intermediate frequencies that are not captured by the high and low frequency asymptotes (Eqn. 2.1). We refer to [72] for a conceptually identical but more general derivation of a four-state crossbridge model while we focus here on the simpler two-state variant to demonstrate how modeling choices lead to different rheological features.

Two-state crossbridges in the ensemble cycle between making and breaking bonds between rigid thick and thin filaments. The attachment rate $f(x)$ and detachment

rate $g(x)$, to form and break bonds, respectively, are functions of the distance x between the location of the myosin motor on the thick filament and the nearest binding site on the thin filament. At every distance x and time t, the proportion of attached crossbridges is $n(x,t)$, also known as the bond distribution, and the detached proportion is $(1-n(x,t))$. The bond distribution $n(x,t)$ evolves in time according to

$$\frac{dn(x,t)}{dt} = (1-n(x,t))f(x) - n(x,t)g(x). \tag{2.2}$$

This first-order differential equation has a steady-state bond distribution $n_{\text{ss}}(x) = f(x)/(f(x)+g(x))$ at equilibrium. Starting with this equilibrium bond distribution, a step length perturbation of amplitude a is delivered at $t=0$ to elongate the whole system and held there. Every crossbridge that was a distance x away from its nearest binding site is now a distance $(x+a)$ away and the distribution of crossbridges $n(x,t)$ evolves in time to relax back to its equilibrium state according on equation 2.2. The response to this step length perturbation is obtained using $n(x,0) = n_{\text{ss}}(x-a)$ as the initial condition and integrating equation 2.2 to find

$$n(x,t) = n_{\text{ss}}(x) + (n_{\text{ss}}(x-a) - n_{\text{ss}}(x))e^{-t(f(x)+g(x))}. \tag{2.3}$$

Therefore, $n(x,t)$ exponentially relaxes to its steady-state $n_{\text{ss}}(x)$ at a rate $f(x)+g(x)$. We illustrate this relaxation process in figure 2.4a using Huxley's rate functions [59]. The force $\Delta F(t)$ in response the step length perturbation is determined by the difference between $n(x,t)$ and its steady state $n_{\text{ss}}(x)$. In terms of the stiffness λ_{xb} per attached crossbridge in units of [force/length] and crossbridge density M in units of $[\text{length}]^{-1}$, the force response is,

$$\Delta F(t) = M\lambda_{\text{xb}} \int_{-\infty}^{\infty} x(n_{\text{ss}}(x-a) - n_{\text{ss}}(x))e^{-t(f(x)+g(x))}dx. \tag{2.4}$$

By restricting our attention to the linear regime, *i.e.* a small perturbation a, the force response simplifies to

$$\Delta F(t) = -Ma\lambda_{\text{xb}} \int_{-\infty}^{\infty} x \frac{dn_{\text{ss}}}{dx} e^{-t(f(x)+g(x))} dx. \tag{2.5}$$

This perturbation response may be rewritten as a sum of exponential relaxations with a strain-dependent relaxation time-constant $\tau(x)$ and strain-dependent ensemble stiffness $k(x)$ that is given by,

$$\Delta F(t) = a \int_{-\infty}^{\infty} k(x) e^{-t/\tau(x)} dx, \tag{2.6}$$

$$k(x) = -M\lambda_{\text{xb}} x \frac{dn_{\text{ss}}(x)}{dx}, \text{ and} \tag{2.7}$$

$$\tau(x) = \frac{1}{f(x) + g(x)} \tag{2.8}$$

Therefore, the entire relaxation process may be thought of as being comprised of an infinity of sub-processes where the strain-dependent stiffness $k(x)$ is the weight for each relaxation sub-processes. To obtain a dynamic stiffness $K(\omega)$, we use the Laplace transforms of equation 2.6 and of the step length perturbation to arrive at

$$K(\omega) = \left| \int_{-\infty}^{\infty} k(x) \frac{i\omega}{i\omega + 1/\tau(x)} dx \right|. \tag{2.9}$$

The integrand is the mechanical impedance of a Maxwell body, a spring mechanically in series with a dashpot. A mechanical analogy can thus be drawn between ensemble crossbridge dynamics and Maxwell bodies. The Maxwell spring has a stiffness $k(x)$, the Maxwell dashpot has a damping coefficient $b(x) = k(x)\tau(x)$, and the Maxwell body exponentially relaxes force just as an ensemble of crossbridges do.

The mechanical analogy with a Maxwell body is demonstrated for the two-state model using Huxley's choices for the rate functions $f(x)$ and $g(x)$ [59, figure 2.4b].

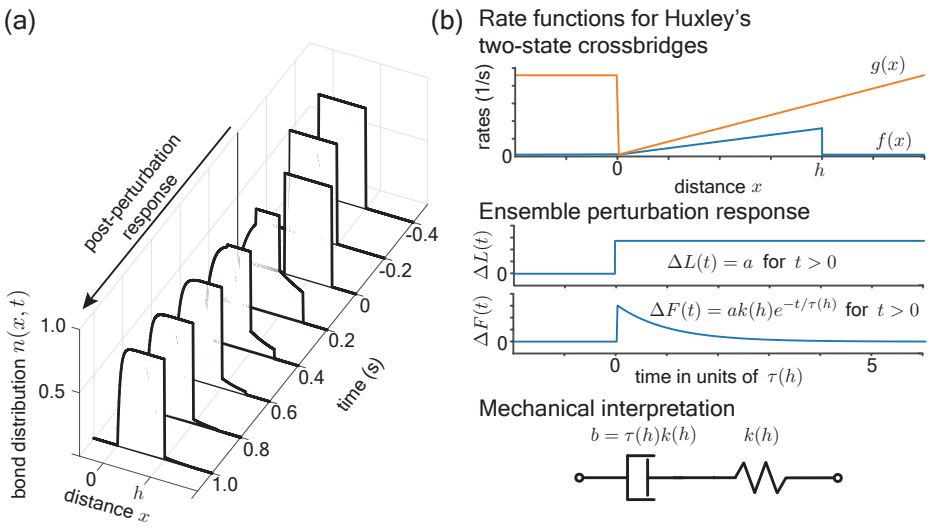

Figure 2.4: The rheology of an ensemble of Huxley's two-state crossbridges. (a) The time-evolution of the bond distribution in response to a step length perturbation. (b) Rheology of an ensemble of Huxley's two-state crossbridges. The ensemble's perturbation response exponentially relax with time-constant $\tau(h) = 1/(f(h) + g(h))$ where $f(x)$ and $g(x)$ are the rate functions and h is the powerstroke distance. A mechanical interpretation of this single exponential relaxation is of a spring in series with a dashpot.

The rate functions $f(x)$ and $g(x)$ are

$$f(x) = \begin{cases} f_1 x \text{ for } 0 \leq x \leq h, \\ 0 \text{ otherwise,} \end{cases} \quad \text{and} \tag{2.10}$$

$$g(x) = \begin{cases} g_2 \text{ for } x < 0, \\ g_1 x \text{ for } x \geq 0. \end{cases} \tag{2.11}$$

Using these rate functions, the steady-state bond distribution $n_{\text{ss}}(x)$ is

$$n_{\text{ss}} = \begin{cases} f_1/(f_1 + g_1) \text{ for } 0 < x \leq h \\ 0 \text{ otherwise.} \end{cases} \tag{2.12}$$

Using equations (2.7 - 2.9), the dynamic stiffness is that of a single Maxwell

body with stiffness $k(h)$ and damping coefficient $b = k(h)/(f(h) + g(h)) = k(h)\tau(h)$. Huxley's choices thus lead to an exact correspondence between ensemble crossbridge dynamics and a single Maxwell body. The rectangular waveform of the steady-state bond distribution implies that $k(x)$ is a sum of two δ-functions, a negative one at $x = 0$ and a positive one at $x = h$. However, the delta at $x = 0$ contributes zero stresses, which implies that only the sub-process at $x = h$ contributes to the stress-relaxation response and leads to a single Maxwell body. The elastic component of the frequency-dependent behavior arises because each bound crossbridge is already modeled as a spring, all of which simply add at high frequencies. On the other hand, there are no dampers built in to a single crossbridge model. The damper component only appears when considering the entire ensemble rather than a single crossbridge. Crossbridges dissipate stored elastic energy as they cycle and this dissipation averaged over many crossbridges and many cycles manifests as an effective damping coefficient that depends on the energy that each spring would store and the time it would take to dissipate that energy. Therefore, the ensemble behavior at low frequencies is that of a linear damper.

As shown, $k(x)$ of equation 2.7 is well-approximated by a δ-function for Huxley's two-state model leading to single sub-process that dominates the entire response. Thus whether we need the full ensemble model or if we can approximate the response with just a few discrete relaxation sub-processes depends on whether $k(x)$ shows localizations in x or not. We hypothesize that, for all crossbridge models considered in this chapter, the localization is a dominant feature and that only a few discrete relaxation sub-processes are needed to capture the emergent rheological features on intermediate frequencies [figure 2.3b]. Because $k(x)$ is proportional to the derivative of the steady-state bond distribution, its localization and the resulting exponential sub-process directly equate to either a sharp rising or falling edge of the steady-state bond distribution, or of multiple bond distributions for crossbridge models with

multiple attached states. We shall verify the hypothesis by fitting exponential sub-processes to the dynamic stiffness computed for the crossbridge models and examine if those fitted processes corresponds to rising or falling edges.

2.4.3 Low-order models of multi-state crossbridge ensembles

Crossbridge dynamics are generally more complex than Huxley's two-state model and may have multiple internal states that introduce higher-order dynamics. Nevertheless, the perturbation force response arises from stretching bound crossbridges and stress relaxation is because of a redistribution of the crossbridges between the various possible states. When a crossbridge detaches, it dissipates the energy stored in it due to the length perturbation as heat, which is dissipated over the timescale for the completion of full crossbridge cycle. This suggests an approach to tackle the behavior in the intermediate frequencies when the more detailed crossbridge models deviate from the simple asymptotic behavior of a Maxwell body. The exact analysis of the generalized two-state model suggests that under more complicated attachment-detachment dynamics, the response would show multiple exponential relaxation sub-processes with timescales τ corresponding to the most dominant ensemble stiffness k. So we investigated whether a finite number of exponential relaxations can capture their rheologies in spite of possible complexities, under the hypothesis that a few sub-processes would dominate the response. We find that just three exponentially relaxing sub-processes accurately capture the frequency-dependent stiffness over seven orders of magnitude on the frequency axis [figure 2.5a, Methods 2.7.2, table 2.1].

Huxley's two state model fit exactly with a single relaxation, consistent with our earlier derivation. The five-state model appears to be a close fit but instead to two relaxations. The three- and four-state models are mostly fitted by three relaxations although there are differences on intermediate frequencies. Our fitting procedure using four and five exponential relaxations did not generate appreciable better fits

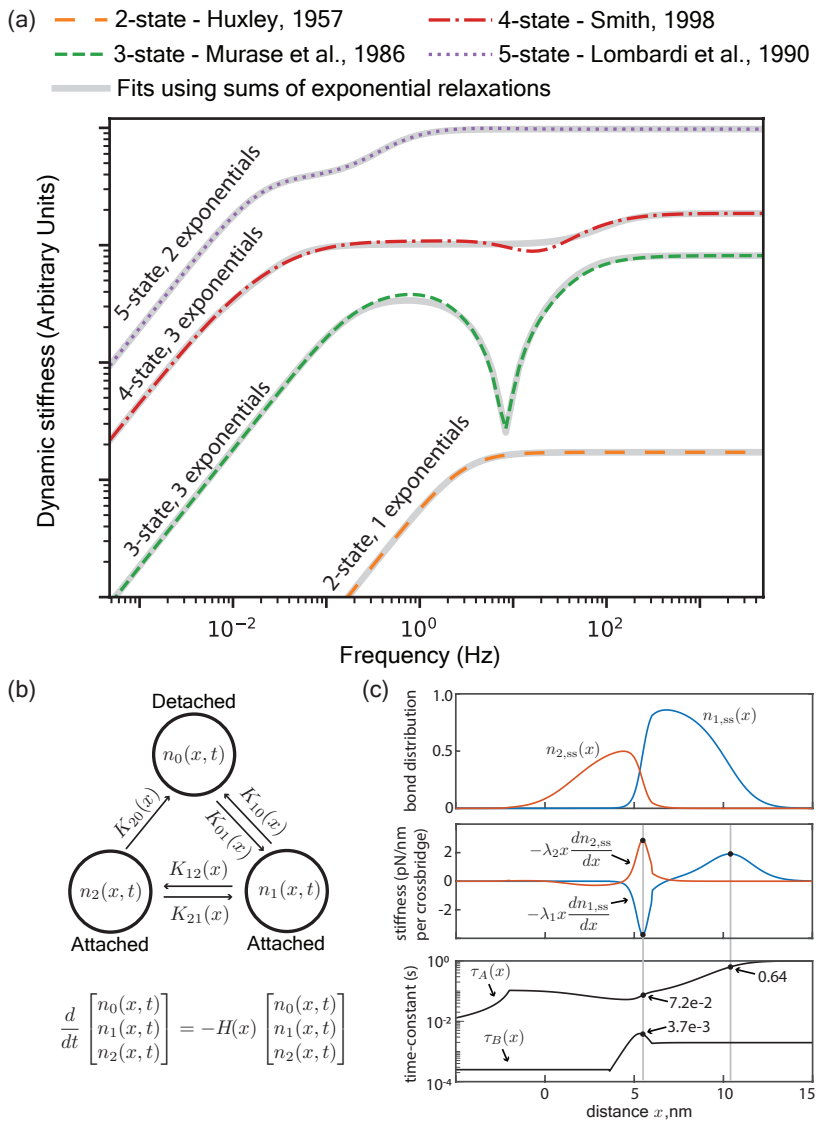

Figure 2.5: (a) The dynamic stiffness of different crosssbridge ensembles are accurately fitted by at most 3 time-constants, each associated with an exponential process [See table 2.1 for fitted values]. The traces are vertically shifted for clarity [see supplementary figure 2.6 for an unmodified plot]. (b) Kinetic scheme of a three-state crossbridge model [71]. The matrix $H(x)$ is a state transition matrix with two non-zero eigenvalues $1/\tau_A$ and $1/\tau_B$. (c) Examination of the derivatives of the steady-state distributions shows that the local peaks accurately identifies the time-constants fitted in table 2.1.

and implies that these crossbridge models incorporate dynamics that cannot be easily distinguished without a large number of time-constants. Overall, the accurate fits demonstrates that, although crossbridge models incorporate a vast parameter space, the rheologies exhibited by their ensemble dynamics are far simpler and dominated

by only a few exponentially relaxing sub-processes.

The fitting process is a general procedure able to find sub-processes acting on vastly different timescales and has been applied to the measured rheology of muscles to identify the dominant sub-processes [41, 74], but how to connect the fitted values to the cycling of crossbridges remains an open question. We use the three-state model as a test case to examine the connection [71]. The model exhibits a significant dip in the dynamic stiffness that is indicative of a negative exponential sub-process that has been attributed to a delayed tension rise observed in a muscle's perturbation response [75]. The three-state model has two attached states with steady-state distributions $n_{1,\mathrm{ss}}(x)$ and $n_{2,\mathrm{ss}}(x)$ and governed by the kinetic scheme illustrated in [figure 2.5b]. Our earlier analysis with equation 2.7 suggests that the derivatives of these distributions drive the perturbation response and that we can heuristically search for local peaks to identify the dominant sub-processes of the three-state model [figure 2.5c]. Namely, we examine $\lambda_1 x dn_{1,\mathrm{ss}}(x)/dx$ and $\lambda_2 x dn_{2,\mathrm{ss}}(x)/dx$ where λ_1 and λ_2 are crossbridge stiffnesses for the first and second attached states, respectively. We find that matching the peaks of these two curves identifies the fitted time-constants [table 2.2] within a 15% error, which is remarkably accurate considering that the fitting process parsed frequencies spanning seven orders of magnitude. This suggests that the fitted sub-processes are measuring these local peaks in the derivative of the steady-state distributions, which correspond to the rising and falling edges of steady-state distributions [figure 2.5c]. To be more precise, the curves to examine should be two separate linear combinations of $\lambda_1 x dn_{1,\mathrm{ss}}(x)/dx$ and $\lambda_2 x dn_{2,\mathrm{ss}}(x)/dx$ rather than each independently but our more detailed analysis show nearly identical results [Appendix 2.8.1].

Our examination of multi-state crossbridge models puts forth the following connection between the exponential relaxation fitted to muscle rheology and the dynamics of crossbridge cycling. Namely, each fitted relaxation results from either a sharp rising or falling edge of the steady-state bond distribution of attached crossbridge states.

Assuming that most crossbridges attach at positive x, the fitted stiffness is positive for a falling edge and negative for a rising edge. The fitted time-constant are associated with the attachment and detachment rates corresponding to the rising or falling edges of the steady-state bond distributions. Furthermore, because the forces arising from the edges are modulated by x, the falling edge at larger x can dominate over the rising edge at smaller x, such as in the case of Huxley's two-state model. Therefore, although the bond distributions themselves may be of a complicated functional form due to the vast parameter space that multi-state crossbridge models tend to require, the emergent ensemble rheology is simpler and dominated by few rising and falling edges. This simplification affords a parameter reduction of multi-state crossbridge models down to two per exponential relaxation, a stiffness and a time-constant, and will allow us to compute the rheological behavior of ensemble crossbridge models in large-scale musculoskeletal simulations in a manner as efficient as phenomenological Hill-type muscle models but without compromising on the mechanistic, crossbridge-based understanding.

2.5 Discussion

Much like Zahalak's distribution-moment formalism, our results simplify the complexity of crossbridge models and connect vastly different scales. But we take a step further and analyze how modeling choices of a single crossbridge cycle give rise to macroscopically measurable quantities, a muscle's bulk rheological characterization. We focused on the dynamic stiffness which generalizes upon notions of elastic stiffness and viscous damping as a viscoelastic property that depend on the time-duration of interest. We showed with numerical computations that the emergent rheology of crossbridge ensembles can be accurately fitted by only a few exponential relaxation processes, without the need for simplifying assumptions about the underlying cross-

bridge model. The fitting procedure can and has been applied to empirical muscle data to identify the dominant exponential relaxations [41, 74], and we show that these relaxation corresponds to either a rising or falling edge in the steady-state bond distributions.

Exponential relaxations have long been used as phenomenological models of muscle rheology. Fading memory models of cardiac studies [76] and Kawai and Brandt models [41, 74] are all sums of exponential relaxations. We showed here that exponential relaxations also arise from the rheology of crossbridge ensembles, and therefore are a common element connecting the microscopic with macroscopic models of muscle. When designing crossbridge models, the modeling choices however complex must map to the exponential relaxations observed in experiments for which three or four are found to accurately capture a muscle's rheology depending the muscle type [41, 74]. Each exponential adds two parameters, a stiffness and a time-constant, so at most eight parameters are justified from length perturbation experiments alone and any additional parameters must be estimated from other experiments. The additional parameters affect forces not included in the linear rheology, namely, nonlinear rheological features and the active contractile forces that operate in parallel to the rheology. On the other hand, when modeling the perturbation response of muscle, exponentials will do as well as detailed crossbridge models but remain grounded to crossbridge theory. Furthermore, using exponentials to compute a perturbation response for any small-amplitude length perturbation can be solved several orders of magnitude faster than directly solving the PDEs of crossbridge models. This computation efficiency affords large-scale biomechanical simulations in real-time, a principal reason why Hill-type muscle models are preferred over detailed crossbridge models in spite of their shortcomings [55–57].

We use the fact that exponential relaxations underlie the ensemble crossbridge dynamics to identify the limits of crossbridge theory in capturing muscle rheology.

One limitation is that exponential relaxations have a finite memory determined by its time-constant, so an ensemble of crossbridges cannot remember its perturbation history far beyond its longest time-constant. Residual force enhancement and force depression are history-dependent phenomena that have implications for the motor control of muscles [77], and are in clear contradiction with having a finite memory. In these phenomena, the forces exhibited by a muscle fiber upon being stretched or shortened to a final length relax towards a value that is persistently higher (force enhancement) or lower (force depression) than if the muscle fiber were isometrically held at the final length. So although forces relax, the muscle fiber always have a memory of being stretched or shortened however long the experimenter waits, unlike exponentials, which suggests that history-dependent muscle phenomena lie outside the purview of current crossbridge models. However, such history-dependence parallels phenomena found in other biological and non-biological materials for which an empirically derived fractional viscoelasticity aptly captures their perturbation response that relax as a power-law rather than an exponential [78–80]. Drawing analogies between muscles and these fractional viscoelastic materials may help to better understand the physical underpinnings of residual force enhancement and depression in muscles.

A second limitation is the neural control of a muscle's perturbation response. Consider a muscle's perturbation response modeled as a single exponential relaxation with coefficient k and time-constant τ that now depend on a neural input u. We argued elsewhere that a requirement on τ is that it increases with neural input u or intracellular calcium concentration [16]. This is to ensure that the same muscle can be used as an elastic structure when maximally activated and as a viscous structure when submaximally activated. We find that the time-constants arising from crossbridge ensembles do not follow this trend. In the simplest implementation of neural control, the number of crossbridges in an ensemble increases with calcium concentration. However, more crossbridges would increase coefficient k but leave τ unchanged

because crossbridge cycling is unaffected. Some crossbridge models incorporate faster crossbridge cycling with higher calcium [63, 64, 81]. While this leads to higher contractile forces, the time-constant would be decrease with higher calcium rather than increase. These arguments may be seen in equations (2.7 - 2.8) for a two-state crossbridge model in which the time-constant does not depend on crossbridge density M and decreases with higher values of attachment f or detachment g.

The mismatches between exponential relaxations, known muscle phenomena, and requirements of neural control all suggest that either crossbridge models currently lack an essential feature or that non-crossbridge elements come into play. There are multiple possible candidate resolutions that we speculate on, may operate in unison, and certainly require further experimental studies. Thick and thin filament compliance between neighboring crossbridges can store elastic energy that dissipate far slower than the crossbridges themselves and affect muscle forces on long experimental timescales [82–84]. Intersarcomeric dynamics may lead to dynamics not captured by single sarcomere model such that the number of participating sarcomeres can drastically alter the rheology of a muscle fiber [85, 86]. Titin can directly modulate force transmission across a sarcomere and therefore may affect crossbridge dynamics [87, 88]. Neural feedback could enforce time-constants as needed depending on motor tasks but is limited by transmission delays on the order of 50ms for humans [9, 10]. All of these possibilities require further research and analysis, but point to a shortcoming in the current crossbridge theory for muscle forces and rheology.

2.6 Conclusions

In this chapter, we analyze the microscopic models of muscle forces to identify a minimal parameter-set that captures the bulk rheological properties of muscle and to provide a mechanistic interpretation of these bulk properties in terms of the micro-

scopic models. Specifically, we performed numerical simulations of ensemble crossbridge models of varying complexities to find a common rheology at asymptotically high and low frequencies. An in-depth analysis into the simplest two-state crossbridge model suggests that the common rheological element is an exponential relaxation of forces, which has an mechanical interpretation as a Maxwell body. We find that crossbridge models differ only in the number of exponential relaxations and that we need at most three to accurately capture their rheologies. So although crossbridge models are complex, their rheologies are more tractable in terms of fewer parameters and lesser computational burden. Exponential relaxations have long been used as phenomenological fits to muscle rheology and our results show how they can be interpreted in terms of the underlying crossbridges dynamics. Thus, this decomposition into exponential relaxations is grounded to crossbridge dynamics yet provides new perspectives into muscle rheology that previously were clouded by the complexity of crossbridge models.

2.7 Methods

2.7.1 Dynamic stiffness calculation of crossbridge models

We detail here the numerical calculation of dynamic stiffness for ensemble crossbridge models. Although each model differs in number of internal states, a general differential equation for the mass balance between states can be written. Let j be the index for the states, then $n_j(x,t)$ is the distribution of crossbridges in the j^{th} state at time t and with distance x to the nearest binding site. The mass balance will take the general form

$$\frac{dn_j(x,t)}{dt} = P_j(x, n_1(x,t), n_2(x,t), ..., N_1(t), N_2(t), ...) \tag{2.13}$$

where $N_j(t) = \int_{-\infty}^{\infty} n_j(x,t)dx$ is the total proportion of crossbridges in state j and P_j is a function that depends on the crossbridge model. We use P_j as given by four different models varying from two to five internal states [59, 71–73].

We impose a step length perturbation of amplitude a and use the output force perturbation response to numerically compute each model's dynamic stiffness. Specifically, we numerically integrate equation 2.13 subjected to the initial condition $n_j(x,0) = n_{j,\mathrm{ss}}(x-a)$ using the explicit fourth-order Runge-Kutta (RK4) scheme [89]. The integration takes time steps of size δt and terminates at a finite time T. The output force perturbation response is a discrete time series ΔF_m indexed in time by m and calculated as

$$\Delta F_m = \sum_j \int_{-\infty}^{\infty} k_j(x - x_{0,j})(n_j(x, m\delta t) - n_{j,\mathrm{ss}}(x))dx \tag{2.14}$$

for stiffness k_j and neutral length $x_{0,j}$ that depends on the j^{th} crossbridge state. The dynamic stiffness $K(\omega)$ is then computed in terms of z-transforms as

$$K(\omega) = \left| \frac{\sum_m \Delta F_m z^{-m}}{\sum_m \Delta L_m z^{-m}} \right|_{z=\exp(-i\omega\delta t)} \tag{2.15}$$

where ΔL_m is the step length perturbation equal to a for all $m \geq 0$ and zero otherwise.

To calculate the dynamic stiffness for Huxley's two-state model [59] in dimensional units, we use parameter values $(f_1, g_1, g_2) = (15, 4, 85)s^{-1}$ provided by (Zahalak and Ma, 1990) [64]. We also used a crossbridge stiffness $k_{\mathrm{xb}} = 0.5\mathrm{pN/nm}$ that is consistent with literature values [72, 73].

2.7.2 Fitting procedure

We detail here the process of fitting exponential relaxations to the dynamic stiffness of different crossbridge models [figure 2.3d]. We denote ω_j as the frequency indexed

by j and logarithmically sampled from $5*10^{-4}$ Hz to $5*10^{3}$Hz. We also denote $K(\omega_j)$ as the numerically determined dynamic stiffness at frequency ω_j. The objective is to find N-pairs of parameters (k_m, τ_m) indexed by m such that the function

$$y(\omega_j) = \left| \sum_{m=1}^{N} k_m \frac{i\omega_j \tau_m}{1 + i\omega_j \tau_m} \right| \tag{2.16}$$

accurately captures $K(\omega_j)$ where N is the number of exponential relaxations to fit and i is the imaginary number. We defined fit to be the N-pairs of parameters (k_m, τ_m) that minimizes the cost

$$\sum_{j} (log(y(\omega_j)) - log(K(\omega_j)))^2 \tag{2.17}$$

where we use the log function to equally weight behaviors at vastly different frequencies. The fit was performed starting at $N = 1$ and N is incrementally increased until there is no appreciable difference between the fits at N and at $N + 1$.

All optimization procedures are performed using the Python 'scipy.optimize' library [90].

Model	k_1	τ_1	k_2	τ_2	k_3	τ_3
Huxley, 1957	0.39	5.3e-2	-	-	-	-
Murase et al., 1996	0.09	0.59	-0.10	6.8e-2	0.15	3.2e-3
Smith, 1997	0.05	2.0	-0.12	3.6	0.20	1.4e-3
Lombardi et al., 1990	0.18	8.0	0.30	0.28	-	-

Table 2.1: Fitted parameters for figure 2.5a. Stiffness values are in units of pN/nm per crossbridge and time-constants are in units of seconds.

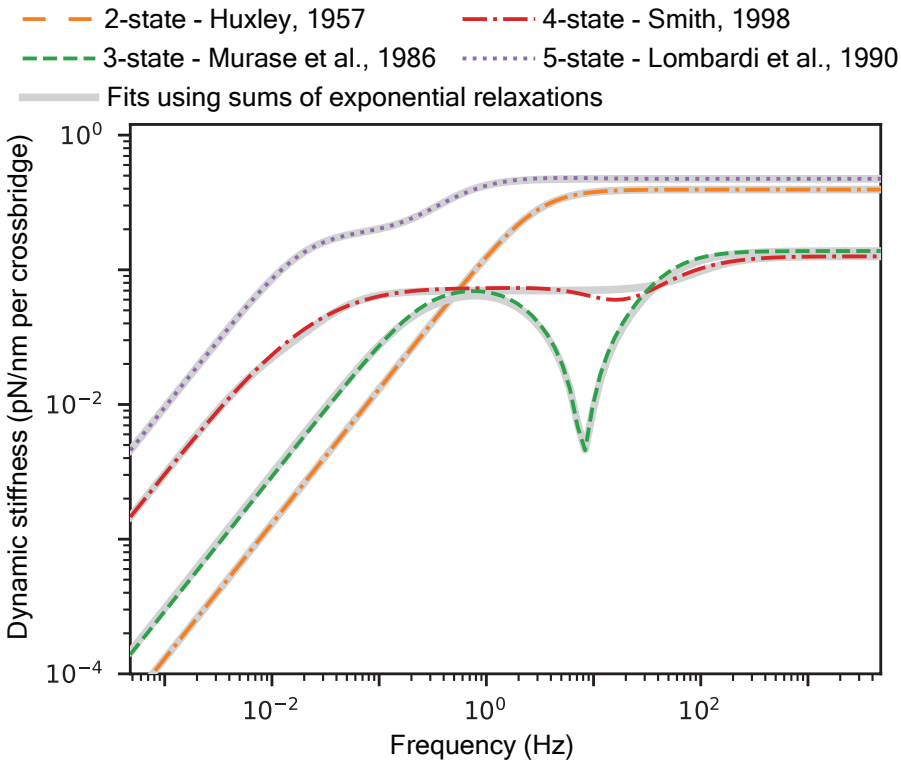

Figure 2.6: Fitted curves to the dynamic stiffness of different crossbridge models.

Model	Fitted time-constants	Search using $xdn_{ss}(x)/dx$
Huxley, 1957	5.3e-2 seconds	5.3e-2 seconds
Murase et al., 1996	(0.59 , 6.8e-2 , 3.2e-3) seconds	(0.64 , 7.2e-2 , 3.7e-3) seconds

Table 2.2: Comparison of fitted time-constants and time-constants identified by using local peaks in the derivatives of steady-state bond distributions for a two-state and a three-state crossbridge model. The peak of xdn_{ss}/dx for the two-state model [equation 2.11] is computed exactly with a time-constant $\tau = 1/(f_1h+g_1h) = 5.3e-2$ seconds.

2.8 Appendix

2.8.1 Perturbation analysis of three-state crossbridge model

We expand here the generalized two-state analysis to the three-state model by (Murase et al., 1986) [71] to identify the dominant time-constants in the system and compare them with the fitted values of table 2.1. In the three-state model, there are two at-

tached states with bond distributions $n_1(x,t)$ and $n_2(x,t)$ and a detached state with distribution $n_0(x,t)$. By defining a column vector $\vec{n} = [n_0, n_1, n_2]^T$, the governing dynamics of the system is given by

$$\frac{d\vec{n}(x,t)}{dt} = -H(x)\vec{n}(x,t) \tag{2.18}$$

$$\text{such that} \quad n_0(x,t) + n_1(x,t) + n_2(x,t) = 1 \tag{2.19}$$

and where $H(x)$ is a 3x3 state transition matrix defined by the kinetic scheme of figure 2.5b. These equations uniquely define the steady-state bond distribution at equilibrium which we denote as $\vec{n}_{\text{ss}}(x)$. Specifically, the state transition matrix has three eigenvector-eigenvalue pairs $(\vec{v}_A(x), 1/\tau_A(x))$, $(\vec{v}_B(x), 1/\tau_B(x))$, and $(\vec{n}_{\text{ss}}(x), 0)$ where τ_A and τ_B are the two time-constants driving the perturbation response and $\vec{v}_A(x)$ and $\vec{v}_B(x)$ are unit vectors.

Mirroring the generalized two-state derivation, the perturbation response to a step length of size a is obtained by setting $\vec{n}(x,0) = \vec{n}_{\text{ss}}(x-a)$ as the initial condition to arrive at

$$\vec{n}(x,t) = \vec{n}_{\text{ss}}(x) + e^{-H(x)t}(\vec{n}_{\text{ss}}(x-a) - \vec{n}_{\text{ss}}(x)) \tag{2.20}$$

$$= \vec{n}_{\text{ss}}(x) - ae^{-H(x)t}\frac{d\vec{n}_{\text{ss}}(x)}{dx} \tag{2.21}$$

where the second equality arises by restricting our attention to small perturbations. We now expand the matrix-vector multiplication on the RHS using eigendecomposition of $H(x)$ as

$$\vec{n}(x,t) - \vec{n}_{\text{ss}}(x) = -a\left(e^{-t/\tau_A(x)}w_A(x)\vec{\nu}_A(x) + e^{-t/\tau_B(x)}w_B(x)\vec{\nu}_B(x)\right) \tag{2.22}$$

where w_A and w_B are linear weights that satisfy the linear system

$$[\vec{\nu}_A(x), \vec{\nu}_B(x), \vec{n}_{\text{ss}}(x)] \begin{bmatrix} w_A(x) \\ w_B(x) \\ 0 \end{bmatrix} = \frac{d\vec{n}_{\text{ss}}(x)}{dx}. \tag{2.23}$$

The third linear weight is necessary zero because $(\vec{n}(x,t) - \vec{n}_{\text{ss}}(x))$ in equation 2.22 must decay to zero and cannot have a component parallel to $n_{\text{ss}}(x)$ which does not decay.

The perturbation response is the first moment of Eqn. 2.22 multiplied by a stiffness vector that maps the bond distributions to forces. It is given in terms of crossbridge density M, stiffness of the first attached state λ_1, and stiffness of the second attached state λ_2 as

$$\Delta F(t) = a \int_{-\infty}^{\infty} \left[k_A(x) e^{-t/\tau_A(x)} + k_B(x) e^{-t/\tau_B(x)} \right] dx \tag{2.24}$$

$$\text{where} \quad k_A(x) = -Mx w_A(x) \langle [0, \lambda_1, \lambda_2]^T, \vec{\nu}_A(x) \rangle \tag{2.25}$$

$$\text{and} \quad k_B(x) = -Mx w_B(x) \langle [0, \lambda_1, \lambda_2]^T, \vec{\nu}_B(x) \rangle. \tag{2.26}$$

The operator $\langle \cdot \rangle$ denotes the dot product between two column vectors. The first entry in the stiffness vector is set to zero to represent the detached crossbridge state. Our analysis of the generalized two-state crossbridge model suggests that dominant time-constants appears where either $k_A(x)$ or $k_B(x)$ are localized, and we find that these time-constants do not significantly differ from heuristically using the derivatives of the steady-state distributions [figure 2.7].

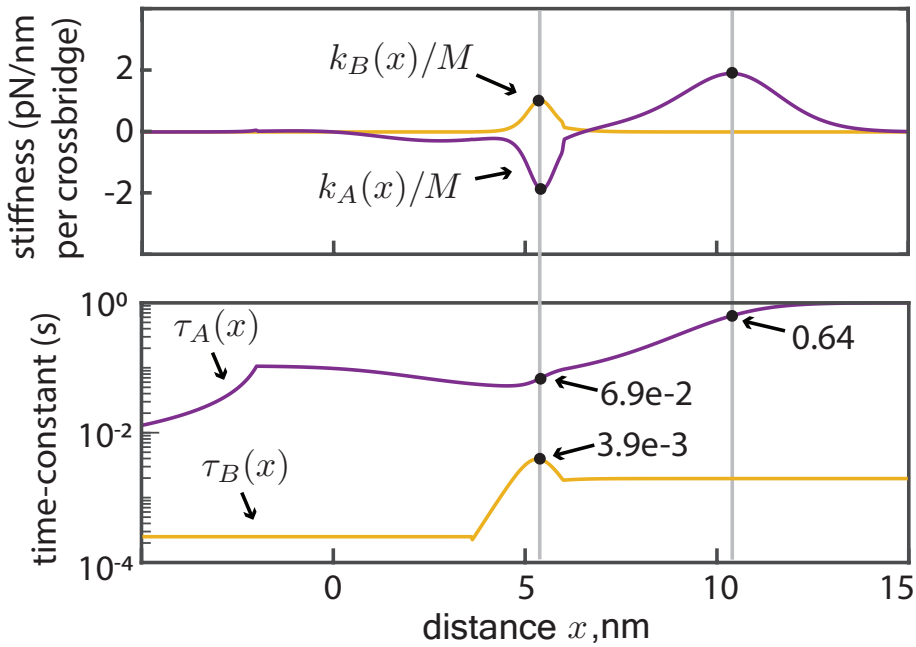

Figure 2.7: Examination of the local peaks in stiffnesses $k_A(x)$ and $k_B(x)$ identifies the dominant time-constants. The stiffnesses are computed using an eigenvector analysis of the state-transition matrix $H(x)$ and are different from $\lambda_1 x dn_{1,\mathrm{ss}}(x)/dx$ and $\lambda_2 x dn_{2,\mathrm{ss}}(x)/dx$ used in figure 2.5c as a heuristic search. The identified time-constants do not significantly differ from the values found in figure 2.5c.

Chapter 3

Rheological basis of skeletal muscle work loops

3.1 Abstract

How skeletal muscle exerts forces in response to stretch is its rheology, a mechanical resistance central to animal locomotion and a property subject to control by neural or electrical stimuli. The plot of forces versus an externally imposed oscillatory stretch is a closed force-length loop that is a graphical signature of the rheology and is well-studied under both fixed and time-varying stimuli. Under fixed-stimuli, the oscillatory stretch probes a constant rheological state of muscle and results in a force-length loop characteristic of passive materials. But under time-varying stimuli, the rheological state is changing and the corresponding force-length loop, referred to as a work loop, exhibits functionally critical features not found in passive materials but which underlie the mechanical actuation by skeletal muscles. However, how to interpret work loops and these features as a rheological behavior of skeletal muscle is not well understood. In this chapter, we hypothesize that work loops emerge by splicing together underlying fixed-stimuli loops at different junctions. Using published muscle datasets and a detailed sarcomere model, we find that the hypothesis accurately predicts work loop shape and, consequently, allows a formulation of skeletal muscle work loops in terms

of rheological behaviors measured at fixed-stimuli.

3.2 Introduction

Rheology, or how materials respond to being deformed, is a central consideration for living materials [80, 91, 92]. Many biological tissues may be considered tunable because their functionality arises from a modulation of their rheological properties by an external control parameter or a stimulus [93]. One tunable material of considerable relevance to animals [26, 94], and the object of much engineering mimicry [27, 95, 96], is skeletal muscle. A skeletal muscle's rheological behavior is actively regulated by the nervous system and is crucial for how animals control their body movements [16, 97].

There are several broad groups of experimental characterizations of skeletal muscle rheology that each provide a different cross-sectional view of muscle phenomena. Isometric and isotonic measurements capture the steady forces developed by muscle as a function of its length and shortening velocity [7, 98]. Transient forces in response to step length, step velocity, and twitch perturbations capture the initial fast response and history-dependent relaxation to steady-state [15, 51, 99, 100]. Oscillatory rheological experiments, or sinusoidal analysis, measure the frequency-dependent storage and loss moduli under fixed neural or electrical stimulation and length oscillations [41, 101]. And lastly, work loop analysis capture the mechanical actuation of muscles when they are simultaneously subjected to time-varying stimulation and length oscillations [23, 102]. Underlying all these broad groups are biophysical models of actomyosin crossbridges that form the internal motor machinery of muscle [15, 59]. The connection of scales between molecular crossbridge dynamics and macroscopic rheological characterizations, however, remain difficult owing to the numerous mechanochemical parameters employed in crossbridge models that cannot be directly measured. As a result, the broad groups remain as separate and distinct rheological

characterizations. In this chapter, we hypothesize and test a connection between two of the broad groups, namely oscillatory rheological experiments and work loops. Such connections between different rheological characterizations can help illuminate new understandings of muscle phenomena and, in this case, provide a rheological basis for the shape of skeletal muscle work loops.

Work loop analysis is prevalently applied to study a skeletal muscle's forces in response to an externally imposed oscillatory length perturbation while it is actively regulated by neural or electrical stimuli [23, 102]. The trajectory obtained by plotting the imposed oscillatory perturbation with the recorded force response forms the work loop, which is a graphical signature of the dynamics and work-producing capabilities of skeletal muscles [26, 98]. The shape of work loops is an important determinant of the biomechanical functions that the muscle provides [97]. It depends on the precise timing of the stimulus, the frequency of oscillation, the muscle's physiological properties, and other factors that are still vigorously debated [22, 23, 97, 98]. As a result, we currently lack a cohesive framework to understand and predict the emergence of complex work loop shapes. For example, two cockroach leg extensor muscles that appear nearly identical under isometric or isotonic force characterizations generate loops of markedly different shapes, implying different functional consequences to the cockroach [24, 25].

The difference between oscillatory rheological experiments and work loop analysis is that one involves fixed neural or electrical stimulation whereas the other involves time-varying stimuli. A question that arises is if a detailed accounting of the time-varying stimuli permits a characterization of work loops in terms of rheological properties measured at fixed-stimuli. The tunable nature of skeletal muscles, however, presents several hurdles. For example, under fixed-stimuli, a muscle follows a force-length trajectory that shares similarities with other soft and passive materials [95, 96, 103, figure 3.1a]. But when the rheology is changing in time due to

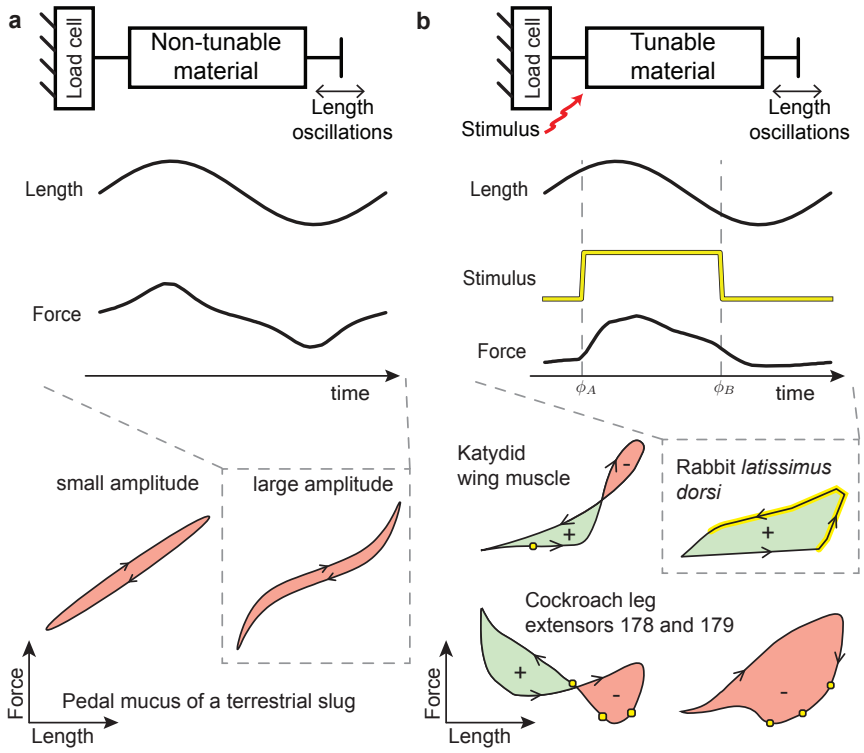

Figure 3.1: **Comparison of measured force-length loops in non-tunable and tunable materials. a**, Oscillatory rheology of a passive non-tunable material (pedal mucus of a terrestrial slug, *Limax maximus*) for small and large amplitudes [adapted from 104]. **b**, Work loops under time-varying stimuli of the wing muscle of a katydid (*Neoconocephalus triops*), rabbit *latissimus dorsi* muscle, and cockroach leg extensor muscles 178 and 179 [adapted from 23, 24, 98, respectively]. Yellow dots and thick yellow lines indicate discrete and continuous stimulation, respectively. The loops have been rescaled for visual comparison. Positive and negative mechanical work output are shaded green and red, respectively. All loops shown are taken from experimental measurements.

variable stimuli, the trajectory is far more complex and exhibits loop features like self-intersections and directional changes between clock-wise and counter-clockwise loops that passive materials do not show (figure 3.1b). Here, we build upon current fixed-stimuli rheological characterizations and admit tunability under a specific hypothesis and examine to what extent measurements from oscillatory rheological experiments can explain the emergent shape of skeletal muscle work loops.

In this paper, we develop and test the hypothesis that skeletal muscle work loops measured under time-varying neural or electrical stimulation emerge by transitioning

between underlying fixed-stimulus force-length loops. We term this the splicing hypothesis which forms the foundations for our mathematical framework. The paper starts with preliminaries to introduce and define ideas of oscillatory rheology and linear viscoelasticity. We then present the mathematical formulation of the splicing hypothesis and derive a minimal parameterization for the space of all possible loop shapes obtained using a singular version of the splicing hypothesis where the transition between force-length loops is assumed to be instantaneous. The space of loop shapes lends insights into different modes of mechanical actuation that can arise as a result of a skeletal muscle's tunable rheology and forms the premise for understanding the shapes that emerge under more gradual transitions. We then show two parallel validations of our mathematical framework using published work loops of short-horn sculpin (*Myoxocephalus scorpius*) abdominal muscles and using direct numerical simulations of a detailed biophysical sarcomere model. We then discuss the implications of our framework for muscle modeling and experiments.

3.3 Preliminaries

3.3.1 Oscillatory rheology

Oscillatory rheology characterizes materials with invariant properties by generalizing upon notions of stiffness and damping to steady dynamical conditions [103, 105]. To do so, the material's force (or stress) response to sinusoidal length (or strain) perturbations of different frequencies and amplitudes are characterized by force-length loops, otherwise known as Lissajous figures [106], that provide a graphical signature of the material's rheology [103]. The force-length loops are approximately elliptic for small amplitude oscillations, but are typically non-elliptic for larger amplitudes (figure 3.1a). For small amplitudes, the complex modulus $E(\omega) = E'(\omega) + i\,E''(\omega)$ captures the material's dynamic response and generally depends on the oscillatory

frequency ω [103].

The storage modulus $E'(\omega)$ and loss modulus $E''(\omega)$ are respectively the in-phase and out-of-phase components of the measured force divided by the imposed length amplitude. The storage and loss moduli have been widely applied to muscle [41, 67, 101, 107] and other natural and engineered tunable materials [80, 91, 108], so long as the external stimulus is held constant. Although *in vivo* muscle strain is often greater than the small amplitudes used in oscillatory tests, the loss and storage moduli have helped develop predictive models for muscle's dynamic response [107, 109, 110] and guided the interpretation of *in vivo* data [5, 67].

Non-elliptic force-length loops can occur in response to large amplitude oscillations that probe nonlinear rheological behaviors, for example, an inherent stress or strain dependence of the moduli, within muscles and other materials [103–105, 111, figure 3.1a]. The nonlinearities are understood to be embedded within higher order terms of a Fourier expansion whose leading order terms are the storage modulus E' and loss modulus E''[104, 105]. We shall formulate our mathematical framework in terms of the leading order storage and loss moduli and focus on the linear oscillatory rheology of skeletal muscles because of the vast experimental literature that currently exist on them [41, 101]. The generalization to non-elliptic loops, however, is a direction extension of the framework by an inclusion of the higher order terms (see Appendix 3.8.1).

Sign convention: Following the muscle literature [23], we take a sign convention in which increasing length is positive but positive forces imply the opposite sense, namely contraction. So a positive or counter-clockwise loop is when the material performs work on the environment, and a negative or clockwise loop is when the material absorbs work ('+' and '−' regions in figures 3.1 and 3.2).

3.4 Mathematical framework

3.4.1 Tunable oscillatory rheology

Current rheological methods under a fixed stimulus do not directly accommodate the complex loop shapes that arise under a time-varying stimulus (figure 3.1b for example). We extend current methods and incorporate a time-varying element using a new hypothesis: splicing together fixed-stimulus force-length loops at different junctions predicts the shape of complex work loops.

We first illustrate the hypothesis by way of example and then state its mathematical formulation. Consider three idealized tunable elements, a Hookean spring with tunable stiffness and neutral length, a Newtonian damper with tunable viscosity, and an ideal force generator with tunable force output. The force generator accommodates the isometric forces a muscle exert when stimulated. The force-length loops for these idealized elements under a constant stimulus are a sloped line for the Hookean spring, a horizontal clockwise ellipse for the Newtonian damper, and a flat line for the ideal force generator. Periodically switching the properties of the idealized elements—stiffness, neutral length, damping, or force level—between two set of constant values or changing the timing of switching result in more complicated loops that exhibit reversals and self-intersections (figure 3.2a).

We can generalize the idea from the simpler idealized elements to tunable linear viscoelastic materials by mapping stiffness to a storage modulus and viscosity to a loss modulus. Combining the two moduli with the ideal force results in a vertically sheared ellipse (figure 3.2b). The storage modulus controls the amount of vertical shear, the loss modulus controls the enclosed area, and the ideal force shifts the entire figure up or down. Thus, under a time-varying stimulus that modulates all three rheological properties, a complex force-length loop emerges by switching between two sheared

ellipses, each of which correspond to a distinct rheological state. Consider a tunable material that has a greater storage modulus, loss modulus, and ideal contractile force at rheological state A compared to state B, implying a more inclined, wider, and vertically offset ellipse for A than B (figure 3.2c). Periodically switching the rheological states from B to A and back to B would result in a splicing of the two ellipses to form the more complicated loop. For this illustration, assume that the time taken to switch and settle into the new rheological state is negligible compared to the period of the oscillation. Generically, there are two target points to jump to upon switching, but only one will traverse the loop in a direction consistent with its loss modulus, thus fully defining a new spliced loop built up from underlying sheared ellipses. This spliced loop exhibits self-intersections and net positive work although both the A and B ellipses are individually dissipative.

3.4.2 Splicing hypothesis

We state here the mathematical formulation of the hypothesis. When phasically stimulated during $\phi_A \leq \omega t \leq \phi_B$, for oscillatory frequency ω, time t, junctions ϕ_A and ϕ_B of switching between rheological states, the force response $F(t)$ to a sinusoidal length perturbation $L(t) = \Delta L \sin(\omega t)$ of amplitude ΔL is found by splicing the forces $F_B(t)$ and $F_A(t)$ corresponding to the two different rheological states A and B, respectively, and expressed as,

$$F(t) = \begin{cases} F_A(t) & \text{for } \phi_A \leq \omega t \leq \phi_B, \\ F_B(t) & \text{otherwise.} \end{cases} \tag{3.1}$$

The force-length loops obtained by graphing $F_A(t)$ and $F_B(t)$ against $L(t)$ introduce the notion of loops that are produced under a constant rheological states A and B. Given the loops corresponding to $F_A(t)$ and $F_B(t)$, the force response is completely

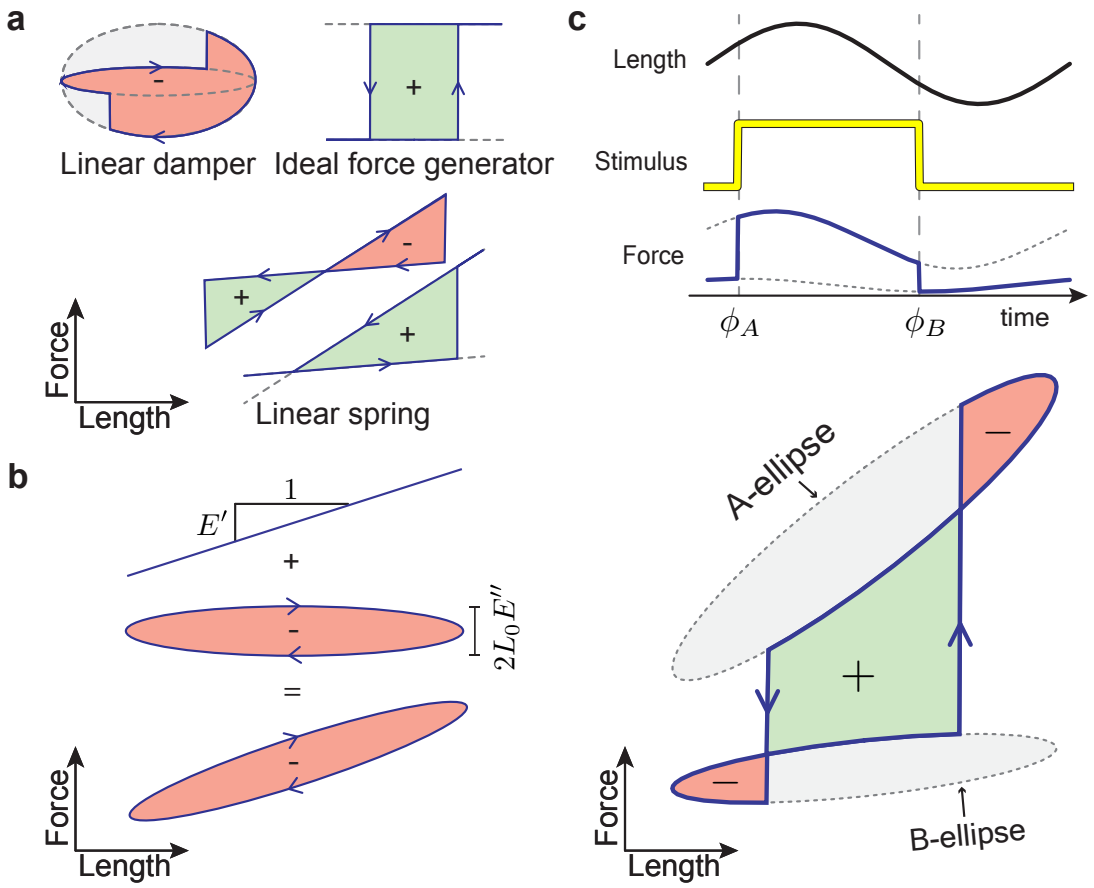

Figure 3.2: **Sketches to illustrate the splicing hypothesis. a,** Hypothetical work loops for idealized tunable elements. **b,** The force-length loop for a linear material is a sheared ellipse, which is the sum of a sloped line (elastic component) and a clockwise horizontal ellipse (viscous component). **c,** Splicing the state A ellipse and state B ellipse results in a new work loop.

described by a vector $[\phi_A, \phi_B]$ and the loops form a basis for all possible force responses that can arise from different choices of phasic timing. We refer to these loops as basis loops. In addition to the rheological state, these basis loops depend on the oscillation frequency and amplitude. They are elliptic for linear materials but could generally be non-elliptic. The spliced loop can be interpreted as an emergent periodic orbit of a piecewise smooth dynamical system (figure 3.2 - Figure Supplement 1). The tunable material's rheological states, the basis loops, are the constitutive pieces of the piecewise system. We refer to the construction of work loops from basis loops as splicing (figure 3.2c, equation 3.1).

3.4.3 Shape-space of spliced loops

Shape is an important feature of work loops and directly embeds not only the net mechanical work a tunable material performs but also the type of mechanical actuation the material provides. Specifically, in the case of muscle [97], whether it performs mechanical work as a tunable spring, tunable dashpot, or tunable ideal force generator has vastly different biomechanical implications even though the net mechanical work performed may be identical [16]. A tool that the splicing approach affords is a parameterization of loop shape in terms of oscillatory rheological characterizations and therefore also a rheological basis for the mechanical actuation that muscle provides based on loop shape. We show here the derivation of the parameterization and present a two-dimensional space of all possible loop shapes that can arise from splicing together basis loops.

For this derivation, we use linear rheological response of tunable materials where the material at a constant rheological state is fully described by an ideal force term, and the storage and loss moduli. The analysis for nonlinear rheological responses is a direct extension of the linear theory but adds additional storage and loss moduli parameters that correspond to higher harmonics (Methods 3.8.1). The oscillatory force response $F(t)$ of a tunable material that is phasically stimulated between rheological states A and B depends on the ideal force terms F_{A0} and F_{B0}, the storage moduli E'_A and E'_B, the loss moduli E''_A and E''_B, and length amplitude ΔL, according to,

$$F(t) = \begin{cases} F_{A0} + \Delta L \ \left(E'_A \sin\omega t + E''_A \cos\omega t\right), \ \text{for } \phi_A \leq \omega t \leq \phi_B, \\ F_{B0} + \Delta L \ \left(E'_B \sin\omega t + E''_B \cos\omega t\right), \qquad \text{otherwise.} \end{cases} \tag{3.2}$$

Atypical loop shapes, which are not seen in nontunable materials, emerge from phasic changes in rheological states. Therefore, it is the difference between the two rheological states that introduces new loop features (figure 3.3a). We sub-

tract the force response $F_B(t)$ from $F(t)$, and derive nondimensional expressions using the length scale ΔL, force scale $(F_{A0} - F_{B0})$, and timescale $1/\omega$. In terms of the nondimensional phase $\phi = \omega t$, the stimulated nondimensional force response $f_A(\phi) = (F_A(t) - F_B(t))/(F_{A0} - F_{B0})$ is expressed using the difference in moduli $\Delta e' = \Delta L(E'_A - E'_B)/(F_{A0} - F_{B0})$ and $\Delta e'' = \Delta L(E''_A - E''_B)/(F_{A0} - F_{B0})$ as,

$$f_A(\phi) = 1 + \Delta e' \sin\phi + \Delta e'' \cos\phi. \tag{3.3}$$

We recast the modulus parameters $\Delta e'$ and $\Delta e''$ in terms of the nondimensional work w' and w'' that is performed by the material as a result of switching the storage and loss moduli respectively, and an additional work w_0 as a result of switching the ideal force component between F_{B0} and F_{A0}. Thus, the nondimensional sinusoidal length perturbation is $\ell(\phi) = \sin(\phi)$ and the force response $f(\phi)$ is

$$\begin{aligned} f(\phi) &= \frac{F(t) - F_B(t)}{F_{A0} - F_{B0}} \\ &= \begin{cases} 1 + \frac{w'}{w_0}\,\frac{2}{\ell_A + \ell_B}\sin\phi + \frac{w''}{w_0}\,\frac{\ell_B - \ell_A}{\beta}\cos\phi, \\ \qquad\qquad\qquad \text{for } \phi_A \le \phi \le \phi_B, \\ 0, \ \text{otherwise.} \end{cases} \end{aligned} \tag{3.4}$$

The shape factor $\beta = \int_{\phi_A}^{\phi_B} \cos^2\phi\, d\phi$ represents the partial area of the loss-ellipse traversed in switching the rheology, and $\ell_A = \ell(\phi_A)$ and $\ell_B = \ell(\phi_B)$ are the dimensionless lengths at switching from A to B and then from B back to A, respectively. The nondimensional work w' for switching the elastic modulus, w'' for switching the loss modulus, and w_0 for switching the ideal force term are,

$$w' = -\Delta e' \int_{\ell_A}^{\ell_B} \ell d\ell = \frac{1}{2}\Delta e'(\ell_A^2 - \ell_B^2), \tag{3.5}$$

$$w'' = -\Delta e'' \int_{\phi_A}^{\phi_B} \cos^2\phi d\phi = -\Delta e''\beta \tag{3.6}$$

$$w_0 = -\int_{\ell_A}^{\ell_B} d\ell = \ell_A - \ell_B, \tag{3.7}$$

and the nondimensional and dimensional net work per loop are respectively,

$$w_n = \oint f d\ell = w_0 + w' + w'', \text{ and} \tag{3.8}$$

$$W_n = w_n \Delta L(F_{A0} - F_{B0}) - \pi E_B'' \Delta L^2. \tag{3.9}$$

Expressing the force response, and thus the loop shape, using work ratios aids in the interpretation of the response under time-varying stimuli in terms of the material's functionality as a force actuator, elastic body, or viscous damper (figure 3.3b). The choice of shape parameterization also delineates the rheological states A and B from the effect of the stimulus protocol that are captured by the parameters $(\ell_B + \ell_A)/2$, and $\beta/(\ell_B - \ell_A)$. Current approaches to functionally interpreting skeletal muscle work loops are based on qualitative observations about the positive and negative regions of the loops [23, 102]. The shape-space provides a quantitative means to understand the net effect of the shape in terms of relative work contributions from the storage and loss moduli underlying the rheological response relative to the ideal force term. Therefore, the coordinates of a loop in the shape-space provide a quantitative functional interpretation of the loop.

Although the veracity of the shape-space remains to be tested, the splicing approach provides a single framework in which to view vastly different loop shapes. For example, different loop shapes may arise from the same material simply by varying the oscillatory frequency and holding all else constant (figure 3.3c). This is because

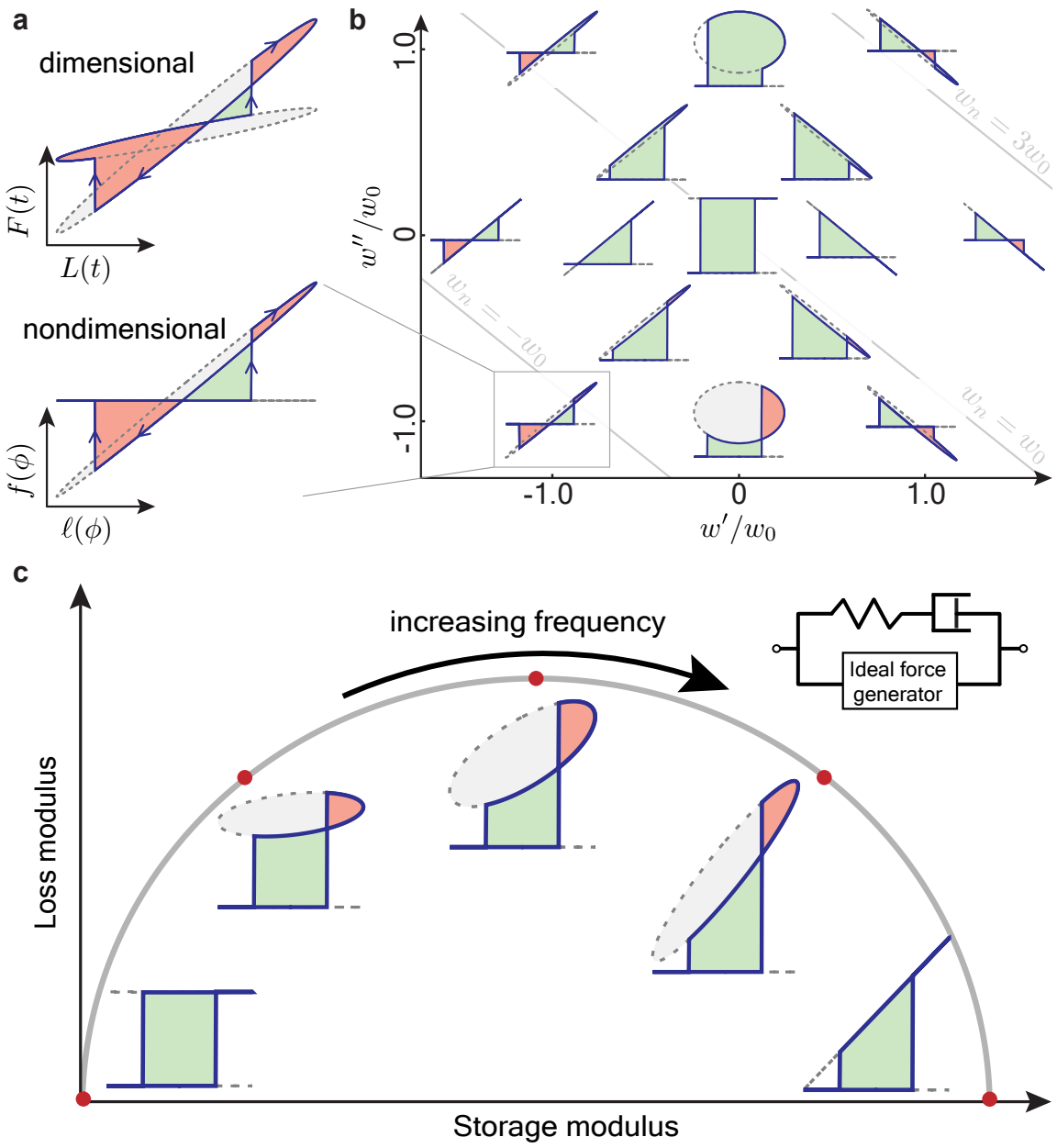

Figure 3.3: **Shape-space of spliced loops. a,** Representative loops to illustrate nondimensionalization of loop shape. **b,** Two work ratios define the shape-space of spliced loops, one measures the net mechanical work by variable elastic modulus and the another the work by variable loss modulus. The loops are scaled to have the same width and height and shown here for one stimulation protocol ($\phi_A = \pi/6$ and $\phi_D = 5\pi/4$). Contour (gray) lines of net work w_n are also shown. All loops shown are computed using equation (3.4). **c,** Example of traversing the shape space for an ideal force generator in parallel with a tunable Maxwell body, a spring and dashpot in series, which exhibits vastly different loop shapes simply by changing the oscillatory frequency (Methods 3.8.2).

the material's rheological properties are frequency-dependent. The splicing approach enables the application of rheological modeling to generate predictions for skeletal muscles when it is subjected to varying stimuli. It may also prove to be a tool for designing actuators and programmable mechanical interfaces from tunable materials other than skeletal muscles because it is now possible to predict the range of loop shapes a material can exhibit and consequently the exchange of mechanical work with its environment.

3.5 Results

The splicing hypothesis and its constitutive pieces are tested here using published muscle data and numerical simulations. We first show direct evidence for the passive basis loops in rat papillary muscles by graphically overlaying their force-length loops when deactivated and when subjected to a single electrical spike. We then test whether the splicing hypothesis accurately predicts loop shape using a dataset of work loops collected from short-horn sculpin (*Myoxocephalus scorpius*) abdominal muscle. These work loops differ only in the phasic timing of an electrical stimulus and, according to the splicing hypothesis, arise from the same set of basis loops. Because the rat and sculpin work loops were not specifically collected to test splicing, we also implement a biophysical model of the sarcomere that incorporates calcium activation to compare predictions of the splicing hypothesis with computed work loops.

In connecting theory with data and simulations, it is important to define stimulus and rheological states in the context of muscles. The stimulus is an external control parameter that varies muscle behavior and can take different forms depending on experimental protocol. It may be calcium concentration, binding affinity of actomyosin crossbridges, frequency of neural inputs, or frequency of electrical spikes that directly modulate the motor machinery of muscle. The degree of engagement of the motor

machinery, specifically the bond distributions of actomyosin crossbridges [15], is the muscle's rheological state that underlies its viscoelastic resistance to length perturbations. The distinction between stimulus and rheological state introduces several complications in examining muscle data. An example to be encountered with sculpin work loop data is that the transition between rheological states is slower than changes in the stimulus. The stimulus may also be a function of length perturbations because of stretch-induced calcium release or heat production and the notion of a fixed-stimuli rheological state during measurement becomes less well-defined [51, 112].. Furthermore, because there are multiple possible stimuli, holding one constant does not imply that the others are constant so a fixed-stimulus rheological state is not one of all possible stimuli being constant, but one in which the stimulus under experimental control is held constant. Recognizing all these complexities about muscle, the question we ask in examining work loop data and sarcomere models is if a superposition of rheologies measured at fixed-stimuli adequately captures the tunable rheology measured for time-varying stimuli.

3.5.1 Rat papillary work loops

Work loops of rat papillary muscles show evidence for one of the basis loops corresponding to a low stimulus, namely the analog to the B-ellipse in figure 3.2c that has a weaker rheological response compared to the A-ellipse. Although papillary muscles are cardiac rather than skeletal muscles, they are similar based on the fact that they both are underlied by the mechanics of sarcomeres. Baxi et al. [111] overlays work loops measured for a single electrical impulse with passive force-length loops of rat papillary muscles on the same plot. The work loop closely traces the passive loop up to onset of the electrical impulse (figure 3.4a), providing direct evidence which shows that the passive loop is a basis loop corresponding to an unstimulated papillary muscle. But Baxi et al. [111] did not measure a basis loop when the papillary muscle was

stimulated. This could be because stretching highly activated muscles often induces tissue damage [49], thus making it experimentally infeasible to directly measure basis loops of an activated muscle at large strains.

3.5.2 Sculpin work loops

Although direct measurements of basis loops under high neural or electrical stimulus are not currently available, we show a means to infer them by pooling data from multiple work loop measurements of the same muscle. By using the inferred basis loops, we show how to apply splicing and predict work loops with which to compare with measured work loops. For this analysis, we use a previously published dataset consisting of twelve work loops from a short-horn sculpin (*Myoxocephalus scorpius*) muscle [113] subjected to a 5% strain amplitude and a 5Hz oscillatory frequency. In that study, three successive electrical spikes spaced 20 ms apart were applied per cycle and the onset of the first stimulus relative to the length oscillation was systematically varied from 0° to 360° phase lag to produce twelve work loops that vary considerably in their shape (figure 3.4b). Because the twelve loops differ only in stimulus timing, the sculpin dataset provide a testing ground of the splicing hypothesis because they are, in theory, underlay by the same set of basis loops.

A complication arises that unlike the simplified illustration of the splicing approach (figure 3.2), the effect of the stimulus on muscle is not instantaneous nor is it constant for the entire duration. Instead, work loop measurements typically apply impulsive neural or electrical spikes that cause a gradual rise and fall in intracellular calcium concentration, which in turn leads to a gradual engagement and disengagement of the muscle's motor machinery. The degree of engagement of the motor machinery is the rheological state that affects force production, but it is often experimentally inaccessible or difficult to quantify. We overcome this inaccessibility and approximate the rheological state using independent experimental measurements of the force twitch

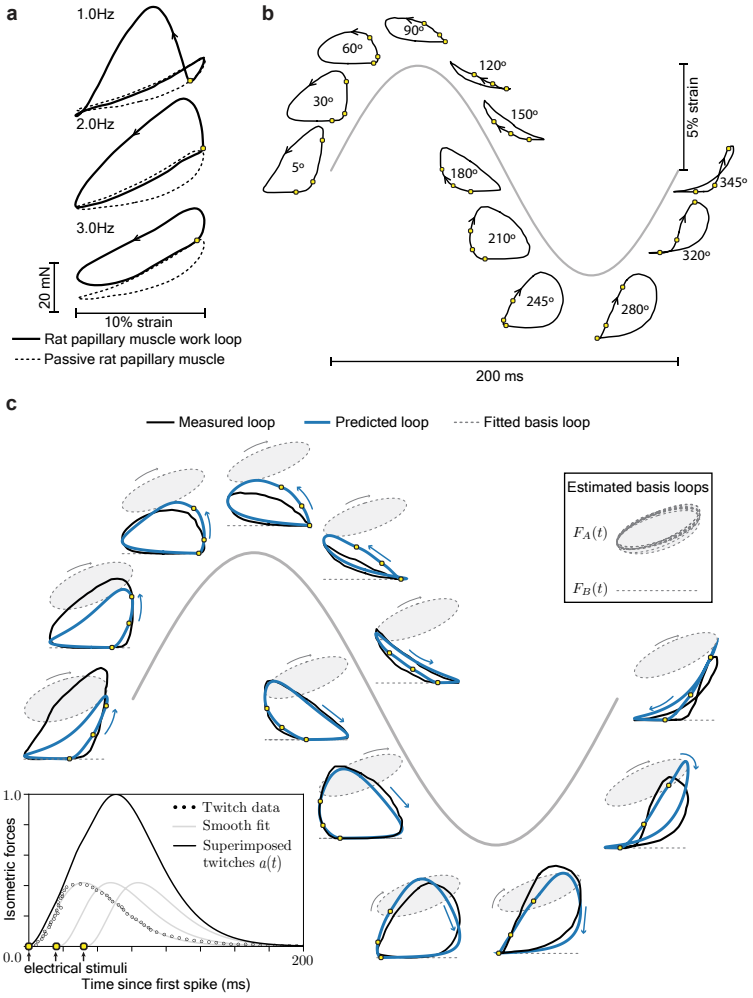

Figure 3.4: **Work loops, basis loops, and gradual transitions. a,** Passive force-length loops and works loops of rat papillary muscle show that measured work loops trace closely along the passive loop up to the electrical spike (yellow dot) that actives the muscle's motor machinery [adapted from figure 3 of 111]. **b,** Work loops from a short-horned sculpin abdominal muscle measured at 5Hz and 5% strain amplitude and for different stimulation protocols [adapted from figure 4 of 113]. Three electrical spikes were applied in each cycle (yellow dots). Work loop locations on the sine wave indicate the phase difference between the first stimulus and the length oscillation. **c,** A leave-one-out analysis to estimate the stimulated basis loop (grey shaded ellipses), used to predict the work loop (blue), and compare with measurement (black). The slow transition in rheological states is modeled using the isometric twitch response to a single electrical spike to construct an interpolation variable $a(t)$. The twitch response was found from separate measurements of the short-horned sculpin abdominal muscle (bottom-left inset) [adapted from figure 1b of 114].

response to a single electrical spike under isometric conditions [114]. Because the length is constant, the time-course of the force development and decay reflects the

engagement of the motor machinery. The pulse duration in the isometric twitch study was 1 ms, different from 2 ms that was used in the sculpin dataset. But both are much smaller than the 20 ms inter-spike interval, the ∼100 ms force rise and relaxation time, or the 200 ms time period of the oscillation. So we treat the stimuli in both studies as impulses. Furthermore, the work loop protocol used three successive electrical spikes. We find the total response to three spikes using a superposition of three twitch responses and rescale the response to lie between zero and one to yield a normalized interpolation variable $a(t)$ (bottom left inset of figure 3.4c, and Methods 3.8.3) that embeds within it the dynamics between stimuli and rheological states. This procedure uses the single-spike response to construct the response to more generalized inputs, three spikes in this case, and is similar to past applications of impulse responses in neural systems involving sensory [115] and motor activation dynamics [116].

We modify the splicing approach of equation (3.1) to accommodate the sculpin muscle's continuously varying rheological state by using the normalized interpolation variable $a(t)$. The geometric picture for this modification is that the measured force reflects an intermediate rheological state that a muscle transiently passes through at any point in time. The interpolation variable $a(t)$ specifies this intermediate rheological state such that when $a(t)$ gradually changes from zero to one, the sculpin work loop transitions from one basis loop corresponding to $F_B(t)$ to another corresponding to $F_A(t)$. Using standard practice to linearly relate forces [7], and for an onset time t_0 when the stimulus is first applied, the mathematical representation of this modification of equation (3.1) to permit a slow transitioning between rheological states A and B is

$$F(t) = a(t - t_0)F_A(t) + (1 - a(t - t_0))F_B(t). \tag{3.10}$$

The measured passive loop is generally non-zero much like the Baxi et al. study [111],

but we assume it to be zero in the sculpin dataset because the stimulated loop $F_A(t)$ appears to be the dominant rheological structure. Furthermore, we parameterize the stimulated basis loop using an ideal force term F_{A0}, storage modulus E'_A, and loss modulus E''_A. Thus, for an applied length oscillation of amplitude ΔL, frequency ω and a stimulus onset time t_0, the predicted spliced response is simplifies from equation (3.10) by taking $F_B(t) = 0$ as

$$F(t) = a(t - t_0)(F_{A0} + \Delta L E'_A \sin \omega t + \Delta L E''_A \cos \omega t). \tag{3.11}$$

The interpolation variable a, stimulus onset time t_0, and amplitude Δ are all externally specified which leaves the three rheological parameters (F_{A0}, E'_A, and E''_A) of the stimulated basis loop to be determined. In the more general case where the passive loop cannot be ignored, the passive loop adds three additional rheological parameters to be determined.

We estimate the three parameters (F_{A0}, E'_A, and E''_A) by fitting the sculpin work loop data to equation (3.11) in a leave-one-out analysis to test the splicing hypothesis (Methods 3.8.3). Briefly, the analysis excludes one work loop from the dataset of twelve loops and uses the remaining eleven to estimate the three parameters. The estimated parameters are then used to generate a prediction that is compared that with the excluded loop (figure 3.4c). We repeat this procedure for all twelve loops, generating a different triplet (F_{A0}, E'_A, and E''_A) for each and avoiding a tautological use of the dataset in which a measured loop is used to generate its own prediction.

We quantitatively compare the loops generated by the leave-one-out analysis and the measured sculpin work loops using Pearson's correlation coefficient and net mechanical work performed as goodness of fit measures. These measures are plotted in figure 3.4 - Figure Supplement 1 as functions of the stimulus timing. The Pearson's correlation coefficient compares the predicted force response and the measured force

response (see Methods 3.8.3), and a value close to one implies a strong correlation. We find that it ranges from 0.90-0.99 for all loops. The net mechanical work performed is a standard measure in work loop analysis to compare loops [98, 117, 118], and we find it to be similar for all pairs of measured and predicted loops except for the 5° and 30° loops. The estimated stimulated basis loop, *i.e.* the fitted triplet (F_{A0}, E'_A, and E''_A), can also serve as a quantitative comparison and we find it to be almost unchanging across all twelve instances of the leave-one-out fitting procedure (top-right inset of figure 3.4c, Figure 3.4 - Table Supplement 1). Based on these comparisons, we find that the predicted loops generated by the splicing hypothesis accurately captures the experimentally measured sculpin work loops.

Future investigation is needed, but we speculate that the slightly worse predictions when the stimulation phase is near 0° might be due to stretch-induced doublet-potentiation in muscle where the effects of a stimulus are modified [51]. Briefly, stretch-induced doublet potentiation is the experimental observation that the muscle's force response to stretch sum up more than linearly when subjected to multiple back-to-back electrical spikes [26, 51]. By comparison, our construction of the interpolation variable $a(t)$ assume that the force responses adds up linearly and, in doing so, our approach implicitly serves as a control to test nonlinear summations of forces. Thus, in addition to revealing the rheological origins of muscle work loops, the splicing hypothesis may help identify circumstances when tissue-specific phenomena such as doublet-potentiation become functionally consequential.

The quality of the predictions point to the veracity of the splicing hypothesis and the rheological basis for the emergence of work loops in muscle. It also underscores the robustness of three linearity assumptions, namely, (**i**) linear rheology for the stimulated basis loop (ellipse-shaped), (**ii**) the principle of superposition to extract an interpolation variable between rheological states from the isometric twitch response, and (**iii**) the intermediate basis loops as a linear interpolation between the minimal

and maximal basis loops to accommodate the slowly varying rheological states. The robustness of the linear rheological assumption indicates that although muscle is a nonlinear material with non-elliptic basis loops, ellipses can adequately capture the dominant features of the basis loops. The robustness of a linear interpolation, *i.e.* equation (3.10), for constructing the transition between rheological states and using that the infer the behavior of a sub-maximally activated muscle is also to be expected based on proven antecedents in capturing neural stimulation dynamics in sensory systems [115] and studies on dynamic stiffness of ankle muscles [116]. Thus we conclude that the basis loops are the building blocks for the work loop in muscle, in agreement with the splicing hypothesis.

3.5.3 Muscle biophysical model

Although the rat and sculpin datasets provided two independent lines of validation based on measured work loops, the datasets were not specifically collected to test splicing and represent only two muscles out of a myriad of muscle types. So to further test splicing, we use direct numerical simulations of a detailed biophysical model of the contractile machinery in muscle [81]. The objectives are two-fold. Firstly, to present a work flow that guides design of future experiments in inferring the basis loops and interpreting measured work loops in terms of them. And secondly, to show that the splicing approach can adequately predict loop shape in current muscle models and therefore also show the applicability of splicing across multiple muscle types and not just of the muscles considered here.

The detailed biophysical model by Walcott captures the forces of single sarcomeres, contractile structures of approximately 2.5µm in length and which repeat in series to form a single muscle fibril. Skeletal muscles comprise of bundles of such fibrils. Within a single sarcomere, contraction is powered by myosin motors that interact with actin filaments by forming force-bearing crossbridges when myosin stochastically binds to

actin, strokes and unbinds (figure 3.5a). Walcott's model incorporates realistic aspects such as thin filament activation dynamics and spatial coupling between actomyosin crossbridges [119, 120] in addition to the latest advances in modelling the Lymn-Taylor actomyosin crossbridge cycle that underlies force production in muscle [14, 26].

We assess the splicing hypothesis in the sarcomere model by predicting work loops from basis loops using equation (3.10). The work loop $F(t)$ is obtained from the sarcomere model for a periodic stimulation protocol that varies between two values and the basis loops, $F_A(t)$ and $F_B(t)$ are obtained by holding the stimulus constant at each value. The stimulus used as the external control parameter is a coupling strength ε that modulates the spatial coupling between neighboring crossbridges [Methods 3.8.4, figure 3.5a], and the rheological state of the sarcomere model is the exact bond distribution [15] of these crossbridges that make up the sarcomere's viscoelastic resistance to mechanical perturbations. We implement a periodic back and forth switch, *i.e.* a rectangular pulse train, for the stimulation protocol in which the coupling strength ε switches between values corresponding to pCa = 6.17 and pCa= 7.04 [See Methods 3.8.4]. Such stimulation protocols are common when applying tetanic electrical stimuli [e.g. 98]. Much like the rat and sculpin datasets, the rheological state does not change instantaneously in response to the stimulus and has additional dynamics that must be accounted for. Although the rheological state is available in our implementation of Walcott's model in the form of bond distributions, it is generally not accessible in work loop experiments. So we adapt the approach used in the sculpin dataset and instead use the isometric response to the same stimulation protocol to construct a linear interpolation variable $a(t)$ as a proxy for the rheological state (see equation 3.10). Specifically, the isometric response is collected over several periods of the stimulation protocol and averaged at the same angular phase of a period from 0° to 360°., i.e. phased-averaged, and then normalized between zero and one to form the interpolation variable $a(t)$ at every time point in the period. This approach uses

only experimentally accessible elements and therefore the flow chart of figure 3.5b can be applied to muscle work loop experiments. The elements are namely the basis loops obtained by holding the stimulus constant, the isometric force response to a time-varying stimulation protocol, and work loops obtained for the same stimulation protocol.

We also probe the model's nonlinearities to demonstrate that splicing can work even for non-elliptic basis loops by using peak-to-peak oscillatory amplitudes that are twice the power stroke length of myosin. We repeat this for three different oscillation frequencies to elucidate the effect of slow versus fast transitions between rheological states relative to the oscillation time period (figure 3.5c). To separately identify the roles of basis loops and dynamics associated with switching between them, we show both the spliced loop and final predicted loop. The spliced loop assumes an instantaneous change in rheological states and the final predicted loop applies the interpolation variable estimated from isometric experiments (see equation 3.10 and panel titled transient dynamics in figure 3.5b). The predicted loops accurately reconstructs the work loop at all oscillation frequencies and the idealized spliced loop is shown to underlie the overall shape of the work loops. Not surprisingly, the sharp corners in the idealized splicing construction are smoothed out by incorporating the isometric force response which captures asymmetries in the timescales of force rise versus decay. If in muscle experiments, direct measurement of the basis loop could damage the tissue, we find that small amplitude measurements of basis loop could be used in lieu of the true large amplitude basis loop with little loss of accuracy, at least for this detailed biophysical model of muscle (figure 3.5 - Figure Supplement 1). Thus, work loops are comprised of two components: (**i**) an idealized spliced loop formed from basis loops that can be found from the rheological response at constant stimulus, and (**ii**) dynamics between transitioning between rheological states that smooth or regularize the idealized loop and can be found using isometric force

responses.

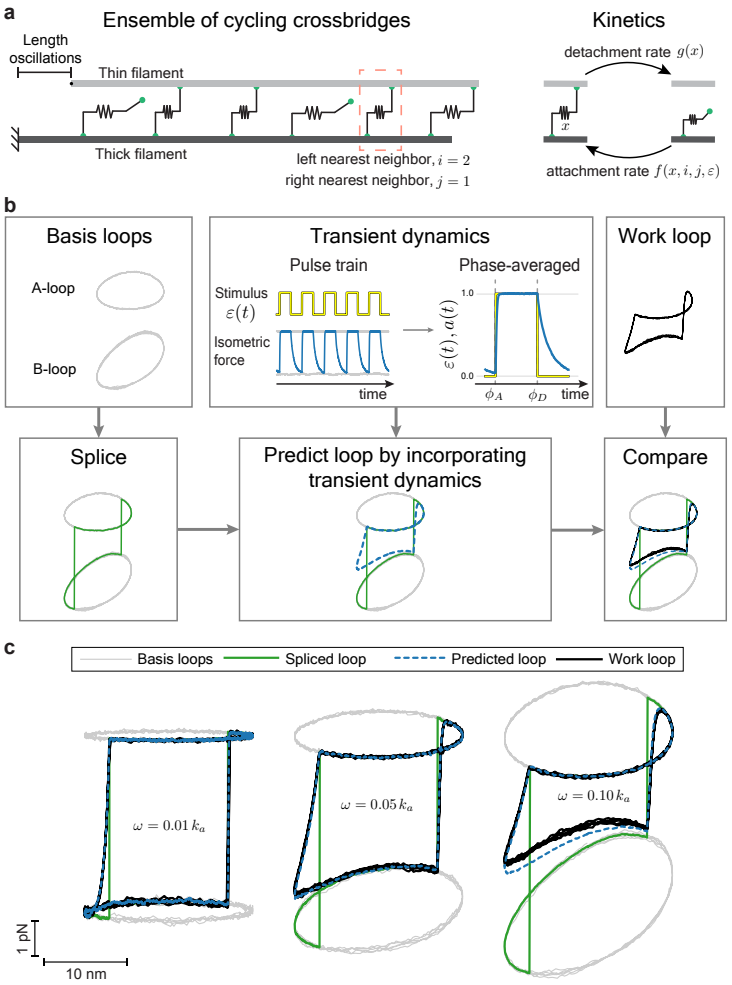

Figure 3.5: **Work loop prediction in muscle: a model-based validation of splicing. a,** The sarcomere is modeled as an ensemble of crossbridges that cycle between attached and detached states depending on its internal displacement x, distance to its left nearest neighbor i, distance to its right nearest neighbor j, and a coupling strength ε that is varied as the external control parameter and used as the stimulus [81, Methods 3.8.4]. Loops are generated using Monte Carlo simulations of an ensemble consisting of 500,000 crossbridges. **b,** Flow chart to predict work loops based on basis loops and isometric responses, and thus assess the splicing hypothesis. **c,** Outputs of the flow chart for three different frequencies placed next to each other for comparison. The basis loops and work loops are the direct results of Monte Carlo simulations whereas the spliced and predicted loop are computed using the splicing hypothesis. The frequency scale k_a is the myosin attachment rate taken to be around $40Hz$ in chicken pectoralis at 25°C [81]. The vertical scale is in units of tension per crossbridge whereas the horizontal scale is in units of sarcomere displacement.

3.6 Discussion

In examining the mathematical framework and evidence presented here, the reader is alerted to some cautionary points. Muscle is not monolithic and considerable physiological differences arise between different types of muscle; skeletal, cardiac, smooth, fast or slow, and many other varieties. This paper tests the splicing hypothesis in two specific muscles from rat and a short-horn sculpin for which the type of data needed are presently available, but future studies may expand that set. Furthermore, rheology is fundamentally a bulk property and only lends partial insight into the molecular mechanisms underlying it. So rheological studies are complementary to ongoing studies and debates that are centered around the molecular mechanisms behind intriguing muscle phenomena such as history-dependence [51, 99, 100], length-dependent transitions [121], and other transient non-steady phenomena [26, 122]. But, insofar as stable work loops can be measured and are applicable to mechanical actuations in animals, testing the splicing hypothesis will lend insight into the applicability of fixed-stimulus rheology to the functionally more realistic case of a time-varying stimulus. In this manner, the work presented here takes a bottom-up and data-driven approach to assess how well a superpositiong of fixed-stimulus rheology explains the data under time-varying stimulation. Furthermore, the splicing hypothesis presents a means to incorporate steady-state dynamical rheology into predictions under non-steady conditions so that future investigations can unambiguously account for the role of steady-state rheology before attributing measured responses to new phenomena.

While our focus is a rheological basis for skeletal muscle work loops, we predict that the splicing hypothesis will be applicable and bring new insights to other striated muscles based on our examination of a detailed sarcomere model and the fact that sarcomeres are constitutive elements of all striated muscles. Cardiac muscles are a key area of clinical relevance because their mechanical behavior is a central component of

heart function and dysfunction [5, 47]. Further validation in more specialized cardiac muscle models and in experiments are certainly necessary and may be guided by the flow chart of figure 3.5b. The basis loops are likely non-elliptic, as evidenced by rat papillary dataset [111] shown in figure 3.4a, and can be accounted for by introducing higher harmonic modes into the data analysis (see Methods 3.8.1). The basis loops themselves may also be difficult to directly measure without inducing tissue damage, but can be inferred in an approach similar to the sculpin dataset analysis by pooling together multiple work loops that differ only in stimuli timing (see Methods 3.8.3). Keeping all these possible complexities in mind, the splicing hypothesis may provide a new phenomenological approach to modelling the rheological behavior of cardiac muscle in a manner that accounts for its tunability.

3.7 Conclusion

We adapted current oscillatory rheological methods to admit tunable properties by splicing fixed-stimulus rheologies and showed its predictive ability using published data on sculpin skeletal muscle and direct numerical simulations of a detailed sarcomere model. We found that most but not all of the sculpin muscle's work loop is accounted for by an interpolation between basis loops and rheological states. Our method incorporates experimental rheological characterization of muscle into predictions under time-varying neural or electrical stimuli, so that future investigations into new emergent muscle phenomena can account for and filter the effects of steady-state rheology. In this manner, the splicing hypothesis is a new tool to study muscle mechanics and complements ongoing investigations into the molecular mechanisms that underlie the emergent rheological properties. Finally, the shape-space of work loops provides a unified view of the vastly different loop shapes a muscle can exhibit to variably perform as motors, springs, dampers, and combinations thereof based on its

tunable rheology.

Acknowledgments: Funding support from the Raymond and Beverly Sackler Institute for Biological, Physical and Engineering Sciences at Yale, a National Institutes of Health training grant T32EB019941, and the Robert E. Apfel Fellowship awarded by Yale. This material is based upon work supported by the National Science Foundation under Grant No. 1830870. M.M. Bandi, S. Mandre, and M. Murrell for helpful comments.
Author Contributions: K.D.N. and M.V. conceived the research, designed the research, analyzed and interpreted the results, and wrote the paper.
Competing interests: The authors declare no competing interests.

3.8 Methods

3.8.1 Expansion with higher harmonics:

The generalization of splicing the fixed-stimulus basis loops to include higher harmonics is a straightforward extension of splicing ellipses by using a Fourier series for the force response. The force response to sinusoidal length perturbations as given by equation (3.2) generalizes to

$$F(t) = \begin{cases} F_{A0} + \Delta L \sum_k (E'_{A,k} \sin(k\omega t) + E''_{A,k} \cos(k\omega t)), & \text{for } \omega t \in [\phi_A, \phi_B] \\ F_{B0} + \Delta L \sum_k (E'_{B,k} \sin(k\omega t) + E''_{B,k} \cos(k\omega t)), & \text{otherwise} \end{cases} \tag{3.12}$$

for index k over the set of positive integers and where each higher harmonic introduces four additional moduli. Subtracting the state B force response and normalizing by length scale ΔL and force scale $F_{A0} - F_{B0}$ result in two difference of moduli of the k^{th} harmonic: $\Delta e'_k = \Delta L(E'_{A,k} - E'_{B,k})/(F_{A0} - F_{B0})$ and $\Delta e''_k = \Delta L(E''_{A,k} - E''_{B,k})/(F_{A0} - F_{B0})$. Expanding equations (3.4)–(3.7) to include the higher harmonics results in

$$f(\phi) = \begin{cases} 1 + \sum_k \left(\frac{w'_k}{w_0} \frac{l_B - l_A}{\alpha_k} \sin k\phi + \frac{w''_k}{w_0} \frac{l_B - l_A}{\beta_k} \cos k\phi \right), & \text{for } \phi \in [\phi_A, \phi_B] \\ 0, & \text{otherwise.} \end{cases} \tag{3.13}$$

$$w'_k = -\Delta e'_k \int_{\phi_A}^{\phi_B} \sin k\phi \cos\phi \, d\phi = -\Delta e'_k \alpha_k \tag{3.14}$$

$$w''_k = -\Delta e''_k \int_{\phi_A}^{\phi_B} \cos k\phi \cos\phi \, d\phi = -\Delta e''_k \beta_k \tag{3.15}$$

$$w_0 = -\int_{\ell_A}^{\ell_D} d\ell = \ell_A - \ell_B, \tag{3.16}$$

where $\alpha_k = \int_{\phi_A}^{\phi_B} \sin k\phi \cos\phi \, d\phi$ and $\beta_k = \int_{\phi_A}^{\phi_B} \cos k\phi \cos\phi \, d\phi$ are shape parameters. The terms w'_k and w''_k are the work by storage forces and loss forces of the k^{th} harmonic, respectively. The net work now includes contributes from all higher harmonics as

$$w_n = w_0 + \sum_k (w'_k + w''_k). \tag{3.17}$$

The relation between nondimensional net work w_n and the dimensional net work remains unchanged according to equation (3.9) because only the first harmonic of the state B force response contributes to net work.

3.8.2 Traversing the shape space

We document here the process of generating dimensionless spliced loops illustrated in figure 3.3c for a tunable Maxwell body in parallel with an ideal force generator. The force response to an oscillatory motion of unit amplitude is given by equations (3.4-3.7) with $\phi_A = \pi/6$ and $\phi_B = 7\pi/6$. The $\Delta e'$ and $\Delta e''$ needed to calculate w' and w'' are derived for a Maxwell body, a spring with unit stiffness in series with a dashpot with unit damping coefficient. Specifically, $\Delta e' = \omega^2/(\omega^2+1)$ and $\Delta e'' = \omega/(\omega^2+1)$. The oscillatory frequencies ω are chosen such the spliced loops are uniformly spread on the semicircle on the Nyquist plot. Lastly, we hold the ideal motor work constant at $w_0 = 1.5$.

3.8.3 Sculpin Work Loops

We estimated F_{A0}, E'_A, and E''_A in equation (3.11) from the set of 12 work loops of a short-horned sculpin abdominal muscle published by Johnson and Johnston [113]. All optimization and root-finding are performed using the Python `scipy.optimize` library [90]. The data were extracted by digitizing the original figures.

The interpolation variable $a(t)$ is found using published isometric twitch response

of the same muscle, but separately measured by Altringham and Johnston [114] at a temperature between 2.5°C and 3.5°C. The work loop data were measured at 4°C. A smooth approximation $ct^k \exp(-t/\tau_a)$ is fitted to the twitch response, which captures the fast initial rise and slower decay in the measurements. When the twitch response is scaled to be between 0 and 1 where 1 is equal to the peak tension measured, we find these values to be $c = 3.39 \cdot 10^{-4}$, $k = 2.99$, and $\tau_a = 13.2$ms. To simulate the response to three electrical stimuli instead of one, we perform the following procedure: **1.** Superimpose the three twitch responses separated by 20ms intervals. **2.** Scale the superimposed response by its maximum so that interpolation is normalized to be between 0 and 1. We refer to this intermediate step as $a^*(t)$. **3.** Impose periodicity by finding a baseline shift δ such that $a^*(\delta) = a^*(T + \delta)$ where $T = 200$ms is the period of the sculpin work loops and define the desired output $a(t)$ to be $a^*(t+\delta)$. The third step makes a minor correction to ensure that $a(t)$ is periodic and is necessary because the smooth fit to the data $ct^k \exp(-t/\tau_a)$ is not automatically periodic. This is because, under steady periodic conditions, the value at $t = 0$ is not zero. So we use the initial time offset $\delta = 3.21$ms, which captures a non-zero initial condition of $a(0) = a(T) = 0.00356$. The final result $a(t)$ is plotted in as an inset in figure 3.4c.

Given $a(t)$, measured force response $y_i(t)$, and stimulus timing θ_i of the i^{th} sculpin work loop, a set of values (F_{A0}, E'_A, E''_A) were generated for the i^{th} loop by excluding it and minimizing the error for the remaining loops. So the fitted values for the i^{th} loop are obtained by minimizing

$$\sum_{m \neq i} \sum_{k} \left[a(t_k - \theta_m)(F_{A0} + \Delta L E'_A \sin(\omega t_k) + \Delta L E''_A \cos(\omega t_k)) - y_m(t_k) \right]^2 \qquad (3.18)$$

where k indexes the time steps in $[0, T]$.

Goodness of fit measures

Pearson's correlation coefficient for the i^{th} loop is calculated from the fitted values as

$$r = \frac{\sum_k (y_i(t_k) - \bar{y_i})(F(t_k) - \bar{F})}{\sum_k (y_i(t_k) - \bar{y_i}) \sum_k (F(t_k) - \bar{F})} \tag{3.19}$$

where bars denote mean values and $F(t_k)$ is predicted force response in equation (3.11) given the fitted values (F_{A0}, E'_A, E''_A). We use Pearson's correlation coefficient because of the well-known problems in assessing goodness of fit using the coefficient of determination R^2 that is employed for linear statistical models [123].

3.8.4 Sarcomere model simulation

We use a published crossbridge model to assess the applicability of splicing [81]. The attachment rate f of a crossbridge to an internal displacement in the interval $[x, x+dx]$ is given by

$$f(x, i, j, \varepsilon) = \beta(i, j, \varepsilon) \sqrt{\frac{D}{2\pi}} \exp\left(-\frac{D}{2} x^2\right) \tag{3.20}$$

where $D = 100$. The function $\beta(i, j, \varepsilon)$ depends on coupling strength ε and the distance to the nearest attached crossbridge on the left i and right j as

$$\beta(i, j, \varepsilon) = \begin{cases} 1 & \text{if} \quad i + j \leq C \\ \varepsilon^{(i+j-C)/C} & \text{if} \quad i, j < C \& i + j > C \\ \varepsilon^{i/C} & \text{if} \quad i < C \& j \geq C \\ \varepsilon^{j/C} & \text{if} \quad i \geq C \& j < C \\ \varepsilon & \text{if} \quad i \geq C \& j \geq C \end{cases} \tag{3.21}$$

where $C = 11$. The detachment rate g of a crossbridge with internal displacement x is

$$g(x) = \frac{1}{K} \exp(-E(x+1)) \tag{3.22}$$

where $E = 1$ and $K = 0.2$.

A Monte Carlo simulation computed the behavior of 500,000 crossbridges as the system is sheared by an oscillatory motion $L(t) = A\sin(\omega t)$ with $A = 1$ and a coupling strength ε that periodically alternates between 0.15 and $\exp(-5)$, which respectively corresponds to pCa values of 6.17 and 7.04 [81, via Walcott's equation 23]. At each timestep, crossbridge attachment and detachment are decided by a random number generator. The tension T_m per crossbridge transmitted across the system at the m^{th} timestep is computed as

$$T_m = \frac{1}{N} \sum_{n=1}^{N} (x_n + 1)s \tag{3.23}$$

for index n over N crossbridges and where $s = 1$ if a crossbridge is attached and zero if detached.

All equations are nondimensional. The chosen timescale is $1/k_a$ where $k_a = 40$Hz is the attachment rate of a crossbridge with many attached neighbors. The length scale is a powerstroke distance $d = 10$nm. The stiffness scale is $k = 0.4$pN/nm, the stiffness of each crossbridge's elastic spring. Consequently, the tension scale is $kd = 4$pN in units of force per crossbridge. The Monte Carlo simulations were performed using Matlab version 9.8.0.1323502 (R2020a, Natick, MA).

3.8.5 Illustrative phenomenological muscle model

We use a previously published phenomenological muscle model [48] to illustrate the splicing between nonlinear rheologies shown in figure 3.2 - Figure Supplement 1a. The force output $F(a, l, v)$ is a function of activation a, length l and velocity v according

to,

$$F(a,l,v) = B(a,l)F_L(l)F_V(l,v) + F_{P1}(l) + BF_{P2}(l), \tag{3.24}$$

where the functions are defined as,

$$B(a,l) = 1 - \exp\left(\left(-\frac{a}{0.56N_f(l)}\right)^{N_f(l)}\right), \tag{3.25}$$

$$N_f(l) = 2.11 + 4.16(l^{-1} - 1), \tag{3.26}$$

$$F_L(l) = \exp\left(-\left|\frac{l^{1.93} - 1}{1.03}\right|^{1.87}\right), \tag{3.27}$$

$$F_V(l,v) = \begin{cases} \frac{-5.72-v}{-5.72+(1.38+2.09l)v}, & v \leq 0 \\ \frac{0.62-(-3.12+4.21l-2.67l^2)v}{0.62+v}, & v > 0 \end{cases} \tag{3.28}$$

$$F_{P1}(l) = 5.42\ln\left(\exp\left(\frac{l-1.42}{0.052}\right) + 1\right), \tag{3.29}$$

$$F_{P2}(l) = -0.02\exp(-18.7(l-0.79) - 1). \tag{3.30}$$

To generate the nonlinear force responses, $a = 1$ is used as the first activation state and $a = 0.5$ as the second. The dimensional length input is $l(t) = 1+0.15\sin((3\pi/2)t)$, activation phase is $\phi_A = \sin^{-1}(0.5)$, and deactivation phase is $\phi_D = (\sin^{-1}(0.4) + \pi)$. All simulations were performed using Matlab version 9.8.0.1323502 (R2020a, Natick, MA).

List of source files

Source code: Matlab code used to generate the sarcomere model described in Methods 3.8.4 and used in figure 3.5.

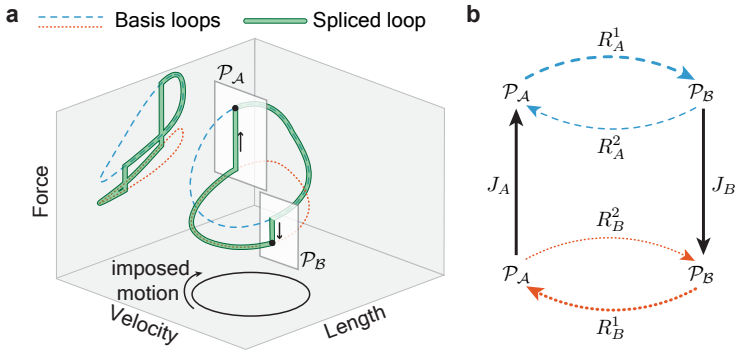

Figure 3.2 - Figure Supplement 1: The spliced loop can be viewed as a singular periodic orbit of a piecewise smooth dynamical system with two switching planes $\mathcal{P}_\mathcal{B}$ and $\mathcal{P}_\mathcal{A}$ that are defined by the phases ϕ_B and ϕ_A when the rheological state is changed from A to B or *vice versa*. At rheological states B or A, the dynamics of the material when subjected to periodic length oscillations are governed by the composite functions $(R_B^1 \circ R_B^2)$ and $(R_A^2 \circ R_A^1)$, respectively, which map initial conditions on the plane $\mathcal{P}_A$ to the plane $\mathcal{P}_B$ and back onto $\mathcal{P}_A$ again. The oscillatory responses at states, B or A, correspond to stable periodic orbits of the two dynamical systems. The existence of the orbit implies that a steady response can be measured under a constant rheological state. The splicing of those two periodic orbits by instantaneously switching between them at the planes $\mathcal{P}_\mathcal{B}$ and $\mathcal{P}_\mathcal{A}$ yields a new periodic orbit for the spliced dynamical system $(J_D \circ R_A^1 \circ J_A \circ R_B^1)$. The instantaneous jumps J_A and J_B between slowly varying trajectories resembles approaches from geometric singular perturbation theory for constructing relaxation oscillations in multiple-timescale systems [124, 125]. A nonlinear muscle model [Methods 3.8.5, 48] in which force depends on activation, length, and velocity was used to illustrate the basis loops.

Table Figure 3.4 - Table Supplement 1: Fitted ellipses to the sculpin work loop data [113]. The scale $F_{\max}$ is the difference between the maximal and minimal force in the 5° work loop

Stimulus timing	$F_{A,0}/F_{\max}$	$\Delta LE'_A/F_{A,0}$	$\Delta LE''_A/F_{A,0}$
5°	0.659	0.186	0.333
30°	0.678	0.231	0.300
60°	0.695	0.235	0.245
90°	0.701	0.217	0.226
120°	0.702	0.202	0.230
150°	0.692	0.221	0.248
180°	0.690	0.223	0.250
210°	0.685	0.224	0.245
245°	0.694	0.202	0.266
280°	0.677	0.209	0.236
320°	0.708	0.262	0.245
345°	0.708	0.254	0.238

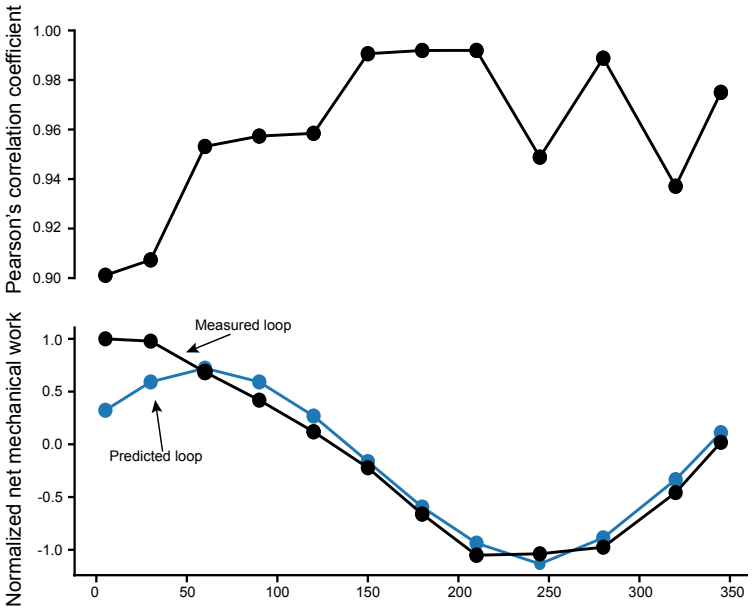

Figure 3.4 - Figure Supplement 1: Quantitative comparisons between measured sculpin work loops and loops predicted from splicing hypothesis. (Top) The Pearson's correlation is calculated for each pair of measured and predicted loop as a function of the stimuli timing in units of degrees from 0° to 360°. See Methods 3.8.3 for details of the calculation. (Bottom) The net mechanical work is calculated for both the measured and predict loops by taking the total enclosed area of each loop. The values are normalized by the net work performed by the measured 5° loop.

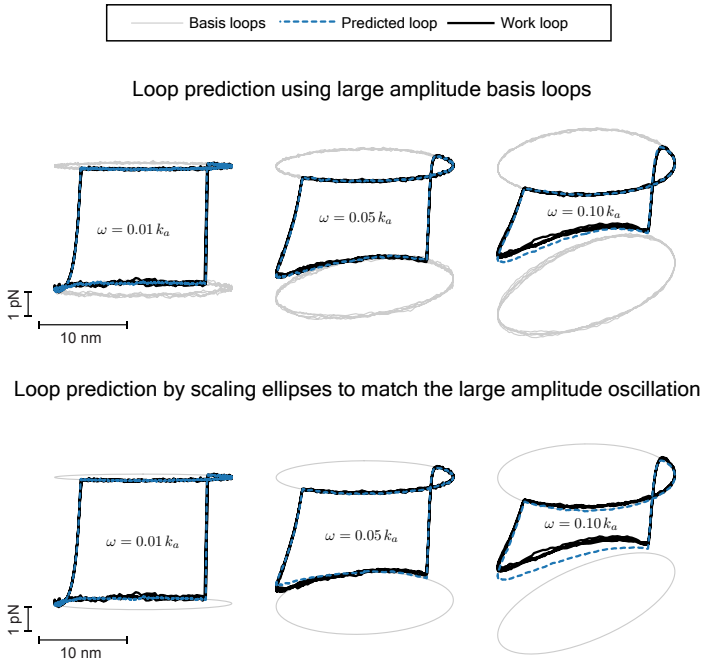

Figure 3.5 - Figure Supplement 1: Illustration of how small-amplitude basis loops can be used to generate large-amplitude work loop predictions. When large amplitude basis loops are inaccessible to direct measurement, scaling up linear ellipses found from small amplitude oscillations results in minimal loss of accuracy between predicted loops and work loops for the sarcomere model. The work loops (solid black lines) are the same in both panels and serve as a reference for comparison of predicted loops. All loops are generated from Monte Carlo simulations of 500,000 crossbridges following the flow chart of the main figure.

Chapter 4

The role of filament compliance in sarcomeric viscoelasticity

4.1 Abstract

Striated muscles are active viscoelastic materials that can function as either an elastic solid-like structure or a viscous fluid-like damper depending on time-durations of interest and neural inputs. Both are important to the biomechanical functions that muscles provide to animal bodies and ultimately arise from the mechanochemical dynamics of molecular actomyosin crossbridges that cycle on a thick and thin filament lattice. A central premise of current muscle models based on half-sarcomeres is that crossbridges attach and detach independently of each other. This independence is satisfied under length perturbation experiments if the filament lattice is rigid, and in such a case, the half-sarcomere's viscoelastic rheology is determined solely by the transient nature of crossbridges. In this paper, we show that allowing for a compliant filament lattice leads to a sarcomeric viscoelasticity that is distinct from the dynamics of the constituent crossbridges. The physical basis lies in mechanical interactions between crossbridges via elastic deformations of the filaments, which rigid filaments do not allow for. We show that a dimensionless ratio between filament overlap length L and a length scale ℓ quantifies the mechanical interactions. The length scale ℓ arises

from a partitioning of strains between crossbridges and filaments. It is the distance over which elastic displacements of the filaments become appreciable and the strains that crossbridges are subjected to become uncorrelated with each other. The half-sarcomere is rigid if $L/\ell \ll 1$ and compliant if it is at least comparable to unity. Using conservative estimates for half-sarcomere parameters, we find that $L/\ell \approx 10$ for an activated rabbit psoas muscles and similar values for other striated muscles from different animals. This suggests that the additional dynamics introduced by filament compliance may play a dominant role on sarcomeric viscoelasticity and ought to be considered in muscle models based on half-sarcomeres.

4.2 Introduction

Striated muscles are active biological materials that exert forces depending on neural inputs and in resistance to external length perturbations [7, 16, 26]. Like many soft materials, the resistive forces are nearly proportional to the magnitude of the length perturbations on fast timescales, which then relax on longer timescales due to internal dissipative processes [15, 16]. The proportional response characterizes a muscle's elastic solid-like nature whereas the relaxation characterizes its viscous fluid-like nature. Both are important to the biomechanical functions that muscles provide, for example, as elastic springs to maintain body postures [8, 11] or as viscous dashpots to dissipate excessive kinetic energy [13, 49]. Taken together, they form the viscoelastic material rheology of a muscle.

There are passive and active components to a muscle's viscoelasticity. The passive components consist of tissues, fluids, and tendons that are all relatively unchanging on timescales that muscles operate on [13, 45]. On the other hand, the active components are amenable to changes based on neural inputs and biomechanical needs [1, 7]. They are driven by the mechanochemical dynamics of molecular motors known as

crossbridges that collectively operate on a crystalline lattice made of interdigitating thick myosin filaments and thin actin filaments [14, 59, 126]. A large class of muscle models is based on the half-sarcomere that itself is modeled by the crossbridge and filament lattice system [59, 71–73]. A central premise of these muscle models is that crossbridges are independent of each other, which is satisfied under external length perturbations when the lattice is rigid. A simplification that crossbridge independence affords is that the mechanics of the half-sarcomere are determined entirely by the average crossbridge. Additionally, the independence also predicts that a muscle's active forces, elastic stiffness, and viscous damping are all linearly dependent on each other because of a common proportionality to the number of participating crossbridges [15, 59]. The premise of a rigid filament lattice thus underpins the connection between the mechanochemical dynamics of crossbridges with measured muscle forces.

However, direct measurements of actin filaments and x-ray diffraction studies estimate that roughly 50% of a sarcomere's compliance is due to the filaments alone [127–129]. This suggests that elastic deformations of the filament lattice may affect the mapping from crossbridges to muscles in ways not captured by models with rigid filaments and independent crossbridges [130]. In particular, the dynamics of a muscle's forces may be partially decoupled from the dynamics of individual crossbridges because of the intermediary filaments. The filaments can affect crossbridges in one of two ways, either as a lumped compliant element mechanically in series to all crossbridges or as many smaller compliant elements situated between neighboring crossbridges. The first way with a lumped compliance acts on the entire ensemble of crossbridges as a whole. The second way with smaller elements, on the other hand, acts on each crossbridge separately and provides a mechanism for interactions between crossbridges that, in principle, allows the half-sarcomere to take on temporal characteristics that crossbridges alone cannot. Both ways likely come into play and have been considered in the context of isometric force transients observed upon the

onset or removal of activation [82, 131, 132]. But similar considerations in the context of a half-sarcomere's viscoelasticity are sparse in comparison [83, 133]. The effects of a compliant filament lattice on a muscle's or a half-sarcomere's response to length perturbations thus remain poorly understood.

In this chapter, we relax the assumption that the filament lattice is rigid along the longitudinal axis of a half-sarcomere and model it as a compliant structure pulled on by cycling crossbridges. We take a mathematical approach similar to those of Mijailovich et al., 1996 [82] and White and Thorson, 1973 [134] to directly calculate the linear viscoelastic rheology of a one-dimensional half-sarcomere model with compliant filaments. We show that the compliance introduces mechanical interactions between crossbridges of the same filament via elastic stretching of the filament. These interactions give rise to a nondimensional parameter between the length L of a half-sarcomere and a strain-correlation length scale ℓ. Such interactions are reminiscent of a chemical cooperativity between crossbridges in which the attachment of one crossbridge partially opens the binding site of its neighboring crossbridges [135]. Furthermore, a compliance along the radial axis evidenced by sub-nanometer changes of lattice spacing may also lead to mechanical interactions between crossbridges of different filaments [37, 133, 136]. This chapter shows the emergent dynamics for one mode of crossbridge cooperativity via filament stretching, but other modes of cooperativity are possible and may lead to similar emergent dynamics that assuming independent crossbridges cannot capture.

4.3 Mathematical preliminaries

4.3.1 Linear viscoelastic rheology

The viscoelastic rheology of any material or structure is the experimental characterization of its response to length perturbations. We shall focus here on the response

to small perturbations, or the linear regime, to mirror experimental measurements of muscle viscoelasticity using sinusoidal analysis [41]. For simple structures, constant quantities such as stiffness and damping coefficients suffice to relate the input length perturbations to output force responses. But for more complicated structures, the input-to-output relation will not be constant and vary depending on the frequency content of the input length perturbation. For such structures, tools of linear dynamical systems help to formulate the input-to-output relation. Namely, the Laplace transformation that decomposes time-varying functions into exponential modes [68]. If $z(t)$ is the input length perturbation that varies with time t then its Laplace transform is denoted with a hat as $\hat{z}(s)$ that varies with the complex-valued Laplace variable s. Similarly, the output force response $T(t)$ transforms to $\hat{T}(s)$. The ratio $\hat{T}(s)/\hat{z}(s)$ is the mechanical impedance [4], which generalizes notions of springs and dashpots to linear viscoelastic materials that can exhibit elastic and viscous behaviors depending on experimental timescales. Deriving a structure's mechanical impedance is a complete characterization of its linear viscoelastic rheology.

4.3.2 Hooke's law for filaments

To incorporate filament compliance, the thick and thin filaments within the half-sarcomere are idealized as elastic structures subjected to stretch and compression. Consider a single thin filament that undergoes elastic displacements due to the dynamics of crossbridges. It has a cross-sectional area A_a, elastic modulus E_a, stress $\sigma_a(x,t)$, and displacement $u_a(x,t)$ as functions of the longitudinal coordinate x along its axis and time t. Hooke's law states that stress is proportional to strain $\partial u_a(x,t)/\partial x$ as

$$\sigma_a(x,t) = E\frac{\partial u_a}{\partial x}(x,t). \tag{4.1}$$

Following convention in muscle literature [82, 134], stress is expressed as a tension in units of force. The tension $T_a(x,t)$ along the filament would be the product $A_a\sigma_a(x,t)$ and given in terms of displacement as

$$T_a(x,t) = K_a \frac{\partial u_a}{\partial x}(x,t) \tag{4.2}$$

$$\text{where} \quad K_a = A_a E_a \tag{4.3}$$

is the thin filament stiffness in physical units of force per unit strain. The equations for thick filament tension and displacements are similarly obtained.

4.4 Compliant two-filament model of half-sarcomeres

We present a minimal modification of current half-sarcomere models to analyze the role of filament compliance. Like prior models [82, 83, 134], we condense the filament lattice into a two-filament system consisting of one actin filament and one myosin filament. This is in effect an averaging of the lattice's cross-sectional area down to a one-dimensional system. The two filaments transmit tension across the half-sarcomere due to crossbridge-induced tractions that themselves act in response to an externally imposed length perturbation. We shall apply the constitutive equations as follows below to derive the linear viscoelasticity of the compliant half-sarcomere model (see figure 4.1).

Let the displacements in the thin actin filament be denoted by $u_a(x,t)$ as a function of the longitudinal coordinate x and time t. The displacements in the thick myosin filament is similarly denoted by $u_m(x,t)$. The tensions in the actin filament $T_a(x,t)$ and the myosin filament $T_m(x,t)$ relate to the displacements according to Hooke's

law as

$$T_a(x,t) = K_a \frac{\partial u_a}{\partial x}(x,t) \tag{4.4}$$

$$\text{and} \quad T_m(x,t) = K_m \frac{\partial u_m}{\partial x}(x,t) \tag{4.5}$$

where K_a and K_m are the actin and myosin filaments' elastic moduli multiplied by their respective cross-sectional areas. A second constitutive equation relates the variation of filament tension to the traction $F(x,t)$ induced by crossbridge interactions between the two filaments, namely

$$\frac{\partial T_a}{\partial x}(x,t) = F(x,t) \tag{4.6}$$

$$\text{and} \quad \frac{\partial T_m}{\partial x}(x,t) = -F(x,t). \tag{4.7}$$

The tractions are forces distributed over a line element and take on dimensions of force per unit length. Since the two filaments are pulled on by equal and opposing tractions at every x, the sum of filament tensions is constant along x and necessarily equal to the total tension $T(t)$ transmitted across the two-filament system, *i.e.*

$$T(t) = T_a(x,t) + T_m(x,t). \tag{4.8}$$

And lastly, the boundary conditions (bcs) are given at $x = 0$ and $x = L$ where L is the overlap between the two filaments. At $x = 0$, the myosin filament is fixed in place while the actin filament is free. On the opposite boundary at $x = L$, the myosin filament is free while the actin filament is fixed to a plate that moves according to an external length perturbation $z(t)$. The fixed and free conditions stated in terms of

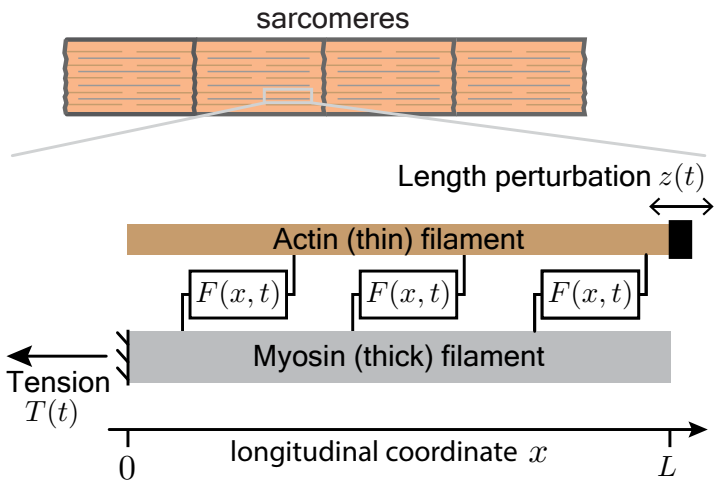

Figure 4.1: The compliant two-filament model of a half-sarcomere

displacements and tensions are

$$\text{bcs at } x = 0: \quad \begin{cases} u_m(x,t) = 0 \\ T_m(x,t) = T(t) \\ T_a(x,t) = 0 \end{cases} \tag{4.9}$$

and

$$\text{bcs at } x = L: \quad \begin{cases} u_a(x,t) = z(t) \\ T_m(x,t) = 0 \\ T_a(x,t) = T(t). \end{cases} \tag{4.10}$$

These equations are the governing equations of the compliant half-sarcomere model and we shall solve them for different choices of crossbridge traction to study the role of thick and thin filament compliance.

4.5 Results

4.5.1 Modeling crossbridge interactions

The interplay between crossbridge tractions and filament compliances is the focus of the half-sarcomere model. To capture it, we model crossbridge dynamics at every x with an ensemble of independently cycling crossbridges and allow ensembles at different x to interact via elastic displacements of the filaments. We further model the spatial distribution of crossbridges as uniformly spread along the filaments so that any differences are due to filament displacements alone. Prior work has shown that the tractions arising from multiple ensemble models of independent crossbridges are a sum of a steady active component and a time-varying viscoelastic resistance to external perturbations [Chapter 2]. We shall consider here the interplay of each component with filament compliance separately.

The steady active component of crossbridge tractions corresponds to the isometric tension measured for a muscle held at a fixed length. It is an ideal force distributed over a line element where ideal, by definition, means zero mechanical impedance or an invariance to elastic displacements of the filaments. Because of this property, the contributions of the steady active component to total tension transmitted is expected to be unaffected by filament compliances. To see this, we express the traction $F(x,t)$ induced by a constant ideal force per crossbridge f_{ideal} as

$$F = M f_{\text{ideal}} \tag{4.11}$$

where M is the density of crossbridge in units of number of crossbridges per length. The filament displacements and tensions of equations (4.6 - 4.10) can be solved di-

rectly without reference to the elastic displacements of the filaments as

$$T_{ideal} = MLf_{\text{ideal}}, \tag{4.12}$$

$$T_{a,\text{ideal}}(x) = T_{\text{ideal}}\left(\frac{x}{L}\right), \tag{4.13}$$

$$\text{and} \quad T_{m,\text{ideal}}(x) = T_{\text{ideal}}\left(1 - \frac{x}{L}\right) \tag{4.14}$$

in which a subscript is added to denote the solution to ideal crossbridge tractions. The tension transmitted across the system is simply the ideal force per crossbridge f_{ideal} multiplied by the number of crossbridges ML. The filament tensions $T_{a,\text{ideal}}(x)$ and $T_{m,\text{ideal}}(x)$ are simply linearly interpolations between zero and the total tension. Filament compliances K_a and K_m do not appear and therefore bear no influences on the tension transmitted across the half-sarcomere model.

The viscoelastic component of crossbridge tractions, on the other hand, have a nonzero mechanical impedance and therefore must vary in response to elastic displacements of the filaments induced by the external length perturbation $z(t)$ applied at the boundaries. These tractions are shown to be sums of exponential processes for multiple ensemble models of crossbridge dynamics, each of which is mechanically analogous to a spring and dashpot in series [Chapter 2]. So we model the viscoelastic forces as a single exponential process and examine its interplay with filament compliances. Specifically, the traction $F(x,t)$ arising from crossbridge dynamics is modeled by a first-order in time differential equation

$$\frac{\partial F(x,t)}{\partial t} + \frac{1}{\tau}F(x,t) = M\lambda\frac{\partial}{\partial t}\left(u_a(x,t) - u_m(x,t)\right) \tag{4.15}$$

where λ is the magnitude of the exponential process with units of stiffness [force/length] and is multiplied by crossbridge density M, τ is the exponential time-constant, and the difference in filament displacements, $u_a(x,t) - u_m(x,t)$, is the amount by which

crossbridges at x are stretched. For algebraic convenience of manipulating differential equations, the time-varying functions are Laplace-transformed into

$$\hat{F}(x,s) = M\lambda\hat{h}(s)\left(\hat{u}_a(x,s) - \hat{u}_m(x,s)\right) \tag{4.16}$$

$$\text{where } \hat{h}(s) = \frac{s}{s+1/\tau} \tag{4.17}$$

where time t is exchanged for the Laplace variable s, a hat notation denotes transformed functions, and $\hat{h}(s)$ is the transfer function of an exponential process of unit magnitude and time-constant τ. Solving the Laplace-transformed versions of the constitutive equations (4.4 - 4.10) yields the mechanical impedance of the compliance half-sarcomere model, the ratio between total tension $\hat{T}(s)$ and the length perturbation $\hat{z}(s)$, as

$$\frac{\hat{T}(s)}{\hat{z}(s)} = \left(\frac{K_a + K_m}{L}\right) \frac{\left(\frac{L}{\ell}\sqrt{\hat{h}}\right)\sinh\left(\frac{L}{\ell}\sqrt{\hat{h}}\right)}{2 + \left(\frac{K_m}{K_a} + \frac{K_a}{K_m}\right)\cosh\left(\frac{L}{\ell}\sqrt{\hat{h}}\right) + \left(\frac{L}{\ell}\sqrt{\hat{h}}\right)\sinh\left(\frac{L}{\ell}\sqrt{\hat{h}}\right)} \tag{4.18}$$

in terms of a length scale

$$\ell = \sqrt{\frac{\left(\frac{1}{K_a} + \frac{1}{K_m}\right)^{-1}}{M\lambda}}. \tag{4.19}$$

The length scale ℓ arises from a competition between filament compliance and the viscoelasticity of crossbridge ensembles, and algebraically obtained from the ratio of filament stiffnesses added in series and the crossbridge stiffness distributed over a line element. It is the length scale over which elastic displacements and strains of the filaments spatially vary. Strains at two points along the filaments separated a distance less than ℓ are strongly correlated with each other because the filaments are rigid. If separated a distance greater than ℓ, however, the two strains are uncorrelated and it is not possible to *a priori* predict one from the other without knowledge of the boundary conditions. This strain-correlation alters crossbridge dynamics in the following way. Two crossbridges separated by a distance less than ℓ are subject to

the same strain and therefore experience the same strain-dependent attachment and detachment rates. This is the case of rigid filaments models in which the size scale of the half-sarcomere L is much less than ℓ and all crossbridges cycle according to their own dynamics with no dependence on any other crossbridge. But if two crossbridges are separated by a distance greater than ℓ, they are subject to uncorrelated filament strains and experience different strain-dependent attachment and detachment rates. Thus, for half-sarcomeres with size L longer than ℓ, filament compliance lead to emergent spatial inhomogeneities in filament strains acting on length scale l that give rise to different sub-populations of crossbridges within the whole ensemble.

The assumption of rigid filaments in half-sarcomeres is equivalent to the overlap L of the filaments being much smaller than the length scale ℓ. In this case, the impedance of eqn. (4.18) simplifies to $ML\lambda\hat{h}(s)$, which is the exponential process multiplied by the total number of crossbridges. At the opposite extreme, when L is much larger than ℓ, the filaments are overly compliant and unable to support crossbridge forces. The impedance here simplifies to the sum of filament stiffnesses $(K_a + K_m)/L$. It is when L is comparable to ℓ that both crossbridge dynamics and filament compliance and must be taken into consideration.

4.5.2 Dynamics of the compliant half-sarcomere model

Compliant filaments affect the tractions of crossbridge ensembles depending on the ratio L/ℓ and give rise to a total tension whose temporal characteristics determine the viscoelasticity of the half-sarcomere model. To examine the emergent half-sarcomere viscoelasticity, consider the dynamic stiffness which measures the viscoelastic response to sinusoidal length perturbations of frequency ω [41]. The dynamic stiffness $H(\omega)$ is defined as the magnitude of the complex-value impedance $\hat{T}(s)/\hat{z}(s)$ of Eqn.(4.18)

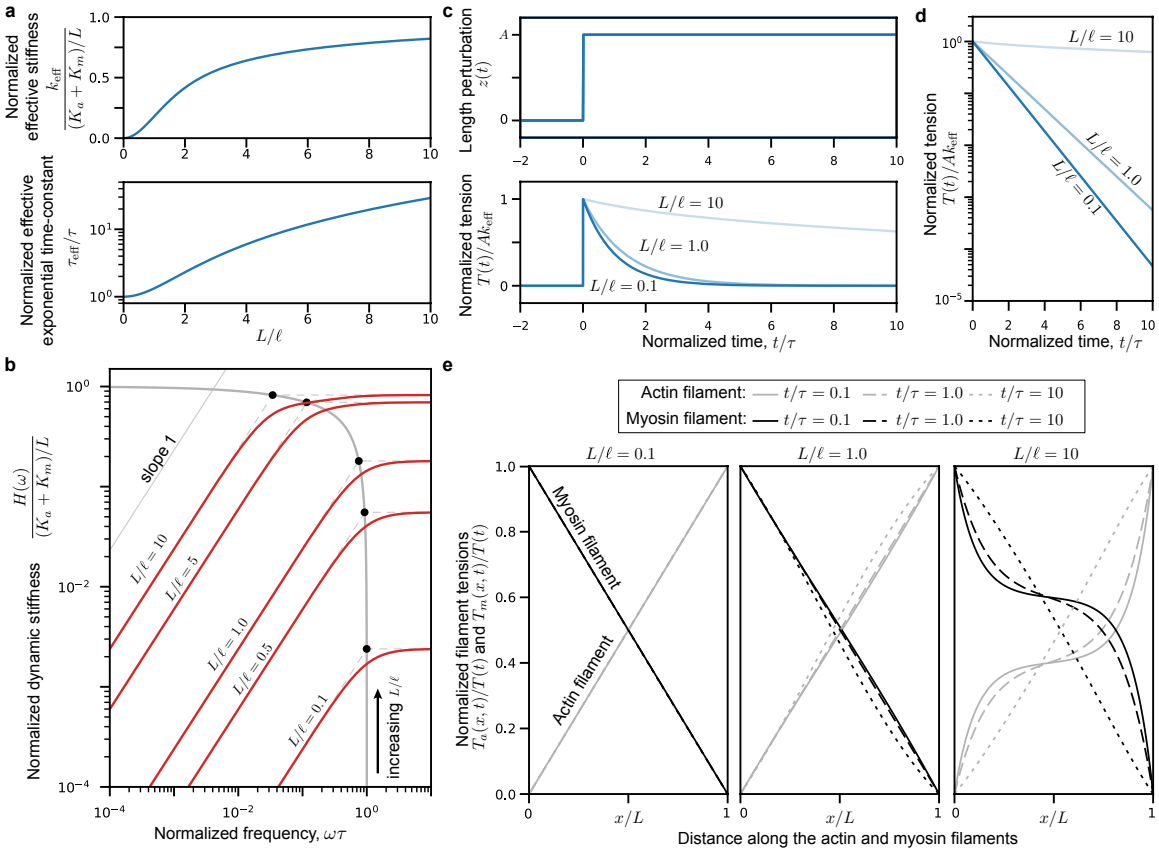

Figure 4.2: Dynamics of the compliant half-sarcomere model. All curves shown are computed using $K_a = 6.5 \cdot 10^4$pN and $K_m = 10^5$pN. **a,** The effective stiffness and exponential time-constant of the half-sarcomere model both grow with the ratio L/ℓ or as crossbridge viscoelasticity becomes comparable to filament compliances. **b,** At all values of L/ℓ, the frequency-dependent behavior of the half-sarcomere model is fluid-like at sufficiently low frequencies and solid-like at high frequencies. The turnover between fluid-like and elastic-like behaviors occurs at lower frequencies and higher stiffnesses as the ratio L/ℓ increases. **c-d,** The time-evolution of the total tension $T(t)$ transmitted across the half-sarcomere and filament tensions $T_a(x,t)$ and $T_m(x,t)$ for a step length perturbation of amplitude A. The curves are obtained by numerically solving equations (4.18 - 4.25)

evaluated along the imaginary line $s = i\omega$ and may be approximated as

$$H(\omega) = \left| \frac{\hat{T}(s)}{\hat{z}(s)} \right|_{s=i\omega} \approx \begin{cases} b\omega \text{ for low frequencies} \\ k_{\text{eff}} \text{ for high frequencies} \end{cases} \tag{4.20}$$

where b is the viscous damping coefficient and k_{eff} is the effective stiffness of the entire half sarcomere. They are evaluated by taking the limits of small and large ω, respectively, as

$$b = \frac{K_a + K_m}{L} \left(\frac{(\frac{L}{\ell})^2 \tau}{2 + (K_a/K_m + K_m/K_a)} \right) \tag{4.21}$$

$$\text{and} \quad k_{\text{eff}} = \frac{K_a + K_m}{L} \left(\frac{(\frac{L}{\ell}) \sinh(\frac{L}{\ell})}{2 + (K_a/K_m + K_m/K_a)\cosh(\frac{L}{\ell}) + \frac{L}{\ell}\sinh(\frac{L}{\ell})} \right). \tag{4.22}$$

The frequency at which the low and high frequency asymptotes meet define an effective time-constant $\tau_{\text{eff}} = b/k_{\text{eff}}$ as

$$\tau_{\text{eff}} = \tau \left(\frac{L/\ell}{\sinh(\frac{L}{\ell})} \right) \left(\frac{2 + (K_a/K_m + K_m/K_a)\cosh(\frac{L}{\ell}) + \frac{L}{\ell}\sinh(\frac{L}{\ell})}{2 + K_a/K_m + K_m/K_a} \right). \tag{4.23}$$

Note that τ is the time-constant of the exponential process used to model the viscoelastic resistance of crossbridge ensembles. A difference between τ and τ_{eff} implies that filament compliance leads to emergent dynamics that are qualitatively distinct from the constituent crossbridge dynamics. For rigid filaments, L/ℓ is much less than unity and the time-constant τ_{eff} is approximately τ so the difference is vanishingly small and half-sarcomere dynamics are identical to crossbridge dynamics. However, for compliant filaments or for $L/\ell \gg 1$, the half-sarcomere dynamics are much slower than underlying crossbridges because the effective time-constant scales as $\tau_{\text{eff}} \sim \tau(\frac{L}{\ell})^2$. A higher effective time-constant amounts to a slower relaxation of tension and a solidification of the half-sarcomere because the viscous fluid-like behavior emerges on timescales much longer or oscillatory frequencies much lower than

crossbridge dynamics would suggest (see figure 4.2a-4.2b).

4.5.3 Spatial inhomogeneties in filaments tension

In addition to slower emergent timescales, filament compliance leads to spatial inhomogeneities in filament tensions that do not appear in half-sarcomere models with rigid filaments. As a point of reference, the homogeneous solution occurs when crossbridge tractions are constant along x and the filament tensions linearly interpolate between zero and the total tension. Figures 4.2c and 4.2d illustrate the inhomogeneities by solving equations (4.4 - 4.10) for the filament tensions, $T_a(x,t)$ and $T_m(x,t)$, in response to a step length perturbation. The solutions in the Laplace domain are

$$\frac{\hat{T}_a(x,s)}{\hat{T}(s)} = \left(\frac{1}{K_m + K_a}\right) * \left(K_a - K_a \cosh\left(\frac{x}{\ell}\sqrt{\hat{h}}\right) + \frac{\left(K_m + K_a \cosh\left(\frac{L}{\ell}\sqrt{\hat{h}}\right)\right)}{\sinh\left(\frac{L}{\ell}\sqrt{\hat{h}}\right)} \sinh\left(\frac{x}{\ell}\sqrt{\hat{h}}\right)\right) \quad (4.24)$$

and

$$\frac{\hat{T}_m(x,s)}{\hat{T}(s)} = \left(\frac{1}{K_m + K_a}\right) * \left(K_m + K_a \cosh\left(\frac{x}{\ell}\sqrt{\hat{h}}\right) - \frac{\left(K_m + K_a \cosh\left(\frac{L}{\ell}\sqrt{\hat{h}}\right)\right)}{\sinh\left(\frac{L}{\ell}\sqrt{\hat{h}}\right)} \sinh\left(\frac{x}{\ell}\sqrt{\hat{h}}\right)\right). \quad (4.25)$$

which, as illustrated in figure 4.2d , simplifies to the homogeneous solution for $L/\ell \ll 1$ and grows as hyperbolic functions for L/ℓ at least comparable to unity. Importantly, although it is currently not possible to measure filament inhomogeneities at sub-micron resolutions, the solutions here predict that the inhomogeneities due to crossbridge-induced tractions act predominantly on the length scale ℓ.

Although further work is necessary, we speculate that the spatial inhomogeneities

observed here due to mechanical interactions between filaments and crossbridges may be a mechanism contributing to a muscle phenomenon known as spontaneous oscillatory contractions (SPOC) [37, 85, 137]. SPOC is the tendency for sub-maximally activated muscle fibers to sustain oscillatory displacements along the fiber's axis and on length scales of several sarcomeres. One proposed theory for SPOC considers a coupling between crossbridge forces and changes in filament lattice spacing as the primary mechanism of the oscillations [37, 138]. The work here suggests a separate mechanism for SPOC without relying on changes in lattice spacing. An extension of the work to include multiple half-sarcomeres in series is certainly needed, and an evaluation of that extension in the context of inter-sarcomeric dynamics [37, 139] also needed. But the driving principles of filament-mediated crossbridge interactions is likely to carry over from the present analysis to a scaled-up model with multiple half-sarcomeres. If filament-mediated crossbridge interactions is the dominant mechanism, then the length scale ℓ or its generalized equivalence in the scaled-up model will necessarily be the dominant oscillatory wavelength observed in SPOC.

4.5.4 Discussion

We use known sarcomere parameters to estimate the length scale ℓ (eqn. 4.19) for an activated muscle and compare it to the overlap length of thick and thin filaments. The filament stiffnesses are estimated to be $K_a \approx 6.5 \cdot 10^4$pN and $K_m \approx 10^5$pN based on measurements of the thin filament and experiments suggesting that thick filaments are 1.5 times as stiff as the thin filaments [127, 128]. The product $M\lambda$ is approximately 10pn/nm^2 based on the magnitude of experimentally measured exponential processes in skeletal and cardiac muscles from different animals [41, 107, 110, 140]. We use $M\lambda = 8.1$pn/nm^2 based on the smallest magnitude of Kawai and Brandt's exponential processes for a rabbit psoas muscle. The true value is likely higher because fiber measurements consist of multiple sarcomeres and therefore include compliant elements

outside the overlap zone. The sarcomere parameters taken together yield $\ell \approx 70$nm whereas the overlap L is approximately 700nm [127, 141]. Thus, because L is at least comparable to ℓ for a fully activated muscle, filament compliance is expected to strongly modulate crossbridge forces.

The compliant half-sarcomere model predicts that filament compliance plays a dominant role in the mapping between microscopic crossbridge models and macroscopic muscle measurements, and that assuming rigid filaments to estimate crossbridge parameters from measurements will lead to mismatched values. For example, a known consequence of filament compliance is that linearly scaling measured muscle stiffness by the number of crossbridges will underestimate the true crossbridge stiffness [39, 130]. However, a less known consequence is that fitting rate constants of multi-state crossbridge models to tension transients, often the frequency-dependent loss and storage moduli of sinusoidal analysis [71, 72], will similarly lead to underestimated values even after accounting for any series compliance outside the overlap zone. The mismatch will be at least an order of magnitude for $L/\ell = 10$ since τ_{eff}/τ would approximately be 25.

The ratio L/ℓ is additionally a function of activation, being zero for a deactivated muscle because there are no cycling crossbridges, *i.e* $M = 0$, so the observation that the effective time-constant τ_{eff} grows monotonically with L/ℓ (see figure 4.2b) is a statement that the half-sarcomere model solidifies with activation. This is because for timescales shorter than τ_{eff}, the half-sarcomere's tension is nearly constant like an elastic solid, whereas for timescales longer the tension relaxes exponentially like a viscous fluid. Increasing τ_{eff} via activation is equivalent to transforming the half-sarcomere from a fluid-like structure into a solid-like structure. Such fluid-to-solid transitions have been predicted for muscles based on biomechanical needs of providing postural stability yet also able to freely yield to rapid motions [16]. Importantly, the transition is in spite of unchanging crossbridge dynamics because the original time-

constant τ is independent of activation, and it is only through filament-mediated interactions between crossbridges that the half-sarcomere model solidifies. Alternative mechanisms for a solidification are also possible if crossbridge cycling drastically slows with intracellular calcium or at large strains, but such mechanisms have not been studied whereas a not insignificant contribution of filaments to the total sarcomere compliance has been directly measured [127, 128]. The compliant half-sarcomere model presented here shows invariably that accounting for filament compliance leads to a slowdown of tension relaxation as more crossbridges are recruited and stretch the filament lattice that they operate on.

Parallels can be drawn between the dynamics of half-sarcomeres and those of disordered actin networks with transient crosslinkers [93, 142, 143]. In both scenarios, a structural backbone to transmit stresses is provided by the filaments that connect together via temporary bonds. These bonds, crossbridges in half-sarcomeres and crosslinkers in disordered actin networks, resist deformations when attached on short timescales and dissipate stored mechanical energy when detaching on longer timescales. The parallels bring forth the question of whether similar filament-mediated interactions between bonds also underlie a fluid-to-solid transition in disordered actin networks. It is important to recognize the vast experimental and theoretical work surrounding disordered actin networks that previously resolved other components necessary for such a transition [43, 143–146], for example, the minimal number of crosslinkers required per filament. The compliant half-sarcomere model here suggests that an additional component may be filament stretching which, if the same principles carry over, allows the disordered network to relax stresses on timescales much longer than the crosslinkers would otherwise allow if they were all independently cycling. Filament bending is also likely to lead to slower stress relaxation but the exact details of how remains unclear. We speculate that the exact interplay of filament stretching and bending with crosslinker dynamics will give rise to a correlation

length scale, or multiple length scales depending on anisotropy, between the strains of the crosslinkers. We also speculate that the interplay will give rise to emergent spatial inhomogeneities in disordered actin networks if the correlation length scales are greater than the average separation between crosslinkers but less than the system size. Although much work remains, the mechanisms and principles derived from the compliant half-sarcomere model motivate a deeper look into filament-mediated crosslinker interactions that may prove to be a necessary component of fluid-to-solid transitions in disordered actin networks with transient crosslinkers.

Chapter 5

Conclusions and future directions

5.1 Conclusions

The thesis presented efforts to connect scales and address the shortcomings of two widely used classes of striated muscle models, a major objective of neuromuscular research. The first class consists of macroscopic, phenomenological models based on experimental measurements of muscle forces. Although accurate, these models are not easily interpretable in terms of known mechanochemical cycle of actomyosin crossbridges that ultimately drive muscle forces. The second class of models builds up from crossbridge dynamics to capture muscle forces. However, these microscopic models employ more biophysical parameters than have been directly measured.

Chapter 2 derived the viscoelastic rheology of multiple ensemble crossbridge models with varying degrees of complexity. It showed that the viscoelasticity comprised of exponential processes, which is consistent with sinusoidal experiments of muscles. Each exponential process of the ensemble viscoelasticity associates with a peak in the derivative of the steady-state bond distributions of crossbridges, and this finding suggests a direct connection between measured muscle rheology and ensemble crossbridge dynamics.

Chapter 3 considers the rheological basis for muscle forces when a striated mus-

cle is subject to sinusoidal length perturbations and piecewise periodic activations. The closed-loop trajectory obtained by plotting length perturbations against forces is commonly known as a muscle work loop. It was shown that the shapes of work loops are consistent with a periodic transition between two underlying basis ellipses. Each ellipse is a graphical representation of a striated muscle's loss and storage moduli at fixed activation. The findings of chapter 3 thus put forth a parameterization of work loop shape and the mechanical actuation that the shape provides, which previously was often parsed in terms of the work loop's enclosed area rather than its shape.

Chapter 4 introduces thick and thin filament compliances into ensemble crossbridge models as a form of mechanical cooperativity between crossbridges. It finds that a length scale arises from a partitioning of strains between the filaments and crossbridges and, using estimates of sarcomere parameters, also finds that the filaments store an appreciable portion of elastic strains. A consequence of this is that the entire system relaxes stresses slower than if the filaments were rigid in a manner depending on the number of crossbridges. In other words, the relaxation timescales of the system are size-dependent, and whether the model can exhibit either solid-like or fluid-like behaviors depends on the number of participating crossbridges.

5.2 Future directions

It is the author's opinion that identifying new potential research directions previously hindered by a lack of understanding is a result as important as the thesis itself. There are research directions on both near and far horizons that the author hopes to tackle or make progress towards during his academic career. The author also hopes that the thesis will be of academic value to others in their research pursuits.

5.2.1 A general framework for tunable materials

The splicing hypothesis introduced in chapter 3 is an effort to accommodate tunable materials whose forces depend on both mechanical perturbations and external stimuli. It extends current rheological methods designed for passive or otherwise non-tunable materials by assuming a separation of timescales between the dynamics of changing stimuli and of the material's response to being perturbed. This separation is not valid in all situations and the splicing hypothesis is thus a limiting case of a more general framework. It is certainly useful, as exemplified by the contents of chapter 3, but ultimately an incomplete description of the rheology of tunable materials.

There are many tunable materials [27, 31, 32], each with different physical processes underlying their tunability, but the set of principles on how to translate the tunability into a desired mechanical actuation may be common to all tunable materials. The framework which generalizes on the splicing hypothesis is likely to be this set of principles. It remains to be developed and doing so would have broad implications for multiple scientific disciplines, including biology, engineering, robotics, and materials science. The framework would help understand the biomechanical functions that contractile apparatus, like striated muscles, provide to biology. It would also help design new mechanical interfaces and actuators built from tunable materials, which have gained traction over the past decade due to their ability to endure large deformations without damage [28–30]. And in materials science, it would help direct new experimental methods to characterize the properties of tunable materials, which current rheological methods are not designed for.

5.2.2 Fluid-to-solid transitions in muscles and other materials

In contradiction to a core tenet of muscle mechanics that actomyosin crossbridges are independent of each other, further investigations into crossbridge-crossbridge interactions may lead to viscoelastic rheologies not previously considered. A consequence of the tenet that Chapter 2 showed is that the viscoelasticity of an ensemble of crossbridges depends trivially on the ensemble's size. Namely, the magnitude of the exponential process underlying the ensemble's viscoelastic rheology scales linearly with ensemble size but the timescale of the process remains unchanging. Thus the expected behavior for muscles modeled by crossbridge ensembles is that a solid-like muscle remains solid-like regardless of ensemble size. A fluid-like muscle similarly remains fluid-like. Such muscle models cannot transition between solid-like and fluid-like behaviors as neural inputs modulate ensemble size despite biomechanical arguments suggesting otherwise.

Motivated by the jamming transition observed in materials [35] in which the relaxation of internal stresses drastically slows as a function of particle density, effective temperature, and external shearing, Chapter 4 showed that a relaxation slowdown can also occur in crossbridge ensembles. Specifically, it showed that the thick and thin filament compliance permit ensemble size-dependent timescales such that the ensemble is fluid-like at low crossbridge density and solid-like at higher densities. It showed one plausible mechanism for muscle models to undergo a fluid-to-solid transition that is reminiscent of the jamming transition where ensemble size takes on the role of particle density. Further investigations into muscle rheology and crossbridge dynamics may draw stronger connections to the jamming transition and bring about new insights to other materials that similarly undergo a fluid-to-solid transition.

Bibliography

[1] Kiisa Nishikawa, Andrew A Biewener, Peter Aerts, Anna N Ahn, Hillel J Chiel, Monica A Daley, Thomas L Daniel, Robert J Full, Melina E Hale, Tyson L Hedrick, et al. Neuromechanics: an integrative approach for understanding motor control. *Integrative and Comparative Biology*, 47(1):16–54, 2007.

[2] Andrew Biewener and Sheila Patek. *Animal locomotion*. Oxford University Press, 2018.

[3] SS An, TR Bai, JHT Bates, JL Black, RH Brown, V Brusasco, P Chitano, L Deng, M Dowell, DH Eidelman, et al. Airway smooth muscle dynamics: a common pathway of airway obstruction in asthma. *European Respiratory Journal*, 29(5):834–860, 2007.

[4] Neville Hogan. Skeletal muscle impedance in the control of motor actions. *Journal of Mechanics in Medicine and Biology*, 2(03n04):359–373, 2002.

[5] Steven A Niederer, Kenneth S Campbell, and Stuart G Campbell. A short history of the development of mathematical models of cardiac mechanics. *Journal of molecular and cellular cardiology*, 127:11–19, 2019.

[6] Yuan-Cheng Fung. *Biomechanics: mechanical properties of living tissues*. Springer Science & Business Media, 2013.

[7] Felix E Zajac. Muscle and tendon: properties, models, scaling, and application to biomechanics and motor control. *Critical Reviews in Biomedical Engineering*, 17(4): 359–411, 1989.

[8] Emilio Bizzi, William Chapple, and Neville Hogan. Mechanical properties of muscles: Implications for motor control. *Trends in Neurosciences*, 5:395–398, 1982.

[9] Neville Hogan, Emilio Bizzi, Ferdinando A Mussa-Ivaldi, and Tamar Flash. Controlling multijoint motor behavior. *Exercise and Sport Sciences Reviews*, 15:153–190, 1987.

[10] Roland S Johansson and Kelly J Cole. Grasp stability during manipulative actions. *Canadian Journal of Physiology and Pharmacology*, 72(5):511–524, 1994.

[11] Andrew A Biewener and Thomas J Roberts. Muscle and tendon contributions to force, work, and elastic energy savings: a comparative perspective. *Exercise and Sport Sciences Reviews*, 28(3):99–107, 2000.

[12] David C Lin and W Zev Rymer. Damping actions of the neuromuscular system with inertial loads: soleus muscle of the decerebrate cat. *Journal of Neurophysiology*, 83 (2):652–658, 2000.

[13] Nicolai Konow, Emanuel Azizi, and Thomas J Roberts. Muscle power attenuation by tendon during energy dissipation. *Proceedings of the Royal Society B: Biological Sciences*, 279(1731):1108–1113, 2012.

[14] RW Lymn and Edwin W Taylor. Mechanism of adenosine triphosphate hydrolysis by actomyosin. *Biochemistry*, 10(25):4617–4624, 1971.

[15] Andrew F Huxley and Ro M Simmons. Proposed mechanism of force generation in striated muscle. *Nature*, 233(5321):533–538, 1971.

[16] Khoi D Nguyen, Neelima Sharma, and Madhusudhan Venkadesan. Active viscoelasticity of sarcomeres. *Frontiers in Robotics and AI*, 2018. doi: 10.3389/frobt.2018.00069.

[17] Neil T Roach, Madhusudhan Venkadesan, Michael J Rainbow, and Daniel E Lieberman. Elastic energy storage in the shoulder and the evolution of high-speed throwing in homo. *Nature*, 498(7455):483–6, Jun 2013. doi: 10.1038/nature12267.

[18] Lei Cui, Eric J Perreault, Huub Maas, and Thomas G Sandercock. Modeling short-range stiffness of feline lower hindlimb muscles. *Journal of Biomechanics*, 41(9): 1945–1952, 2008.

[19] S Sponberg and R J Full. Neuromechanical response of musculo-skeletal structures in cockroaches during rapid running on rough terrain. *J Exp Biol*, 211(Pt 3):433–46, Feb 2008. doi: 10.1242/jeb.012385.

[20] Waleed A Farahat and Hugh M Herr. Optimal workloop energetics of muscle-actuated systems: an impedance matching view. *PLoS Computational Biology*, 6(6):e1000795, 2010.

[21] Xiao Hu, Wendy M Murray, and Eric J Perreault. Muscle short-range stiffness can be used to estimate the endpoint stiffness of the human arm. *Journal of Neurophysiology*, 105(4):1633–1641, 2011.

[22] Gregory S Sawicki, Benjamin D Robertson, Emanuel Azizi, and Thomas J Roberts. Timing matters: tuning the mechanics of a muscle–tendon unit by adjusting stimulation phase during cyclic contractions. *Journal of Experimental Biology*, 218(19): 3150–3159, 2015.

[23] Robert K Josephson. Mechanical power output from striated muscle during cyclic contraction. *Journal of Experimental Biology*, 114(1):493–512, 1985.

[24] Anna N Ahn and Robert J Full. A motor and a brake: two leg extensor muscles acting at the same joint manage energy differently in a running insect. *Journal of Experimental Biology*, 205(3):379–389, 2002.

[25] Anna N Ahn, Kenneth Meijer, and Robert J Full. In situ muscle power differs without varying in vitro mechanical properties in two insect leg muscles innervated by the same motor neuron. *Journal of Experimental Biology*, 209(17):3370–3382, 2006. doi: 10.1242/jeb.02392.

[26] Kiisa C Nishikawa, Jenna A Monroy, and Uzma Tahir. Muscle function from organisms to molecules. *Integrative and Comparative Biology*, 58(2):194–206, 2018. doi: 10.1093/icb/icy023.

[27] Lindsey Hines, Kirstin Petersen, Guo Zhan Lum, and Metin Sitti. Soft actuators for small-scale robotics. *Advanced Materials*, 29(13):1603483, 2017. doi: 10.1002/adma.201603483.

[28] Carmel Majidi. Soft-matter engineering for soft robotics. *Advanced Materials Technologies*, 4(2):1800477, 2019. doi: 10.1002/admt.201800477.

[29] Sangbae Kim, Cecilia Laschi, and Barry Trimmer. Soft robotics: a bioinspired evolution in robotics. *Trends in biotechnology*, 31(5):287–294, 2013.

[30] Daniela Rus and Michael T Tolley. Design, fabrication and control of soft robots. *Nature*, 521(7553):467–475, 2015.

[31] Hyunwoo Yuk, Daeyeon Kim, Honggu Lee, Sungho Jo, and Jennifer H Shin. Shape memory alloy-based small crawling robots inspired by c. elegans. *Bioinspiration & Biomimetics*, 6(4):046002, 2011.

[32] Juan De Vicente, Daniel J Klingenberg, and Roque Hidalgo-Alvarez. Magnetorheological fluids: a review. *Soft matter*, 7(8):3701–3710, 2011.

[33] Robert F Shepherd, Filip Ilievski, Wonjae Choi, Stephen A Morin, Adam A Stokes, Aaron D Mazzeo, Xin Chen, Michael Wang, and George M Whitesides. Multigait soft robot. *Proceedings of the National Academy of Sciences*, 108(51):20400–20403, 2011.

[34] Sidney R Nagel. Experimental soft-matter science. *Reviews of Modern Physics*, 89 (2):025002, 2017. doi: 10.1103/RevModPhys.89.025002.

[35] Andrea J Liu and Sidney R Nagel. The jamming transition and the marginally jammed solid. *Annu. Rev. Condens. Matter Phys.*, 1(1):347–369, 2010.

[36] Daniel TN Chen, Qi Wen, Paul A Janmey, John C Crocker, and Arjun G Yodh. Rheology of soft materials. *Annu. Rev. Condens. Matter Phys.*, 1(1):301–322, 2010. doi: 10.1146/annurev-conmatphys-070909-104120.

[37] Fumiaki Kono, Seitaro Kawai, Yuta Shimamoto, and Shin'ichi Ishiwata. Nanoscopic changes in the lattice structure of striated muscle sarcomeres involved in the mechanism of spontaneous oscillatory contraction (spoc). *Scientific reports*, 10(1):1–14, 2020.

[38] John Sleep, Alexandre Lewalle, and David Smith. Reconciling the working strokes of a single head of skeletal muscle myosin estimated from laser-trap experiments and crystal structures. *Proceedings of the National Academy of Sciences*, 103(5):1278–1282, 2006.

[39] AF Huxley and Sl Tideswell. Filament compliance and tension transients in muscle. *Journal of Muscle Research & Cell Motility*, 17(4):507–511, 1996.

[40] Peter MH Rack and DR Westbury. The short range stiffness of active mammalian muscle and its effect on mechanical properties. *The Journal of Physiology*, 240(2): 331–350, 1974.

[41] Masataka Kawai and Philip W Brandt. Sinusoidal analysis: a high resolution method for correlating biochemical reactions with physiological processes in activated skeletal muscles of rabbit, frog and crayfish. *Journal of Muscle Research & Cell Motility*, 1 (3):279–303, 1980.

[42] Nicholas W Tschoegl. *The phenomenological theory of linear viscoelastic behavior: an introduction*. Springer Science & Business Media, 2012.

[43] ML Gardel, Jennifer Hyunjong Shin, FC MacKintosh, L Mahadevan, Paul Matsudaira, and David A Weitz. Elastic behavior of cross-linked and bundled actin networks. *Science*, 304(5675):1301–1305, 2004.

[44] Gijsje H Koenderink, Zvonimir Dogic, Fumihiko Nakamura, Poul M Bendix, Frederick C MacKintosh, John H Hartwig, Thomas P Stossel, and David A Weitz. An active biopolymer network controlled by molecular motors. *Proceedings of the National Academy of Sciences*, 106(36):15192–15197, 2009.

[45] David A Sleboda and Thomas J Roberts. Internal fluid pressure influences muscle contractile force. *Proceedings of the National Academy of Sciences*, 117(3):1772–1778, 2020.

[46] Brian R MacIntosh and Meredith B MacNaughton. The length dependence of muscle active force: considerations for parallel elastic properties. *Journal of Applied Physiology*, 98(5):1666–1673, 2005.

[47] YC Fung. Comparison of different models of the heart muscle. *Journal of Biomechanics*, 4(4):289–295, 1971. doi: 10.1016/0021-9290(71)90035-2.

[48] Emanuel Todorov. On the role of primary motor cortex in arm movement control. *Progress in Motor Control III*, 6:125–166, 2003.

[49] SL Lindstedt, PC LaStayo, and TE Reich. When active muscles lengthen: properties and consequences of eccentric contractions. *Physiology*, 16(6):256–261, 2001. doi: 10.1152/physiologyonline.2001.16.6.256.

[50] Sabrina SM Lee, Allison S Arnold, Maria de Boef Miara, Andrew A Biewener, and James M Wakeling. Accuracy of gastrocnemius muscles forces in walking and running goats predicted by one-element and two-element hill-type models. *Journal of Biomechanics*, 46(13):2288–2295, 2013.

[51] Thomas G Sandercock and CJ Heckman. Force from cat soleus muscle during imposed locomotor-like movements: experimental data versus hill-type model predictions. *Journal of Neurophysiology*, 77(3):1538–1552, 1997.

[52] Taylor JM Dick, Andrew A Biewener, and James M Wakeling. Comparison of human gastrocnemius forces predicted by hill-type muscle models and estimated from ultrasound images. *Journal of Experimental Biology*, 220(9):1643–1653, 2017.

[53] N Rice, S Jeong, and K Nishikawa. How do muscle length and activation interact to determine muscle force production? In *Integrative and Comparative Biology*, volume 60, pages E195–E195. Oxford University Press, 2020.

[54] Eric J. Perreault, Charles J. Heckman, and Thomas G. Sandercock. Hill muscle model errors during movement are greatest within the physiologically relevant range of motor unit firing rates. *Journal of Biomechanics*, 36(2):211–8, 2003. doi: http://dx.doi.org/10.1016/S0021-9290(02)00332-9. URL `https://search.proquest.com/scholarly-journals/hill-muscle-model-errors-during-movement-are/docview/1035112279/se-2?accountid=15172`.

[55] Friedl De Groote and Antoine Falisse. Perspective on musculoskeletal modelling and predictive simulations of human movement to assess the neuromechanics of gait. *Proceedings of the Royal Society B*, 288(1946):20202432, 2021.

[56] Matthew C O'Neill, Leng-Feng Lee, Susan G Larson, Brigitte Demes, Jack T Stern, and Brian R Umberger. A three-dimensional musculoskeletal model of the chimpanzee (pan troglodytes) pelvis and hind limb. *Journal of Experimental Biology*, 216(19): 3709–3723, 2013.

[57] Ross H Miller. A comparison of muscle energy models for simulating human walking in three dimensions. *Journal of biomechanics*, 47(6):1373–1381, 2014.

[58] Kenneth C Holmes. The swinging lever-arm hypothesis of muscle contraction. *Current Biology*, 7(2):R112–R118, 1997.

[59] Andrew F Huxley. Muscle structure and theories of contraction. *Prog. Biophys. Biophys. Chem*, 7:255–318, 1957.

[60] Bradley M. Palmer. *A Strain-Dependency of Myosin Off-Rate Must Be Sensitive to Frequency to Predict the B-Process of Sinusoidal Analysis*, pages 57–75. Springer New York, New York, NY, 2010. ISBN 978-1-4419-6366-6. doi: 10.1007/978-1-4419-6366-6_4.

[61] Chao Liu, Masataka Kawana, Dan Song, Kathleen M Ruppel, and James A Spudich. Controlling load-dependent kinetics of β-cardiac myosin at the single-molecule level. *Nature structural & molecular biology*, 25(6):505–514, 2018.

[62] George Ireneus Zahalak. A distribution-moment approximation for kinetic theories of muscular contraction. *Mathematical Biosciences*, 55(1-2):89–114, 1981.

[63] G. I. Zahalak. A Comparison of the Mechanical Behavior of the Cat Soleus Muscle With a Distribution-Moment Model. *Journal of Biomechanical Engineering*, 108(2): 131–140, 05 1986. ISSN 0148-0731. doi: 10.1115/1.3138592. URL `https://doi.org/10.1115/1.3138592`.

[64] George I Zahalak and Shi-Ping Ma. Muscle activation and contraction: constitutive relations based directly on cross-bridge kinetics. *Journal of Biomechanical Engineering*, 112(1):52–62, 1990.

[65] Gerald K. Cole, Anton J. van den Bogert, Walter Herzog, and Karin G.M. Gerritsen. Modelling of force production in skeletal muscle undergoing stretch. *Journal of Biomechanics*, 29(8):1091–1104, 1996. ISSN 0021-9290. doi: https://doi.org/10.1016/0021-9290(96)00005-X. URL `https://www.sciencedirect.com/science/article/pii/002192909600005X`.

[66] A.J van den Bogert, K.G.M Gerritsen, and G.K Cole. Human muscle modelling from a user's perspective. *Journal of Electromyography and Kinesiology*, 8(2):119–124, 1998. ISSN 1050-6411. doi: https://doi.org/10.1016/S1050-6411(97)00028-X. URL `https://www.sciencedirect.com/science/article/pii/S105064119700028X`.

[67] Bradley M Palmer, Douglas M Swank, Mark S Miller, Bertrand CW Tanner, Markus Meyer, and Martin M LeWinter. Enhancing diastolic function by strain-dependent detachment of cardiac myosin crossbridges. *Journal of General Physiology*, 152(4), 2020.

[68] Katsuhiko Ogata. *System dynamics*, volume 13. Pearson/Prentice Hall Upper Saddle River, NJ, 2004.

[69] David Weitz, Hans Wyss, and Ryan Larsen. Oscillatory rheology: Measuring the viscoelastic behaviour of soft materials. *GIT Laboratory Journal Europe*, 11(3-4): 68–70, 2007.

[70] Khoi D Nguyen and Madhusudhan Venkadesan. Rheological basis of skeletal muscle work loops. *arXiv*, [cond-mat.soft]:2005.07238, 2021.

[71] M Murase, H Tanaka, K Nishiyama, and H Shimizu. A three-state model for oscillation in muscle: sinusoidal analysis. *Journal of Muscle Research & Cell Motility*, 7(1): 2–10, 1986.

[72] DA Smith. A strain-dependent ratchet model for [phosphate]-and [atp]-dependent muscle contraction. *Journal of Muscle Research & Cell Motility*, 19(2):189–211, 1998.

[73] Vincenzo Lombardi and Gabriella Piazzesi. The contractile response during steady lengthening of stimulated frog muscle fibres. *The Journal of Physiology*, 431(1):141–171, 1990.

[74] Masataka Kawai, Yasutake Saeki, and Yan Zhao. Crossbridge scheme and the kinetic constants of elementary steps deduced from chemically skinned papillary and trabecular muscles of the ferret. *Circulation Research*, 73(1):35–50, 1993.

[75] Masataka Kawai, Robert Stehle, Gabriele Pfitzer, and Bogdan Iorga. Phosphate has dual roles in cross-bridge kinetics in rabbit psoas single myofibrils. *Journal of General Physiology*, 153(3), 2021.

[76] PJ Hunter, AD McCulloch, and HEDJ Ter Keurs. Modelling the mechanical properties of cardiac muscle. *Progress in Biophysics and Molecular Biology*, 69(2-3):289–331, 1998.

[77] Walter Herzog. History dependence of skeletal muscle force production: implications for movement control. *Human movement science*, 23(5):591–604, 2004.

[78] Aditya Jaishankar and Gareth H McKinley. Power-law rheology in the bulk and at the interface: quasi-properties and fractional constitutive equations. *Proceedings of the Royal Society A: Mathematical, Physical and Engineering Sciences*, 469(2149): 20120284, 2013.

[79] Ronald L Bagley and PJ Torvik. A theoretical basis for the application of fractional calculus to viscoelasticity. *Journal of Rheology*, 27(3):201–210, 1983.

[80] Philip Kollmannsberger and Ben Fabry. Linear and nonlinear rheology of living cells. *Annual Review of Materials Research*, 41:75–97, 2011. doi: 10.1146/annurev-matsci-062910-100351.

[81] Sam Walcott. Muscle activation described with a differential equation model for large ensembles of locally coupled molecular motors. *Physical Review E*, 90(4):042717, 2014.

[82] Srboljub M Mijailovich, Jeffrey J Fredberg, and James P Butler. On the theory of muscle contraction: filament extensibility and the development of isometric force and stiffness. *Biophysical Journal*, 71(3):1475, 1996.

[83] Thomas L Daniel, Alan C Trimble, and P Bryant Chase. Compliant realignment of binding sites in muscle: transient behavior and mechanical tuning. *Biophysical Journal*, 74(4):1611–1621, 1998.

[84] Khoi D Nguyen and Madhusudhan Venkadesan. The compliance-induced slowdown of stress relaxation in active sarcomeres. *Biophysical Journal*, 120(3):62a, 2021.

[85] Yuta Shimamoto, Madoka Suzuki, Sergey V Mikhailenko, Kenji Yasuda, and Shin'ichi Ishiwata. Inter-sarcomere coordination in muscle revealed through individual sarcomere response to quick stretch. *Proceedings of the National Academy of Sciences*, 106 (29):11954–11959, 2009.

[86] Kenneth S Campbell. Interactions between connected half-sarcomeres produce emergent mechanical behavior in a mathematical model of muscle. *PLoS Computational Biology*, 5(11):e1000560, 2009.

[87] Kiisa C Nishikawa, Jenna A Monroy, Theodore E Uyeno, Sang Hoon Yeo, Dinesh K Pai, and Stan L Lindstedt. Is titin a 'winding filament'? a new twist on muscle contraction. *Proceedings of the royal society B: Biological sciences*, 279(1730):981–990, 2012.

[88] Krysta Powers, Gudrun Schappacher-Tilp, Azim Jinha, Tim Leonard, Kiisa Nishikawa, and Walter Herzog. Titin force is enhanced in actively stretched skeletal muscle. *Journal of Experimental Biology*, 217(20):3629–3636, 2014.

[89] William H Press, H William, Saul A Teukolsky, A Saul, William T Vetterling, and Brian P Flannery. *Numerical recipes 3rd edition: The art of scientific computing*. Cambridge University Press, 2007.

[90] Pauli Virtanen, Ralf Gommers, Travis E. Oliphant, Matt Haberland, Tyler Reddy, David Cournapeau, Evgeni Burovski, Pearu Peterson, Warren Weckesser, Jonathan Bright, Stéfan J. van der Walt, Matthew Brett, Joshua Wilson, K. Jarrod Millman, Nikolay Mayorov, Andrew R. J. Nelson, Eric Jones, Robert Kern, Eric Larson, C J Carey, İlhan Polat, Yu Feng, Eric W. Moore, Jake VanderPlas, Denis Laxalde, Josef Perktold, Robert Cimrman, Ian Henriksen, E. A. Quintero, Charles R. Harris, Anne M. Archibald, Antônio H. Ribeiro, Fabian Pedregosa, Paul van Mulbregt, and SciPy 1.0 Contributors. SciPy 1.0: Fundamental Algorithms for Scientific Computing in Python. *Nature Methods*, 17:261–272, 2020. doi: 10.1038/s41592-019-0686-2.

[91] Margaret L. Gardel, Karen E. Kasza, Clifford P. Brangwynne, Jiayu Liu, and David A. Weitz. Mechanical response of cytoskeletal networks. In *Biophysical Tools for Biologists, Volume Two: In Vivo Techniques*, volume 89 of *Methods in Cell Biology*, chapter 19, pages 487 – 519. Academic Press, 2008. doi: 10.1016/S0091-679X(08)00619-5.

[92] Karen E Kasza, Amy C Rowat, Jiayu Liu, Thomas E Angelini, Clifford P Brangwynne, Gijsje H Koenderink, and David A Weitz. The cell as a material. *Current Opinion in Cell Biology*, 19(1):101–107, 2007. doi: 10.1016/j.ceb.2006.12.002.

[93] Shiladitya Banerjee, Margaret L Gardel, and Ulrich S Schwarz. The actin cytoskeleton as an active adaptive material. *Annual Review of Condensed Matter Physics*, 11:421–439, 2020.

[94] Stan L Lindstedt and Hans H Hoppeler. Expanding knowledge of contracting muscle, 2016.

[95] Pierre-Gilles de Gennes. Un muscle artificiel semi-rapide. *Comptes Rendus de l'Académie des Sciences-Series IIB-Mechanics-Physics-Chemistry-Astronomy*, 324(5): 343–348, 1997. doi: 10.1016/S1251-8069(99)80044-X.

[96] John DW Madden, Nathan A Vandesteeg, Patrick A Anquetil, Peter GA Madden, Arash Takshi, Rachel Z Pytel, Serge R Lafontaine, Paul A Wieringa, and Ian W Hunter. Artificial muscle technology: physical principles and naval prospects. *IEEE Journal of Oceanic Engineering*, 29(3):706–728, 2004. doi: 10.1109/JOE.2004.833135.

[97] Michael H. Dickinson, Claire T. Farley, Robert J. Full, M. A. R. Koehl, Rodger Kram, and Steven Lehman. How animals move: An integrative view. *Science*, 288 (5463):100–106, 2000. ISSN 0036-8075. doi: 10.1126/science.288.5463.100. URL `https://science.sciencemag.org/content/288/5463/100`.

[98] Rob S James, Iain S Young, Valerie M Cox, David F Goldspink, and John D Altringham. Isometric and isotonic muscle properties as determinants of work loop power output. *Pflügers Archiv*, 432(5):767–774, 1996. doi: 10.1007/s004240050197.

[99] Dilson E. Rassier and Walter Herzog. Considerations on the history dependence of muscle contraction. *Journal of Applied Physiology*, 96(2):419–427, 2004. doi: 10.1152/japplphysiol.00653.2003. URL `https://doi.org/10.1152/japplphysiol.00653.2003`. PMID: 14715673.

[100] Martin Lakie and Kenneth S. Campbell. Muscle thixotropy—where are we now? *Journal of Applied Physiology*, 126(6):1790–1799, 2019. doi: 10.1152/japplphysiol.00788.2018. URL `https://doi.org/10.1152/japplphysiol.00788.2018`. PMID: 31070959.

[101] KE Machin and John William Sutton Pringle. The physiology of insect fibrillar muscle iii. the effect of sinusoidal changes of length on a beetle flight muscle. *Proceedings of the Royal Society of London. Series B. Biological Sciences*, 152(948):311–330, 1960. doi: 10.1098/rspb.1960.0041.

[102] A. N. Ahn. How muscles function – the work loop technique. *Journal of Experimental Biology*, 215(7):1051–1052, 2012. ISSN 0022-0949. doi: 10.1242/jeb.062752. URL `https://jeb.biologists.org/content/215/7/1051`.

[103] Nicholas W Tschoegl. *The phenomenological theory of linear viscoelastic behavior: an introduction*. Springer-Verlag Berlin Heidelberg, 1 edition, 1989.

[104] Randy H Ewoldt, AE Hosoi, and Gareth H McKinley. New measures for characterizing nonlinear viscoelasticity in large amplitude oscillatory shear. *Journal of Rheology*, 52 (6):1427–1458, 2008. doi: 10.1122/1.2970095.

[105] Kyu Hyun, Manfred Wilhelm, Christopher O Klein, Kwang Soo Cho, Jung Gun Nam, Kyung Hyun Ahn, Seung Jong Lee, Randy H Ewoldt, and Gareth H McKinley. A review of nonlinear oscillatory shear tests: Analysis and application of large amplitude oscillatory shear (LAOS). *Progress in Polymer Science*, 36(12):1697–1753, 2011. doi: 10.1016/j.progpolymsci.2011.02.002.

[106] Jules Antoine Lissajous. Mémoire sur l'étude optique des mouvements vibratoires. *Ann. Chim. Phys. Ser. 3*, 51:147, 1857.

[107] Bertrand CW Tanner, Yuan Wang, David W Maughan, and Bradley M Palmer. Measuring myosin cross-bridge attachment time in activated muscle fibers using stochastic vs. sinusoidal length perturbation analysis. *Journal of Applied Physiology*, 110(4): 1101–1108, 2011. doi: 10.1152/japplphysiol.00800.2010.

[108] Juan De Vicente, Daniel J Klingenberg, and Roque Hidalgo-Alvarez. Magnetorheological fluids: a review. *Soft Matter*, 7(8):3701–3710, 2011. doi: 10.1039/C0SM01221A.

[109] Po MH Rack. The behaviour of a mammalian muscle during sinusoidal stretching. *The journal of physiology*, 183(1):1, 1966.

[110] Bradley M Palmer, Takeki Suzuki, Yuan Wang, William D Barnes, Mark S Miller, and David W Maughan. Two-state model of acto-myosin attachment-detachment predicts c-process of sinusoidal analysis. *Biophysical Journal*, 93(3):760–769, 2007. doi: 10.1529/biophysj.106.101626.

[111] Jagir Baxi, Chris J Barclay, and Colin L Gibbs. Energetics of rat papillary muscle during contractions with sinusoidal length changes. *American Journal of Physiology-Heart and Circulatory Physiology*, 278(5):H1545–H1554, 2000.

[112] Archibald Vivian Hill. The heat of shortening and the dynamic constants of muscle. *Proceedings of the Royal Society of London. Series B-Biological Sciences*, 126(843): 136–195, 1938. doi: 10.1098/rspb.1938.0050.

[113] Timothy P Johnson and Ian A Johnston. Power output of fish muscle fibres performing oscillatory work: effects of acute and seasonal temperature change. *Journal of Experimental Biology*, 157(1):409–423, 1991.

[114] JD Altringham and IA Johnston. The mechanical properties of polyneuronally innervated, myotomal muscle fibres isolated from a teleost fish (myoxocephalus scorpius). *Pflügers Archiv*, 412(5):524–529, 1988.

[115] Priyanka Gupta, Dinu F Albeanu, and Upinder S Bhalla. Olfactory bulb coding of odors, mixtures and sniffs is a linear sum of odor time profiles. *Nature neuroscience*, 18(2):272, 2015.

[116] PL Weiss, IW Hunter, and RE Kearney. Human ankle joint stiffness over the full range of muscle activation levels. *Journal of biomechanics*, 21(7):539–544, 1988.

[117] John D Altringham and Ian A Johnston. Scaling effects on muscle function: power output of isolated fish muscle fibres performing oscillatory work. *Journal of Experimental Biology*, 151(1):453–467, 1990.

[118] Graham N Askew and Richard L Marsh. The effects of length trajectory on the mechanical power output of mouse skeletal muscles. *Journal of Experimental Biology*, 200(24):3119–3131, 1997.

[119] Gerrie P Farman, Edward J Allen, Kelly Q Schoenfelt, Peter H Backx, and Pieter P De Tombe. The role of thin filament cooperativity in cardiac length-dependent calcium activation. *Biophysical Journal*, 99(9):2978–2986, 2010.

[120] Massimo Reconditi, Marco Caremani, Francesca Pinzauti, Joseph D Powers, Theyencheri Narayanan, Ger JM Stienen, Marco Linari, Vincenzo Lombardi, and Gabriella Piazzesi. Myosin filament activation in the heart is tuned to the mechanical task. *Proceedings of the National Academy of Sciences*, 114(12):3240–3245, 2017.

[121] Elise Burmeister Getz, Roger Cooke, and Steven L. Lehman. Phase transition in force during ramp stretches of skeletal muscle. *Biophysical Journal*, 75(6):2971–2983, 2021/03/04 1998. doi: 10.1016/S0006-3495(98)77738-0. URL `https://doi.org/10.1016/S0006-3495(98)77738-0`.

[122] Walter Herzog. *Skeletal muscle mechanics: from mechanisms to function*. John Wiley & Sons, 2000.

[123] Tarald O Kvålseth. Cautionary note about R^2. *The American Statistician*, 39(4): 279–285, 1985.

[124] Mario Bernardo, Chris Budd, Alan Richard Champneys, and Piotr Kowalczyk. *Piecewise-smooth dynamical systems: theory and applications*, volume 163. Springer Science & Business Media, 2008.

[125] Johan Grasman. *Relaxation Oscillations*, pages 1475–1488. Springer New York, New York, NY, 2011. ISBN 978-1-4614-1806-1.

[126] HE Huxley. The double array of filaments in cross-striated muscle. *The Journal of Biophysical and Biochemical Cytology*, 3(5):631–648, 1957.

[127] Hiroaki Kojima, Akihiko Ishijima, and Toshio Yanagida. Direct measurement of stiffness of single actin filaments with and without tropomyosin by in vitro nanomanipulation. *Proceedings of the National Academy of Sciences*, 91(26):12962–12966, 1994.

[128] Katsuzo Wakabayashi, Yasunobu Sugimoto, Hidehiro Tanaka, Yutaka Ueno, Yasunori Takezawa, and Yoshiyuki Amemiya. X-ray diffraction evidence for the extensibility of actin and myosin filaments during muscle contraction. *Biophysical Journal*, 67(6): 2422–2435, 1994.

[129] Hugh E Huxley, Alex Stewart, Hernando Sosa, and Tom Irving. X-ray diffraction measurements of the extensibility of actin and myosin filaments in contracting muscle. *Biophysical Journal*, 67(6):2411–2421, 1994.

[130] Yale E Goldman and Andrew F Huxley. Actin compliance: are you pulling my chain? *Biophysical Journal*, 67(6):2131, 1994.

[131] Kenneth S Campbell. Compliance accelerates relaxation in muscle by allowing myosin heads to move relative to actin. *Biophysical Journal*, 110(3):661–668, 2016.

[132] Kenneth S Campbell. Filament compliance effects can explain tension overshoots during force development. *Biophysical journal*, 91(11):4102–4109, 2006.

[133] C David Williams, Michael Regnier, and Thomas L Daniel. Elastic energy storage and radial forces in the myofilament lattice depend on sarcomere length. *PLoS computational biology*, 8(11):e1002770, 2012.

[134] DCS White and John Thorson. The kinetics of muscle contraction. *Progress in Biophysics and Molecular Biology*, 27:173–255, 1973.

[135] Sam Walcott. A differential equation model for tropomyosin-induced myosin cooperativity describes myosin–myosin interactions at low calcium. *Cellular and Molecular Bioengineering*, 6(1):13–25, 2013.

[136] MA Bagni, G Cecchi, PJ Griffiths, Y Maeda, G Rapp, and CC Ashley. Lattice spacing changes accompanying isometric tension development in intact single muscle fibers. *Biophysical journal*, 67(5):1965–1975, 1994.

[137] Nobuyuki Okamura and Shin'ichi Ishiwata. Spontaneous oscillatory contraction of sarcomeres in skeletal myofibrils. *Journal of Muscle Research & Cell Motility*, 9(2): 111–119, 1988.

[138] Katsuhiko Sato, Masako Ohtaki, Yuta Shimamoto, and Shin'ichi Ishiwata. A theory on auto-oscillation and contraction in striated muscle. *Progress in biophysics and molecular biology*, 105(3):199–207, 2011.

[139] Felipe de Souza Leite, Fabio C Minozzo, David Altman, and Dilson E Rassier. Microfluidic perfusion shows intersarcomere dynamics within single skeletal muscle myofibrils. *Proceedings of the National Academy of Sciences*, 114(33):8794–8799, 2017.

[140] Axel J Fenwick, Shelby R Leighton, and Bertrand CW Tanner. Myosin mgadp release rate decreases as sarcomere length increases in skinned rat soleus muscle fibers. *Biophysical Journal*, 111(9):2011–2023, 2016. doi: 10.1016/j.bpj.2016.09.024.

[141] Sally G Page and HE Huxley. Filament lengths in striated muscle. *The Journal of Cell Biology*, 19(2):369–390, 1963.

[142] Michael Murrell, Patrick W Oakes, Martin Lenz, and Margaret L Gardel. Forcing cells into shape: the mechanics of actomyosin contractility. *Nature Reviews Molecular cell biology*, 16(8):486–498, 2015.

[143] Wylie W Ahmed and Timo Betz. Dynamic cross-links tune the solid–fluid behavior of living cells. *Proceedings of the National Academy of Sciences*, 112(21):6527–6528, 2015.

[144] Samantha Stam, Simon L Freedman, Shiladitya Banerjee, Kimberly L Weirich, Aaron R Dinner, and Margaret L Gardel. Filament rigidity and connectivity tune the deformation modes of active biopolymer networks. *Proceedings of the National Academy of Sciences*, 114(47):E10037–E10045, 2017.

[145] Yuval Mulla, FC MacKintosh, and Gijsje H Koenderink. Origin of slow stress relaxation in the cytoskeleton. *Physical review letters*, 122(21):218102, 2019.

[146] Chase P Broedersz, Xiaoming Mao, Tom C Lubensky, and Frederick C MacKintosh. Criticality and isostaticity in fibre networks. *Nature Physics*, 7(12):983–988, 2011.